

Robust Flutter Analysis for Aeroservoelastic Systems

A THESIS
SUBMITTED TO THE FACULTY OF THE GRADUATE SCHOOL
OF THE UNIVERSITY OF MINNESOTA
BY

Aditya Kotikalpudi

IN PARTIAL FULFILLMENT OF THE REQUIREMENTS
FOR THE DEGREE OF
DOCTOR OF PHILOSOPHY

Gary J. Balas, advisor
Peter J. Seiler, advisor

April 2017

© Aditya Kotikalpudi 2017
All Rights Reserved

Acknowledgments

I would like to begin by expressing my deep gratitude for Dr. Peter Seiler for being an excellent advisor and guide for close to three years. Dr. Seiler's guidance has been the primary driving force behind this work. His dedication towards mine and all of his other students' academic progress and future careers has been remarkable. He was the first professor I talked to when I joined in as a Ph.D. candidate and I'm immensely happy to have worked with him, for it has been an excellent learning experience. He has always attempted to push me further than I thought in terms of excellence in research, technical writing and presentation. I will always remember something he once said - writing is research.

Acknowledging my Ph.D. advisor certainly cannot be complete without expressing my immense gratitude for Dr. Gary Balas, who was my advisor for the first two years of my Ph.D career. He laid the foundations to my research, introduced me to the world of aeroservoelasticity and more importantly, served as an excellent idol to look up to. His enthusiasm for high quality research and tangible contribution to the research community was infectious. He was the primary force behind partnership of the aeroservoelasticity research group and Systems Technology Inc., a research firm based out of Hawthorne CA which offered me an internship and eventually a job. I would like to believe that a small part of him lives in every student he guided and mentored, and I consider myself very fortunate to have been one of them.

I would also like to acknowledge Dr. Harald Pfifer, a post-doctoral research associate with Dr. Balas and later with Dr. Seiler, whose role in my academic career at UMN has been as important as my two advisors, if not more. Harald has had a deep impact on the way I go about my research work, write my publications and present my work in seminars and talks. As my immediate 'boss', he always pushed me to improve, learn from my mistakes and strive for high quality research output, whether in terms of results or written work. I sincerely thank him for dedicating time and energy towards my research endeavors, often at the cost of his own, and helping me progress over the years.

My fellow researchers in room 309 - Claudia, Abhineet, Bela (post-doctoral researcher), Julian, Sally Ann, Paul, Raghu, David, Jen, Masanori, Bin and Shu have all been a part of my Ph.D. years and have enriched them. The fun times with the lab will always be a cherished part of my time in Minnesota. I would particularly like to ac-

knowledge those who were a part of the aeroservoelasticity group - Claudia, Abhineet, Bela, Julian and Sally Ann. Their contributions are a part of this thesis and more importantly, a part of my professional career ahead. I would also like to acknowledge the contribution and support from a few people outside the university, specifically Brian Danowsky and Dr. David Schmidt, for engaging with me in interesting and fruitful discussions over the years. They have certainly contributed to my understanding of aeroelastic modeling and mean axes formulation, and it is a great joy to continue working with them today and for foreseeable future.

An important event during my grad school life was meeting my wife, Sahiti on campus. She has been a pillar of support throughout my graduate student life. As my frustration-absorber, motivator and my best friend, she became and continues to be an indispensable part of my life. She, along with my room-mates Praveen and Abhineet, have been my family in Minnesota for the four years I lived there, and for that I cannot thank them enough. And of course, I would like to express my deepest gratitude and love for my family back in India - my dad, mom and sister. They have been patient with my lack of phone-calls, listened to me talk about my work for hours and given me nothing but support and encouragement in return. Thank you!

Finally, I want to acknowledge the support of the various institutions like NASA and Systems Technology Inc. which have provided financial and technical support for my research.

Dedication

To My Family

Abstract

The dynamics of a flexible air vehicle are typically described using an aeroservoelastic model which accounts for interaction between aerodynamics, structural dynamics, rigid body dynamics and control laws. These subsystems can be individually modeled using a theoretical approach and experimental data from various ground tests can be combined into them. For instance, a combination of linear finite element modeling and data from ground vibration tests may be used to obtain a validated structural model. Similarly, an aerodynamic model can be obtained using computational fluid dynamics or simple panel methods and partially updated using limited data from wind tunnel tests. In all cases, the models obtained for these subsystems have a degree of uncertainty owing to inherent assumptions in the theory and errors in experimental data. Suitable uncertain models that account for these uncertainties can be built to study the impact of these modeling errors on the ability to predict dynamic instabilities known as flutter. This thesis addresses the methods used for modeling rigid body dynamics, structural dynamics and unsteady aerodynamics of a blended wing design called the Body Freedom Flutter vehicle. It discusses the procedure used to incorporate data from a wide range of ground based experiments in the form of model uncertainties within these subsystems. Finally, it provides the mathematical tools for carrying out flutter analysis and sensitivity analysis which account for these model uncertainties. These analyses are carried out for both open loop and controller in the loop (closed loop) cases.

Contents

List of Tables	vi
List of Figures	vii
Chapter 1 Introduction	1
Chapter 2 Dynamics Modeling using Mean Axes Constraints	6
2.1 Equation of Motion in Mean Axes	8
2.1.1 Derivation of Equations of Motion	8
2.1.2 Discussion on Lagrangian Approach	19
2.2 Linearized Model for BFF Vehicle	21
2.2.1 Finite Element Modeling	22
2.2.2 BFF Structural Model	24
2.2.3 Linearized Equations of Motion	25
2.3 Summary	27
Chapter 3 Aerodynamic Forces for Flexible Aircraft	28
3.1 Model Overview	31
3.2 Doublet Lattice Method	32

3.2.1	Aerodynamic Influence Coefficients Matrix	34
3.2.2	Correction to Steady Solution	37
3.3	Continuous Aerodynamic Model in Modal Coordinates	38
3.3.1	Grid Interpolation	39
3.3.2	Generalized Aerodynamics Matrices	43
3.3.3	Rational Function Approximation	48
3.4	Unsteady Aerodynamics Model for the BFF Vehicle	52
3.4.1	Implementation and Validation	52
3.4.2	Aerodynamic Model for BFF Vehicle	54
3.5	Summary	58
Chapter 4 Uncertainty Modeling		60
4.1	Introduction	60
4.2	Uncertainty Descriptions	62
4.3	Uncertainties in Structural Dynamics	64
4.3.1	Ground Tests for Structural Model Identification	64
4.3.1.1	Static Deformation Tests	64
4.3.1.2	Ground Vibration Tests	65
4.3.2	Parametric Uncertainties	66
4.3.2.1	Approximation using Dynamic Uncertainty bounds	67
4.3.2.2	Eigenvector Derivatives Method	69
4.3.3	Mode Shape Uncertainties	72
4.3.4	Uncertain Structural Model	76
4.4	Uncertainties in Aerodynamics	77



4.4.1	Experiments for Aerodynamic Model	78
4.4.2	Parametric Uncertainties	78
4.4.2.1	Aerodynamic Stability Derivatives	78
4.4.2.2	Structural Parametric Uncertainties	79
4.4.3	Dynamic Uncertainties	80
4.5	Uncertain Model for BFF Vehicle	81
4.5.1	Parametric uncertainties in structural model	81
4.5.2	Uncertainties from GVT data	83
4.5.3	Parametric Uncertainties in Aerodynamic Model	89
4.5.4	Dynamic Uncertainty in Unsteady Aerodynamics	90
4.6	Summary	92
Chapter 5 Robust Flutter Analysis		94
5.1	State Space Model	97
5.2	Nominal Flutter Analysis	103
5.2.1	Classical Flutter Analysis Background	103
5.2.1.1	p Method	104
5.2.1.2	k Method	105
5.2.1.3	p-k method	107
5.2.2	BFF Vehicle Flutter Analysis	108
5.3	Robust Flutter Analysis	110
5.3.1	Structured Singular Value	111
5.3.2	Robust Flutter Analysis for BFF vehicle	113
5.4	Sensitivity Analysis	117


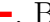







5.4.1	Approach for Sensitivity Analysis	118
5.4.2	Results & Discussion of Sensitivity Analysis	120
5.5	Summary	125
Chapter 6	Closed Loop Analysis	126
6.1	Aircraft Model for Synthesis	127
6.1.1	Model Order Reduction	129
6.1.2	Parasitic Dynamics	131
6.2	Baseline Control Design	132
6.2.1	Nominal Closed Loop Flutter Boundary	137
6.2.2	Robust Closed Loop Flutter Boundary	138
6.3	Closed Loop Sensitivity Analysis	140
6.4	Summary	144
Chapter 7	Conclusion	146
7.1	Conclusions	146
7.2	Future Directions	148
Bibliography		150
Appendix A	Appendices	161
A.1	Equations for Doublet Lattice Method	161
A.2	Derivation for Nelson's Method	163
A.3	BFF Vehicle State Space Matrices	166

List of Tables

4.1	Weights for structural parametric uncertainties and corresponding bounds	82
4.2	Weights for structural parametric uncertainties and corresponding bounds	89
4.3	Weights for aerodynamic parametric uncertainties and corresponding bounds	90
5.1	Slopes of the Sensitivity Plot for different Uncertainties	122
6.1	Slopes of the Sensitivity Plot for different Uncertainties in closed loop	142

List of Figures

1.1	BFF aircraft in background and a UAV testbed with same aerodynamic design in the foreground	3
2.1	Floating Reference Frame for Deformable Body	9
2.2	Finite Element Model for the BFF Vehicle	24
2.3	Beam Element used in Finite Element Model for BFF Vehicle	24
3.1	A typical discretization of the lifting surface S	33
3.2	The 2×2 grid example in top view, with a superimposed structural model	39
3.3	A representative infinite thin plate deformation	41
3.4	Spline grid construction	42
3.5	Kernel function distribution on a panel of AR= 5 at $k = 2$ and Mach 0.8	53
3.6	CAD model of BFF aircraft and the corresponding aerodynamic grid	55
3.7	Spline grid construction of the BFF aircraft	56
3.8	Unsteady aerodynamics transfer function fitting for the BFF aircraft, RFA model:  , Raw GAM data: 	57
3.9	Aerodynamics transfer functions for the BFF aircraft from 20 to 50 m/s	58
4.1	LFT feedback loop	63

4.2	Upper and Lower bound models obtained via C.G. perturbation. Nominal model indicated by  , Bounds indicated by 	68
4.3	Sensor locations for GVT tests	84
4.4	Thin plate spline for extracting mode shape data from GVT tests	84
4.5	Mode shape errors between GVT data () and FE model ()	85
4.6	Mode shape error comparison: GVT-FEM difference (), Theoretical perturbation due to parameters ()	86
4.7	Mode shape error comparison: GVT-FEM difference (), Perturbation due to parameters ()	88
4.8	Rational Function Fitting of Unsteady Aerodynamics	91
5.1	Location of accelerometers on BFF aircraft and control surfaces used for flutter suppression	99
5.2	Finite Element Model	100
5.3	Short period and first symmetric wing bending modes variation with airspeed	110
5.4	LFT feedback loop	111
5.5	LFT feedback loop	112
5.6	Aeroelastic model with Structured Uncertainty	115
5.7	$\bar{K} - V$ graph for the BFF vehicle	116
5.8	$\bar{K} - V$ graph variation in uncertainty for structural bending stiffness, baseline uncertainty given by ()	120
5.9	Sensitivity Plot showing variation of robust flutter boundary with change in bending stiffness uncertainty bound	121

5.10	Sensitivity plot for BFF uncertain model. The lines represent steady lift coeff: (—◆—), steady pitch coeff: (—▲—), unsteady aerodynamics: (—■—), Pitch moment of inertia: (—■—), Bending stiffness: (—■—), Torsional Stiffness (—◆—), C.G. location (—◆—) and mass distribution (—●—)	122
6.1	Reduced order model (— comparison with full order model (·····))	131
6.2	Generalized Plant interconnections	134
6.3	H_∞ Control Design	134
6.4	Control Input Weighting	135
6.5	Controller Frequency Response	136
6.6	Open (---) and closed loop (—) frequency response of the performance output	136
6.7	Open (---) and closed loop (—) frequency response for pitch rate output	137
6.8	Pole map showing flutter boundary in the BFF model in closed loop	138
6.9	Closed (—◆—) and open loop (—◆—) $\bar{K} - V$ plot for Flutter Boundary	139
6.10	$\bar{K} - V$ graph variation for scaling in structural bending stiffness, closed loop	141
6.11	Closed loop sensitivity plot. The lines represent steady lift coeff: (—◆—), steady pitch coeff: (—▲—), unsteady aerodynamics: (—■—), Pitch moment of inertia: (—■—), Bending stiffness: (—■—), Torsional Stiffness (—◆—), C.G. location (—◆—) and mass distribution (—●—)	141

Chapter 1

Introduction

Aeroservoelasticity is the study of interaction between structural dynamics, aerodynamic forces, rigid body dynamics and control laws of fixed as well as rotor wing aircraft. It is an increasingly prominent field of research due to use of flexible, light-weight materials for construction of modern flight vehicles leading to higher fuel efficiency. Aircraft designs with high aspect ratio wings also lead to increased structural flexibility. Flexibility of airframes often gives rise to dynamic coupling between various rigid body and structural modes, thereby altering the aerodynamic loads on the airframes. Aeroservoelastic modeling and analysis aims to expand the scope of conventional rigid body flight dynamics modeling to account for aeroelastic coupling and their effects on aerodynamic force loads, static and dynamic stability, handling qualities and closed loop control design. Therefore, research in this field requires a multi-disciplinary effort spanning conventionally separate disciplines of aerodynamics, structural vibrations and control theory.

A major area of focus in aeroservoelasticity is stability analysis over the desired operational envelope. In addition to conventional stability problems due to rigid body dynamics, instabilities arising from aeroelastic coupling form an important part of the stability analysis. Two common types of instabilities are *divergence*, which is a static aeroelastic instability, and *flutter*, which is a dynamic aeroelastic instability. Divergence typically results in large, static or quasi-static structural deformations of lifting surfaces under aerodynamic loading which increases with the deformation, thus causing instability. Divergence can usually be avoided via careful structural design of the aircraft, which ensures appropriate static stability in the coupling between

aerodynamic forces and structural deflections. Flutter is a more complex form of instability that involves dynamic coupling between structural modes or structural and rigid body modes, typically aided by unsteady aerodynamic forces.

Flutter has been an important subject of study and research for several decades [1–3] and is the main topic of research for this thesis as well. A reliable prediction of an aircraft’s susceptibility to flutter across its intended flight envelope is possible with the aid of accurate aeroservoelastic models. As noted above, the multi-disciplinary nature of these systems make it difficult to build accurate models that can be analyzed using the standard stability and performance analysis tools from systems theory. Furthermore, relatively simpler models are required for control design, requiring the need to make simplifying assumptions in the modeling procedure. Therefore, modeling errors and simplifying assumptions need to be taken into account in order to carry out reliable flutter analyses for a given aeroservoelastic model. This serves as the primary motivation for the research presented in this thesis.

The Unmanned Aerial Vehicles (UAV) research group at the University of Minnesota carries out extensive research in the field of aeroservoelastic systems. Theoretical research in flight systems modeling [4, 5], model reduction [6, 7] and control design [8, 9] is complimented by experimental work in ground vibration tests [10, 11], flight tests [12] and system identification [13, 14]. The group is also a part of a multi-institutional team of researchers from academia and industry, working on a grant from NASA titled *Performance Adaptive Aeroelastic Wing* (www.paaw.net). The objective of the project is to demonstrate active flutter suppression as well as active morphing wing control in flight. For carrying out experimental flight tests, the group has built a number of test bed UAVs with varying structural characteristics [15]. In keeping with the research philosophy of the group, all data related to flight and ground tests, modeling tools and control design tools are made open source on the group website mentioned above.

The test bed UAVs built for flight test purposes are based on the aerodynamic design of the Body Freedom Flutter (BFF) vehicle built by Lockheed Martin and the Air Force Research Laboratory [16]. A total 7 BFF vehicles were built for demonstrating an aeroelastic instability known as body freedom flutter in flight. Body freedom flutter (BFF mode) involves unstable dynamic coupling between the rigid body short period mode and the first structural wing-bending mode. The objective of the flight

tests for the BFF vehicle ranged from testing the flight envelope in open loop flight to demonstrating expansion of the envelope via active flutter suppression in closed loop flight.

One of the BFF vehicles was donated to the UAV research group in 2012 for conducting further research on body freedom flutter and its active suppression using suitable control laws. The BFF vehicle serves as the main application for all the modeling and analysis methods developed and discussed in this thesis. Although the donated BFF vehicle has never been flown by the group till date, the test bed UAVs which are based on its design have been successfully test flown [15]. The BFF vehicle itself

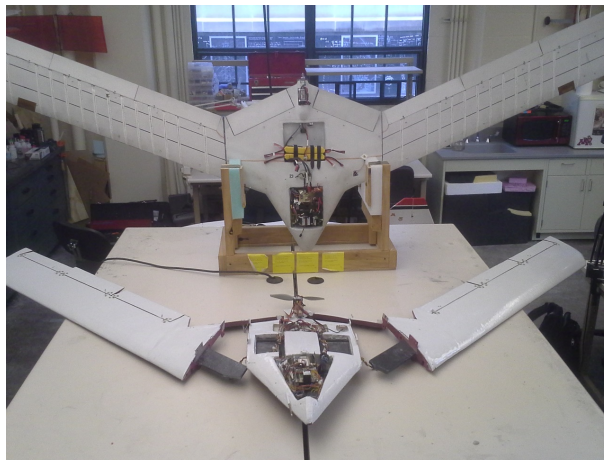


Figure 1.1: BFF aircraft in background and a UAV testbed with same aerodynamic design in the foreground

has been subjected to extensive ground testing such as inertia swing tests and ground vibration tests. A nonlinear aeroelastic model has been constructed using the data from these ground tests, as described in Chapters 2 and 3.

The BFF vehicle model is chosen for developing a robust flutter analysis framework since it is considered an ideal candidate for this purpose. The model is constructed using a subsystem based approach, where each subsystem is associated with a particular aspect such as aerodynamics or structural dynamics. These subsystems are modeled individually and are dependent on model parameters obtained from ground tests and subsequently updated using flight test data. Therefore, the model presents an opportunity to incorporate experimental errors in parameter values and errors due to theoretical modeling approximations in the form of parametric and systemic uncertainties.

Stability analysis and control design for any physical system requires mathematical models which accurately capture the dynamics associated with potential instabilities. Since modeling errors and approximations are inevitable, it is important for the stability analysis and control design procedures to take them into account. The nonlinear model for the BFF vehicle and the linear models obtained subsequently via linearization form the basis of flutter analysis described in this thesis. Broadly, the main problems which this work tries to address are robust flutter analysis in presence of modeling errors and affect of various model parameters as well as subsystems on flutter analysis.

Model uncertainty and stability analysis described in this thesis are based on the robust control theory framework. Specifically, the analysis is based on a measure of robustness called the structured singular value (μ) [17, 18]. The μ based framework has been used in recent years to carry out robust flutter analysis for aeroservoelastic systems [19, 20]. Lind and Brenner have also demonstrated the method for updating model uncertainties using flight data, both offline and in real time during flight [21]. Although not used in this work, it should be noted that a more general approach for representing modeling errors, called the Integral Quadratic Constraints (IQCs) [22–24], is also used as a framework for flutter analysis which accounts for various nonlinearities in the model in addition to the above mentioned uncertainties. However, a detailed description of various uncertainties and computation of relevant bounds for a complex system like the BFF vehicle has not been done extensively in literature.

The research described in this thesis addresses these topics in detail. Specifically, the main contributions of this thesis are

1. Develop an aeroelastic model for a UAV which includes six rigid body degrees of freedom and multiple structural modes, and is suitable for linearization, uncertainty modeling and control design.
2. Identify and bound uncertainties in the aeroelastic model accounting for errors from multiple sources.
3. Develop methods which combine uncertainties from different sources in a unified manner. For example, uncertainties in mode shapes are combined with parametric uncertainties for the computation of uncertain structural models in

modal coordinates.

4. Develop μ based mathematical tools for robust flutter analysis and sensitivity analysis of the computed flutter boundary with respect to the uncertainties specified.

Chapter 2 describes the mean axes based dynamics modeling approach for obtaining a nonlinear, six degrees of freedom model for flexible fixed wing aircraft. The chapter also describes the structural model developed for the BFF vehicle and its incorporation into the mean axes approach. Chapter 3 describes the aerodynamic modeling approach used to capture unsteady aerodynamic loads due to structural vibrations. The doublet lattice method, which is a widely used potential flow based panel method, is described along with the procedure for transforming the aerodynamic model into suitable coordinate frame to enable coupling with structural dynamics. Chapter 4 covers the uncertainty modeling process used for the BFF vehicle. It provides the methods discussed above for defining uncertainties associated with model parameters, structural mode shapes, frequency dependent aerodynamic terms and potential overall systemic uncertainties in a unified manner. Chapter 5 describes the robust flutter analysis based on μ computation for an uncertain model of the BFF vehicle. This chapter also includes a sensitivity analysis to determine the effect on each of the specified uncertainty bounds on the robustness analysis. Chapter 6 considers a closed loop system consisting of a flutter suppression controller which is designed for actively damping the unstable BFF mode. The effect of a controller in the loop on robust flutter computation as well as sensitivity analysis results is analyzed. Finally, Chapter 7 provides the concluding remarks and future directions for this work.

Chapter 2

Dynamics Modeling using Mean Axes Constraints

The dynamics of a conventional aircraft are often modeled with an inherent assumption that the aircraft is rigid. This assumption underlines the fact that in frequency domain, vibrational modes of such an aircraft lie at sufficiently high frequencies compare to rigid body modes. Hence, there is a very remote possibility for any coupling between these dynamics, especially within the aircraft's intended flight envelope. Therefore, vibrational modes are usually ignored in the dynamics model. The standard rigid body flight dynamics modeling is very widely applied and published [25–27].

On the other hand, aeroservoelasticity deals with aircraft which exhibit elasticity within their nominal flight envelope. In such cases, the frequency gap between rigid body and vibrational modes is small and may also possibly overlap. Therefore, the structural dynamics of the aircraft cannot be ignored as they play a significant role in flight dynamics. More importantly, the coupling between rigid body dynamics and structural dynamics has to be accounted for. Depending on the modeling approach and the assumptions/approximations involved, the equations obtained for the dynamics can be highly coupled nonlinear equations.

It is advantageous to describe the dynamics of a flexible body using a set of equations which decouple the rigid body modes from the vibrational modes. Complete decoupling is not possible of course, but by carefully selecting the coordinate system and making certain approximations, it can be ensured that the coupling is restricted

to external forcing terms only. The mean axes approach, first described by Milne in the mid-1960s [28], has been developed keeping these advantages in mind. The mean axes are essentially a floating reference frame in which the dynamics of the flexible aircraft may be defined. By floating frame, it is implied that although the axes move with respect to an inertial frame as the elastic body moves, they are not attached to any material point on the body itself. The translation and rotation of the axes are governed by a specific set of equations known as the mean axes constraints, which are carefully constructed to ensure inertial decoupling as described above. The final result is a set of equations of motion which are essentially an extension of the well known rigid body equations. The state vector in this extended set of equations is expanded to include structural deformation states whose dynamics remain inertially uncoupled from the rigid body states. Therefore, mean axes based equations of motion for flexible aircraft lend themselves very well to standard modeling software, linearization and model reduction procedures as well as standard parametrization of external forces.

The mean axes approach has been widely studied and applied in fields ranging from aeroelastic models in atmospheric flight [29, 30], to spacecraft dynamics [31]. The drawbacks and limitations of the approach have also been pointed out, particularly by Meirovitch and Tuzcu [32]. Response to the work of Meirovitch and Tuzcu has also been published by one of the leading researchers in the field of mean axes based modeling, David Schmidt, see [33]. Equations of motion for the BFF vehicle have been developed using the mean axes approach primarily based on the derivation given by Waszak and Schmidt in Ref. [29]. The derivation, implications of the assumptions made in it and its scope of application to the BFF vehicle are discussed in this chapter. Additional research carried out at University of Minnesota as well as by others [30, 37, 38], which seek to resolve the unclear aspects of the derivation are also discussed. These discussions seek to provide confidence in the aeroelastic model constructed for the BFF vehicle.

The complete derivation for equations of motion using the mean axis approach is provided in Section 2.1. Discussion on the derivation and additional technical discussion and clarifications are also provided in this section. Section II discusses the application of mean axes based modeling approach to the BFF vehicle. Structural modeling of the aircraft as well as linearization of the overall model are also described in Section 2.2

2.1 Equation of Motion in Mean Axes

The mean axes approach for equations of motion of an elastic body is typically based on the Lagrangian method. A Newtonian momentum based approach can also be used as seen in [37,38]. The approach described here is based on the standard Lagrangian method and it takes advantage of availability of orthogonal structural modes which describe free vibrations of the flexible airframe. The derivation provided here is taken from the paper by Schmidt and Waszak [29]. The derivation is followed by a discussion on various insights into the underlying physics of the mean axes and its relation to the more well understood body-fixed axes used in the conventional equations of motion.

2.1.1 Derivation of Equations of Motion

The Lagrangian approach to deriving equations of motion is a prominent part of analytical mechanics [34,35]. It involves derivation of expressions for kinetic and potential energy, denoted T and U respectively, of the system under consideration. The expressions are in terms of the so called generalized coordinates q_i and their derivatives. The generalized coordinates are typically system parameters which completely describe all of its degrees of freedom. Equations of motion can be obtained in terms of the generalized coordinates using the Lagrange's equation shown below.

$$\frac{d}{dt} \left[\frac{\partial T}{\partial \dot{q}_i} \right] - \frac{\partial T}{\partial q_i} + \frac{\partial U}{\partial q_i} = Q_i \quad (2.1)$$

In Eq. (2.1), Q_i represent the generalized external forces acting on the system and are a function of the generalized coordinates. For further details, the reader is directed to standard texts on analytical mechanics [34,35].

The overall objective is to derive equations of motion for a fixed wing air vehicle with a flexible airframe. To obtain inertially decoupled equations, the generalized coordinates are chosen with respect to the mean axes reference frame. The first step is to consider an extended elastic body with continuous mass distribution as shown ahead.

There are two frames of reference shown in Fig. 2.1 - the inertial frame with origin I and a floating frame with origin F . The orientation of the floating frame is unspecified at this point. An infinitesimal mass element is assumed to be located at point i as shown. The equations of motion are derived in terms of vectors expressed in the

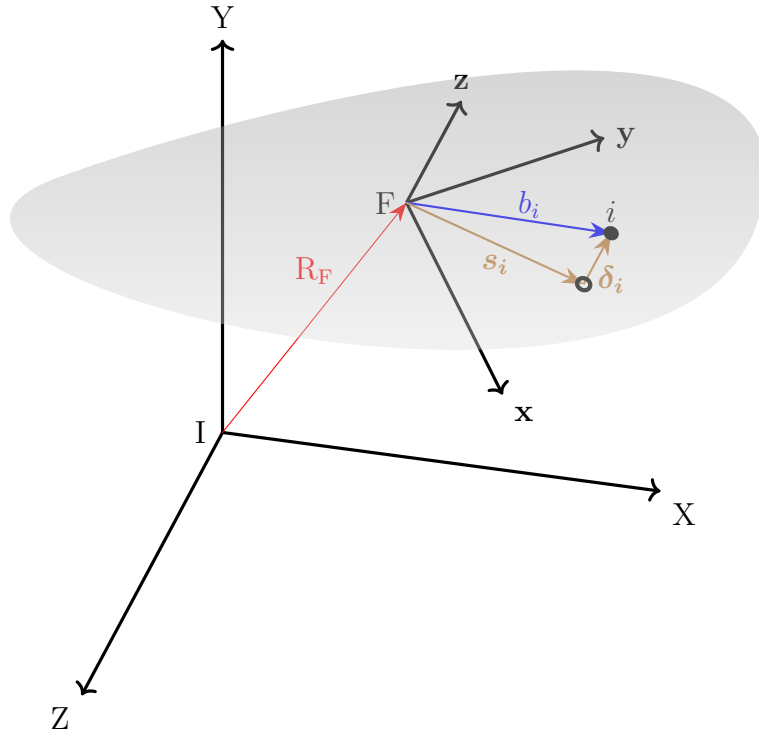


Figure 2.1: Floating Reference Frame for Deformable Body

floating reference frame while applying suitable constraints (referred to as the mean axes constraints) on its location and orientation.

Since we are interested in developing the equations in the floating reference frame, generalized coordinates and their derivatives are chosen with respect to those axes. The overall approach is to derive the expressions of kinetic and potential energy for the infinitesimal mass element at point i shown in Fig. 2.1 in terms of these generalized positions and velocities and then integrate over the volume of the entire body.

Since multiple reference frames are involved, the vectors associated with position and velocity of the mass element may be expressed in different ways. For instance, the position could be described relative to the inertial frame (denoted as inertial position) or relative to the floating frame F (denoted as relative position). Furthermore, the inertial and relative positions may be represented using orthogonal unit vectors along the axes of either of the two frames. The notation used in this chapter helps distinguish between them as shown.

1. A vector may be expressed using unit vectors of the inertial frame as

$$R_F = X_F \hat{I} + Y_F \hat{J} + Z_F \hat{K} \quad (2.2)$$

where X_F , Y_F and Z_F are components of the position vector R_F along the inertial axes and \hat{I} , \hat{J} and \hat{K} are the unit vectors along the inertial axes.

2. A vector can be expressed in the floating frame using unit vectors along those axes as

$$R_F = x_F \hat{i} + y_F \hat{j} + z_F \hat{k} \quad (2.3)$$

where x_F , y_F and z_F are components of the position vector R_F along the floating axes. The only difference between the vectors in Eqs. (2.2) and (2.3) is the axes in which they are expressed.

3. Time derivative of a vector p with respect to the inertial frame is denoted with an overhead dot as

$$\left. \frac{dp}{dt} \right|_I = \dot{p} \quad (2.4)$$

4. Time derivative of a vector p with respect to the floating reference frame is denoted as

$$\left. \frac{dp}{dt} \right|_F = \overset{\circ}{p} \quad (2.5)$$

Keeping the notation above in mind we now look at the transport theorem [34, 35], which provides the expression for the time derivative of a vector expressed in a rotating reference frame with respect to the inertial reference frame.

Theorem 2.1.1. *Let p be a vector. Let F be a non-inertial reference frame rotate with an angular velocity ω . Then the time rate of change of p with respect to the inertial and non-inertial frames are related by*

$$\dot{p} = \overset{\circ}{p} + \omega \times p \quad (2.6)$$

The transport theorem is necessary for computing inertial velocities and accelerations expressed in the floating frame for any point in the extended body. Keeping the notation as well as the Transport theorem in mind, we now derive the required equations of motion.

The position of the infinitesimal mass element at i can be depicted as a sum of its relative position with respect to the floating reference frame and position of the frame with respect to the inertial frame as

$$r_i = R_F + b_i \quad (2.7)$$

where r_i is the position vector for point i . Therefore, from 2.1.1, the inertial velocity of the mass element in the floating frame is computed as

$$\left. \frac{dr_i}{dt} \right|_I = \dot{R}_F + \dot{b}_i \quad (2.8a)$$

$$\dot{R}_F = \dot{\hat{R}}_F + \omega \times R_F \quad (2.8b)$$

$$\dot{b}_i = \dot{\hat{b}}_i + \omega \times b_i \quad (2.8c)$$

where ω is assumed to be the angular velocity of the floating reference frame. Eq. (2.8) can now be used to compute the kinetic energy for the mass element. To keep the overall expressions simple, the inertial velocity term for the origin of the floating frame, given by Eq. (2.8b), is continued to be denoted as \dot{R}_F . Eq. (2.8b) will be used at a later stage to replace that term with the complete notation. Writing the expression for kinetic energy of the mass element and integrating over the volume of the body, we have the total kinetic energy as

$$T = \frac{1}{2} \int_V \left(\dot{R}_F + \dot{b}_i \right) \cdot \left(\dot{R}_F + \dot{b}_i \right) \rho dV \quad (2.9)$$

Using Eqs. (2.8) to expand,

$$T = \frac{1}{2} \int_V \dot{R}_F \cdot \dot{R}_F + \dot{b}_i \cdot \dot{b}_i + (\omega \times b_i) \cdot (\omega \times b_i) + 2 \left\{ \dot{R}_F \cdot \dot{b}_i + \dot{b}_i \cdot (\omega \times b_i) + \dot{R}_F \cdot (\omega \times b_i) \right\} \rho dV \quad (2.10)$$

where ρ is density of the the body, assumed to be constant across its volume.

As mentioned earlier, orientation of the floating frame has not yet been defined. The primary motivation behind defining a floating frame rather than a body fixed frame is to enable inertial decoupling between rigid body and structural modes of the body which is under unconstrained motion. By applying suitable constraints, the orientation of the frame which results in such a decoupling can be established. These

constraints are referred to as the mean axes constraints, and the axes are referred to as mean axes.

According to Waszak and Schmidt, the orientation of the mean axes are defined so that the relative linear and angular momenta due to elastic deformation are zero at each instant [29]. In mathematical terms, these constraints can be expressed as

$$\int_V \dot{b}_i \rho dV = 0 \quad (2.11a)$$

$$\int_V b_i \times \dot{b}_i \rho dV = 0 \quad (2.11b)$$

Applying these constraints to the expression of kinetic energy shown in Eq. (2.10) results in its simplification. Specifically, the fourth and fifth terms of Eq. (2.10) can be rewritten as

$$\int_V \dot{b}_i \cdot (\omega \times b_i) \rho dV = \int_V (b_i \times \dot{b}_i) \cdot \omega \rho dV = 0 \quad (2.12a)$$

$$\int_V \dot{R}_F \cdot \dot{b}_i \rho dV = \dot{R}_F \cdot \int_V \dot{b}_i \rho dV = 0 \quad (2.12b)$$

where Eq. (2.12a) involves the scalar triple product identity. The simplified expression for kinetic energy may now be written as

$$T = \frac{1}{2} \int_V \left[\dot{R}_F \cdot \dot{R}_F + \dot{b}_i \cdot \dot{b}_i + (\omega \times b_i) \cdot (\omega \times b_i) + 2\dot{R}_F \cdot (\omega \times b_i) \right] \rho dV \quad (2.13)$$

To further simplify the expression in Eq. (2.12), another constraint is applied - location of the origin of the floating reference frame F is fixed at the instantaneous center of mass of the body. This can be expressed mathematically as

$$\int_V b_i \rho dV = 0 \quad (2.14)$$

The last term in Eq. (2.13) can now be rewritten using Eq. (2.14) as

$$\int_V \dot{R}_F \cdot (\omega \times b_i) \rho dV = \omega \times \left[\dot{R}_F \cdot \int_V b_i \rho dV \right] = 0 \quad (2.15)$$

The final expression for kinetic energy can now be written as

$$T = \frac{1}{2} \int_V \left[\dot{R}_F \cdot \dot{R}_F + \dot{b}_i \cdot \dot{b}_i + (\omega \times b_i) \cdot (\omega \times b_i) \right] \rho dV \quad (2.16)$$

The first two terms in Eq. (2.16) can be expressed in terms of total mass and instantaneous moments of inertia of the body. Therefore we have

$$T = \frac{1}{2} M \dot{R}_F \cdot \dot{R}_F + \frac{1}{2} \omega^T I \omega + \frac{1}{2} \int_V \dot{b}_i \cdot \dot{b}_i \rho dV \quad (2.17)$$

where M is the total mass of the body and I is the instantaneous inertia tensor which accounts for elastic deformations. Careful study Eq. (2.17) shows that the first two terms essentially represent rigid body translational and rotational kinetic energy associated with the axes. The third term represents kinetic energy of the body with respect to the axes, which as shown later, represents the vibrational energy of the body. By assuming the floating reference frame to be the mean axes frame, energy terms associated with coupled degrees of freedom have been reduced to zero as seen in Eqs. (2.12) and (2.14). As seen later, this directly results in inertially decoupled equations of motion.

The Lagrangian also requires potential energy of the system, which in this case involves the gravitational potential energy and strain energy due to structural deformations. We express the gravitational potential energy for the structurally deformed body as

$$U_g = - \int_V (R_F + b_i) \cdot g \rho dV \quad (2.18)$$

The inertial axes defined for the body are taken to be the datum for obtaining the expression above. Taking the gravity vector g out of the integral in Eq. (2.18) and using Eq. (2.14) to simplify, we get the expression for gravitational potential energy as

$$U_g = - \int_V R_F \cdot g \rho dV = -R_F \cdot gM \quad (2.19)$$

For strain energy, motion of point i due to deformations is alone taken into consideration. In Fig. 2.1, vector b_i can be seen as the sum of two vectors s_i and δ_i . s_i is essentially location of the mass element in its undeformed shape (also referred to as jig shape) whereas δ_i represents the displacement of the element due to structural deformation i.e. strain. Using D'Alembert's principle [36], the strain energy can be

written as

$$U_s = -\frac{1}{2} \int_V \overset{\circ\circ}{\delta}_i \cdot \delta_i \rho dV \quad (2.20)$$

where the accent on $\overset{\circ\circ}{\delta}_i$ represents a double time derivative with respect to the floating frame.

Eqs. (2.11) and Eq. (2.14) constrain the orientation and position of the floating axes. However, the simplified, decoupled expression for kinetic energy in Eq. (2.17) simply assumes that a set of axes which satisfy the mean axes constraints exists. Therefore, to better describe the assumed set of axes for a given elastic body, the concept of free vibration modes is introduced by Waszak and Schmidt [29]. The mean axes constraints are rewritten in terms of free vibration modes, which provide a more practical interpretation of the constraints as well as a means to determine the orientation of the axes with respect to the body. But before moving further, the mean axes constraints shown in Eq. (2.11) are further simplified via some additional assumptions to make them more feasible from an engineering problem perspective.

As mentioned earlier, the vector b_i in Fig. 2.1 can be expressed as a sum of two vectors s_i (location of point i in jig shape) and δ_i (strain displacement of point i). Therefore, Eq. (2.11) can be rewritten as

$$\int_V \left(\overset{\circ}{s}_i + \overset{\circ}{\delta}_i \right) \rho dV = 0 \quad (2.21a)$$

$$\int_V (s_i + \delta_i) \times \left(\overset{\circ}{s}_i + \overset{\circ}{\delta}_i \right) \rho dV = 0 \quad (2.21b)$$

To simplify the Eqs. (2.21) further, Waszak and Schmidt note that the vector s_i which represents the undeformed location of the infinitesimal mass element is invariant with respect to the floating frame. Furthermore, by assuming small deformations, the product of δ_i and $\overset{\circ}{\delta}_i$ is assumed very small and is neglected without any effect up to first order of accuracy. Therefore, Eqs. (2.21) can be written in a simplified form as

$$\int_V \overset{\circ}{\delta}_i \rho dV = 0 \quad (2.22a)$$

$$\int_V s_i \times \overset{\circ}{\delta}_i \rho dV = 0 \quad (2.22b)$$

Eq. (2.22) represent the so called *practical mean axes*, for which orientation and location can be determined analytically since they are explicitly written in terms of

elastic deformations. Also, it should be noted that the approximations made above can be easily carried over to the expressions for kinetic energy and strain potential energy in Eqs. (2.17) and (2.20). The advantage of the explicit and linear dependence of mean axes constraints on the elastic deformations will be made clear as follows.

Structural deformations in an unconstrained elastic body can be described using a linear combination of its free vibration modes. These modes, also referred to as mode shapes, are time invariant spatial functions which essentially describe the *direction* of deformation. Using mode shapes, elastic deformation δ_i of point i in Fig. 2.1 can be written as

$$\delta_i(x_i, y_i, z_i, t) = \sum_{j=1}^{\infty} \Phi_j(x_i, y_i, z_i) \eta_j(t) \quad (2.23)$$

where $\eta(t)$ are the generalized modal displacement coordinates. Eq. (2.23) can be seen as an exercise in variable separation for structural deformations into spatial and temporal components. It should be noted that free vibration modes, by definition, are orthogonal to one another. Ideally, infinite mode shapes are required to completely describe the deformations for a continuous elastic body. For practical purposes only a finite number of them, corresponding to the top few vibrational frequencies, are retained for developing the equations of motion. The yet unspecified number of free vibration modes which are retained can be denoted as n_s . The simplified mean axes constraints in Eqs. (2.22) can be written in terms of mode shapes as

$$\sum_{j=1}^{n_s} \dot{\eta}_j(t) \int_V \Phi_j(x_i, y_i, z_i) \rho dV = 0 \quad (2.24a)$$

$$\sum_{j=1}^{n_s} \dot{\eta}_j(t) \int_V s_i \times \Phi_j(x_i, y_i, z_i) \rho dV = 0 \quad (2.24b)$$

Waszak and Schmidt interpret Eqs. (2.24) as constraints on free vibration modes to be orthogonal to rigid body translational (Eq. (2.24a)) and rotational (Eq. (2.24b)) modes respectively. Eq. (2.23) is applied to the last term of the kinetic energy expression in Eq. (2.17) keeping in mind invariance of s_i in the floating reference frame. The last term, involving \dot{b}_i can be rewritten as

$$\int_V \dot{\delta}_i \cdot \dot{\delta}_i \rho dV = \int_V \left[\left(\sum_{j=1}^{n_s} \Phi_j \dot{\eta}_j \right) \cdot \left(\sum_{k=1}^{n_s} \Phi_k \dot{\eta}_k \right) \right] \rho dV \quad (2.25)$$

To further simplify Eq. (2.25), the orthogonality of mode shapes is used, which can be expressed as -

$$\int_V \Phi_j \cdot \Phi_k \rho dV = 0 \quad \forall j \neq k \quad (2.26)$$

We define \mathcal{M}_j as the j^{th} generalized mass which can be expressed as

$$\mathcal{M}_j = \int_V \Phi_j \cdot \Phi_j \rho dV \quad (2.27)$$

Using Eqs. (2.26) and (2.27), the last term of kinetic energy expression shown in Eq. (2.25) can be written as

$$\int_V \dot{\delta}_i \cdot \dot{\delta}_i \rho dV = \frac{1}{2} \sum_{j=1}^{n_s} \mathcal{M}_j \dot{\eta}_j^2 \quad (2.28)$$

Finally, Eq. (2.17) can be written in terms of free vibrational modes as

$$T = \frac{1}{2} M \dot{R}_F \cdot \dot{R}_F + \frac{1}{2} \omega^T I \omega + \frac{1}{2} \sum_{j=1}^{n_s} \mathcal{M}_j \dot{\eta}_j^2 \quad (2.29)$$

Also, the expression for strain potential energy in Eq. (2.20) is also rewritten in terms of free vibration modes as

$$U_s = \frac{1}{2} \sum_{j=1}^{n_s} \tilde{\omega}_j^2 \eta_j^2 \mathcal{M}_j \quad (2.30)$$

where $\tilde{\omega}$ is the set of free vibration frequencies for the body. Eqs. (2.19), (2.29) and (2.30) can now be used to derive the required equations of motion using Lagrange's equations shown in Eq. (2.1).

The terms \dot{R}_F and ω are explicitly written in terms of their components along the floating axes as

$$\dot{R}_F = u\hat{i} + v\hat{j} + w\hat{k} \quad (2.31a)$$

$$\omega = p\hat{i} + q\hat{j} + r\hat{k} \quad (2.31b)$$

where u , v and w are the components of the inertial velocity of origin F while p , q and r are components of angular velocity ω , along the floating reference frame. It should be noted that using the expression for R_F in Eq (2.3) and the formula for its

derivative from 2.1.1 as shown in Eq. (2.8b), u , v and w can be written as

$$u = \dot{x}_F + qz_F - ry_F \quad (2.32a)$$

$$v = \dot{y}_F + rx_F - pz_F \quad (2.32b)$$

$$w = \dot{z}_F + py_F - qx_F \quad (2.32c)$$

Also, the components of ω may be written in terms of the Euler angles ϕ , θ and ψ and their derivatives as [25]

$$\begin{bmatrix} p \\ q \\ r \end{bmatrix} = \begin{bmatrix} 1 & 0 & -\sin(\theta) \\ 0 & \cos(\phi) & \cos(\theta)\sin(\phi) \\ 0 & -\sin(\phi) & \cos(\theta)\cos(\phi) \end{bmatrix} \begin{bmatrix} \dot{\phi} \\ \dot{\theta} \\ \dot{\psi} \end{bmatrix} \quad (2.33)$$

Using Eqs. (2.31), the kinetic energy expression can be written as

$$T = \frac{1}{2}M(u^2 + v^2 + w^2) + \frac{1}{2} \begin{bmatrix} p \\ q \\ r \end{bmatrix} I \begin{bmatrix} p & q & r \end{bmatrix} + \frac{1}{2} \sum_{j=1}^{n_s} \mathcal{M}_j \dot{\eta}_j^2 \quad (2.34)$$

Similarly, the gravitational and strain potential energy may be written as

$$U_g = -Mg(-x_F \sin(\theta) + y_F \sin(\phi) \cos(\theta) + z_F \cos(\phi) \cos(\theta)) \quad (2.35a)$$

$$U_s = \frac{1}{2} \sum_{j=1}^{n_s} \tilde{\omega}_j^2 \eta_j^2 \mathcal{M}_j \quad (2.35b)$$

Eqs. (2.32) and (2.33) can be substituted into the expression for kinetic energy in Eq. (2.34) to obtain it in terms of the generalized coordinates x_F , y_F , z_F , ϕ , θ , ψ and modal coordinates η_j . Eq. (2.1) can now be used to derive the equations of motion associated with each of these coordinates. However, it is generally more useful to write the equations in terms of translational and angular velocities in the body axes (in this case, mean axes) i.e. u , v , w , p , q and r . Eqs. (2.32) and (2.33) can be used to make suitable substitutions in order to obtain the equations in terms of desired variables.

The complete, final equations of motion as obtained by Waszak and Schmidt are

$$M[\dot{u} - rv + qw + g\sin(\theta)] = Q_x \quad (2.36a)$$

$$M[\dot{v} - pw + ru - g\sin(\phi)\cos(\theta)] = Q_y \quad (2.36b)$$

$$M[\dot{w} - qu + pv - g\cos(\phi)\cos(\theta)] = Q_z \quad (2.36c)$$

$$I_{xx}\dot{p} - (I_{xy}\dot{q} + I_{xz}\dot{r}) + (I_{zz} - I_{yy})qr + (I_{xy}r - I_{xz}q)p + (r^2 - q^2)I_yz = Q_\phi \quad (2.36d)$$

$$I_{yy}\dot{q} - (I_{xy}\dot{p} + I_{yz}\dot{r}) + (I_{xx} - I_{zz})pr + (I_{yz}p - I_{xy}r)q + (p^2 - r^2)I_xz = Q_\theta \quad (2.36e)$$

$$I_{zz}\dot{r} - (I_{xz}\dot{p} + I_{yz}\dot{q}) + (I_{yy} - I_{xx})pq + (I_{xz}q - I_{yz}p)r + (q^2 - p^2)I_xy = Q_\psi \quad (2.36f)$$

$$\ddot{\eta}_j + \tilde{\omega}^2\eta_j = \frac{Q_{\eta_i}}{\mathcal{M}_i} \quad (2.36g)$$

In Eqs. (2.36), the terms on the right hand side i.e. Q_x , Q_y , Q_z , Q_ϕ , Q_θ , Q_ψ and Q_{η_i} are the generalized forces associated with each of the generalized coordinates. They can be computed in terms of the generalized coordinates using the virtual work principle, as described in [29]. In summary, the generalized forces Q_x , Q_y , and Q_z can be expressed in terms of lift, drag and side force by computing the angle of attack and sideslip angle between the mean axes and the wind axes. Similarly, Q_ϕ , Q_θ and Q_ψ are shown to be computed from the integrated roll, pitch and yawing moments obtained in the wind axes for a given air vehicle. However, unlike a rigid air vehicle, these forces and moments are also a function of the structural modes represented by the generalized coordinates η and their derivatives. On the other hand, the generalized structural excitation forces Q_{η_i} essentially represent the aerodynamic force and moment distribution across the airframe in modal coordinates. Therefore, Q_{η_i} is a function of rigid body states as well as structural states. Thus, in the mean axes based equations of motion, coupling between rigid body and structural dynamics takes place primarily via aerodynamic forces.

Although equations of motion shown in Eqs. (2.36) appear to be analogous to the standard equations in body-fixed frame for rigid aircraft (see [25]), it should be remembered that these equations are written in the mean axes frame which is not attached to any material point in the aircraft. In the next subsection, we discuss the assumptions made in this derivation and their implications as well as some of the unclear and ambiguous parts of the derivation. These points of discussion serve as the motivation for further study on the mean axes as undertaken by researchers at the University of Minnesota.

2.1.2 Discussion on Lagrangian Approach

The mean axes approach of deriving equations of motion for an elastic body results in a set of inertially decoupled equations as seen in Eqs. (2.36). Mathematically, these equations appear as an extension to the more commonly known equations for a rigid body in the body-fixed reference frame. Specifically, the mean axes frame enables the smooth addition of structural dynamics in the form of modal coordinates and its associated dynamics (Eq. (2.36 g)) without any additional coupling terms in the equations associated with rigid body translational and rotational modes (Eqs. (2.36 a-f)). The only changes in the rigid body equations comes in the form of added forcing terms on the right hand side, since the forces and moments are now a function of structural states as well.

Although the derivation itself makes it explicitly clear that the mean axes orientation is not decided a priori, the end results appear to take a very convenient form, as described above. This is considered very advantageous since in practice, the equations for an elastic air vehicle appear to be obtainable by extending the nonlinear rigid body dynamics model to account for elastic deformations and vibrations via linear modal dynamics equations. Therefore, if a structural model for the air vehicle is available for computing the mode shapes, mean axes based equations may be readily obtained. However, the assumption that the set of equations obtained in that manner automatically satisfy the mean axes constraints is a non-trivial one. For example, the structural dynamics for an elastic body is often described using a finite element model where the continuous mass with complex geometry is modeled as an assembly of simpler elastic elements. This model may then be used to obtain mode shapes, which in this derivation are assumed to be available a priori. Therefore, there is no explicit description of the role of any finite element model in the derivation, nor any specific indications on any inherent contradictions between the assumptions made for the structural model and the assumptions within the derivation above. Finally, there are several assumptions and other subtle technical aspects of the mean axes derivation shown in the previous subsection. These assumptions and technical subtleties need to be considered carefully in order to implement the mean axes approach in a practical example, specifically the BFF vehicle.

In order to address these technical issues and provide more clarity on the consequences of different assumptions, alternate approaches for mean axes derivations with and

without simplifying assumptions have been studied and developed [30,37,38]. In [30], Neto et al derive the equations of motion for an elastic aircraft using the Lagrangian approach for a general body reference frame using more precise definitions of rigid body modes and structural modes. Three different types of constraints leading to three different types of body reference frames are then considered - a body-fixed frame, the practical mean axes frame and a dual-constrained frame where the rigid body dynamics and structural dynamics are described in two separate yet fixed frames. Effects of retaining nonlinearities due to variable inertia tensor as well as inertial coupling on the overall dynamic response is studied for all three axes. An encouraging result from that work is that for small structural deformations, the practical mean axes approach is satisfactorily accurate in describing the dynamics of an elastic body without retaining any inertial coupling terms or a variable inertia tensor.

A common alternate method for derivation of equations of motion in the mean axes is the momentum based Newtonian approach. For instance, in [37], Nikravesh develops the equations of motion for an elastic body by expressing the mean axes constraints in terms of energy associated with elastic degrees of freedom while the equations themselves are derived from Newton's second law. A finite element model is assumed to be available for the body; however its incorporation into the equations of motion remain ambiguous. The main reason for lack of clarity is the construction of finite element matrices based on structural dynamics equations in an inertial frame and its subsequent use in a non-inertial frame without any modifications. The nature of structural vibrations described by the finite element model in a non-moving (inertial) vs. a moving frame is not adequately studied. However, the work in [37] does provide an intuitive grasp of the motion of the mean axes frame defined for a free-free elastic body.

Keyes and Seiler at University of Minnesota, in collaboration with Schmidt, have worked on developing an alternate derivation of the mean axes based equations of motion based on the Newtonian approach, see [38]. They attempt to provide deeper insights into the role played by initial conditions of the floating reference frame assumed on the mean axes constraints and their physical interpretation. Also, they provide clarity on the relationship between the mean axes constraints, nonlinear rigid body motion of the frame and the linear rigid body modes associated with a given free-free finite element model. A simple example of three masses connected via a linear torsional spring is also presented to provide further insight from a practical

application standpoint. The example also shows that the equations of motion based on mean axes approach describe the nonlinear dynamics with suitable accuracy for small structural deflections where linearity assumptions hold.

The various studies carried out as described above provide the confidence required for application of the mean axes based equations of motion for the BFF vehicle undergoing small deformations. The next section describes the aeroelastic model developed for the BFF vehicle in the mean axes reference frame. The structural dynamics of the BFF vehicle is described using a linear finite element model, which also provides the mode shapes for the vehicle, as described in the next section.

2.2 Linearized Model for BFF Vehicle

Equations of motion which describe the dynamics of the BFF vehicle are derived using the mean axes approach described in the previous sections. These equations are used to construct a suitable linear model for the aircraft which adequately captures the dynamics associated with body freedom flutter and thus serves as the basis for flutter analysis and control design. As mentioned in the previous chapter, body freedom flutter is essentially a result of unstable coupling between the rigid body short period mode and the first structural vibrational mode - symmetric first wing bending mode - at a particular airspeed. Therefore, the mean axes approach provides a simple way to model nonlinear rigid body dynamics and linear structural dynamics in a consistent and uncoupled manner.

A finite element model is constructed to model the structural dynamics of the aircraft and modal data required for the equations of motion are computed. In the interest of developing a low order model, and also keeping in mind that only the first wing bending mode is of interest for body freedom flutter, modal truncation is carried out where only the first six free vibration modes are retained. Mode shapes for the aircraft are derived via eigenvalue decomposition of the mass and stiffness matrices obtained for the finite element model. The mode shapes may then be used to obtain the generalized modal mass and stiffness matrices. These matrices can be suitably scaled to obtain the equations of motion associated with structural dynamics as shown in Eqs. (2.36). The finite element modeling technique is briefly discussed in the following subsection, followed by the model description for the BFF vehicle.

2.2.1 Finite Element Modeling

The finite element (FE) method is a widely used modeling tool for analysis of complex structural designs in a computationally efficient manner [39, 40]. Conceptually, the method models a given complex body as an assembly of smaller and much simpler parts which are called finite elements. The finite elements typically used are beams, plates and shells of varying structural and geometric properties. They are connected to one another at massless joints called nodes. Analytical solutions are usually available for the deformable mechanics of these elements, enabling the deformation to be expressed in terms of the nodes to which they are connected. Consequently, the overall deformation in the body may be expressed in terms of the motion of the underlying nodes. All the equations representing the motion of nodes are then assembled into a large system of equations by keeping the inter-connectivity of the elements in mind. The system of equations is then used to model the structural dynamics of the overall complex body.

Equations obtained from finite element methods may be linear or nonlinear depending on the assumptions made regarding the structural properties of the constituent elements. These assumptions in turn depend on the nature of vibrations considered for analysis for the overall structure. If a small deformation assumption is made for the structure, linear elements can be conveniently used for constructing a linear system of equations. Since the work in this thesis deals only with small deformations of the aircraft structure, only linear finite element modeling will be discussed here and used later in the development of the overall nonlinear equations of motion.

For any given assembly of linear elements, the overall system of equations may be written in a general form as

$$\underbrace{\begin{bmatrix} m_{11} & \cdots & m_{1n} \\ \vdots & \ddots & \vdots \\ m_{n1} & \cdots & m_{nn} \end{bmatrix}}_M \begin{bmatrix} \ddot{\delta}_1 \\ \vdots \\ \ddot{\delta}_n \end{bmatrix} + \underbrace{\begin{bmatrix} k_{11} & \cdots & k_{1n} \\ \vdots & \ddots & \vdots \\ k_{n1} & \cdots & k_{nn} \end{bmatrix}}_K \begin{bmatrix} \delta_1 \\ \vdots \\ \delta_n \end{bmatrix} = \underbrace{\begin{bmatrix} F_1 \\ \vdots \\ F_n \end{bmatrix}}_{F_{ext}} \quad (2.37)$$

where n is the total number of degrees of freedom of all the nodes, M and K are the so called mass and stiffness matrices and F is the column vector containing external forces at all nodes. The column vector containing δ_i represents the displacement of nodes along their degrees of freedom. It should be noted that the number of nodes

itself may be less than, equal to or greater than n depending on the nature of boundary conditions as well as the number of degrees of freedom associated with each of the finite elements. For the linear system of equations represented by Eq. (2.37), eigenvalue analysis can be carried out to compute the eigenvalues and their corresponding eigenvectors as shown.

$$[K - \lambda_i M]\phi_i = 0 \quad (2.38)$$

where λ_i is the i^{th} eigenvalue and ϕ_i is the corresponding i^{th} eigenvector, also referred to as the i^{th} mode shape for the elastic body. The complete eigenvector matrix $\Phi := [\phi_1 \ \phi_2 \ \dots \ \phi_n]$ enables transformation of the system into its modal form. Let the structural deformations be expressed in terms of mode shapes as $\delta = \Phi\eta$. Using Eq. (2.37) we can write

$$\underbrace{\Phi^T M \Phi}_{M_{mod}} \ddot{\eta} + \underbrace{\Phi^T K \Phi}_{K_{mod}} \eta = \underbrace{\Phi^T F}_{F_{mod}} \quad (2.39)$$

where Φ^T has been pre-multiplied on both sides. This transformation results in the diagonalization of both mass and stiffness matrices, resulting in modal matrices M_{mod} and K_{mod} as indicated in Eq. (2.39). η is the vector of modal coordinates and on the right hand side, F_{mod} represents the modal forces. To obtain Eq. (2.39) in the form of equations shown in Eqs. (2.36g), inverse of M_{mod} can be multiplied on both sides of Eq.(2.39). Furthermore, the matrix $M_{mod}^{-1}K_{mod}$ can be expressed in terms of vibrational frequencies as

$$M_{mod}^{-1}K_{mod} = \underbrace{\begin{bmatrix} \tilde{\omega}_1^2 & 0 & \dots & 0 \\ 0 & \tilde{\omega}_2^2 & \dots & 0 \\ 0 & 0 & \ddots & 0 \\ 0 & 0 & \dots & \tilde{\omega}_n^2 \end{bmatrix}}_{\Omega^2} \quad (2.40)$$

Therefore, Eq. (2.39) can be rewritten as

$$\ddot{\eta} + \Omega^2 \eta = M_{mod}^{-1} F_{mod} \quad (2.41)$$

A close inspection of Eq. (2.41) above shows that it is essentially the matrix form of the equations of motion derived in the mean axes for generalized modal coordinates, shown in Eqs. (2.36g). The forcing terms on the right hand side in matrix F_{mod} can be shown as equivalent to the generalized modal force Q_{η_i} , see [29]. Finally, as seen

in the derivation of the equations of motion earlier, the mean axes constraints are defined in terms of mode shapes of the elastic body, thus ensuring that all rigid body modes are orthogonal to the structural modes.

2.2.2 BFF Structural Model

For the BFF model, a linear finite element model is constructed using Euler beams and point masses [10]. The point masses represent payloads and aircraft avionics such as flight computer, GPS system, control surface actuators and so on. Fig. 2.2 shows the finite element model constructed.

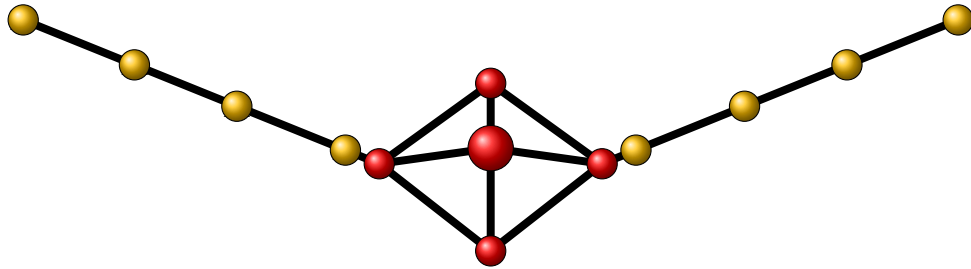


Figure 2.2: Finite Element Model for the BFF Vehicle

The model consists of 14 nodes (including a 'ground' node not shown in Fig. 2.2) interconnected with linear beams. Each node has 3 degrees of freedom allowing the beam to heave, twist and bend, as seen in Fig. 2.3.

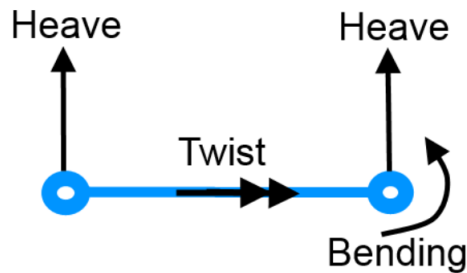


Figure 2.3: Beam Element used in Finite Element Model for BFF Vehicle

The elemental mass and stiffness matrices are given as [41]

$$M_e = \begin{bmatrix} \frac{156m_e}{420} & \frac{22m_eL_e}{420} & 0 & \frac{54m_e}{420} & \frac{-13m_eL_e}{420} & 0 \\ \frac{22m_eL_e}{420} & \frac{4m_eL_e^2}{420} & 0 & \frac{13m_eL_e}{420} & \frac{-3m_eL_e^2}{420} & 0 \\ 0 & 0 & \frac{\chi L_e}{3} & 0 & 0 & \frac{\chi L_e}{6} \\ \frac{54m_e}{420} & \frac{13m_eL_e}{420} & 0 & \frac{156m_e - 22m_eL_e}{420} & 0 & 0 \\ \frac{-13m_eL_e}{420} & \frac{-3m_eL_e^2}{420} & 0 & \frac{-22m_eL_e}{420} & \frac{4m_eL_e^2}{420} & 0 \\ 0 & 0 & \frac{\chi L_e}{6} & 0 & 0 & \frac{\chi L_e}{3} \end{bmatrix} \quad (2.42a)$$

$$K_e = \begin{bmatrix} \frac{12EI_z}{L_e^3} & \frac{6EI_z}{L_e^2} & 0 & -\frac{12EI_z}{L_e^3} & \frac{6EI_z}{L_e^2} & 0 \\ \frac{6EI_z}{L_e^2} & \frac{4EI_z}{L_e} & 0 & -\frac{6EI_z}{L_e^2} & \frac{2EI_z}{L_e} & 0 \\ 0 & 0 & \frac{GJ}{L_e} & 0 & 0 & -\frac{GJ}{L_e} \\ -\frac{12EI_z}{L_e^3} & -\frac{6EI_z}{L_e^2} & 0 & \frac{12EI_z}{L_e^3} & -\frac{6EI_z}{L_e^2} & 0 \\ \frac{6EI_z}{L_e^2} & \frac{2EI_z}{L_e} & 0 & -\frac{6EI_z}{L_e^2} & \frac{4EI_z}{L_e} & 0 \\ 0 & 0 & -\frac{GJ}{L_e} & 0 & 0 & \frac{GJ}{L_e} \end{bmatrix} \quad (2.42b)$$

where m_e is the mass of the beam element, L_e is the length, χ is the mass moment of inertia per unit length, E, G are the Young's and shear modulus respectively, I_z is the second moment of inertia of the cross-section and J is the polar moment of inertia. The structural properties such as the moduli are estimated via static and dynamic ground tests. These tests are described in detail in [15].

Using the elemental mass and stiffness matrices, the overall matrices for the finite element model is assembled to obtain a system of equations as shown in Eq. (2.37). Since each node has 3 degrees of freedom, we obtain matrices of dimension 42×42 . Modal analysis shown in Eq. (2.38) provides 42 mode shapes, out of which the first 6 are rigid body modes. Out of the remaining flexible modes, only the first 12 are retained and the rest are truncated. This provides us with a 12×12 modal mass and stiffness matrix. Using Eq. (2.40), we can then write Eq. (2.41) for the BFF vehicle.

2.2.3 Linearized Equations of Motion

Flutter is typically studied by doing stability analysis for linearized aeroservoelastic models. Body freedom flutter occurs beyond a critical airspeed due to an unstable interaction between the pitching mode and first wing bending mode. To simulate this, equations are obtained for the BFF vehicle by linearizing Eq. (2.36) about a *straight and level* trim condition. The trim condition is taken to be associated with

the undeformed aircraft.

For straight and level flight, let the velocity vector for the instantaneous C.G., the corresponding perturbation velocity and perturbed angular velocity of the mean axes frame be defined as

$$V_{cg} = \begin{bmatrix} U & 0 & W \end{bmatrix}^T \quad (2.43a)$$

$$\Delta V_{cg} = \begin{bmatrix} \Delta u & \Delta v & \Delta w \end{bmatrix}^T \quad (2.43b)$$

$$\Delta \omega = \begin{bmatrix} \Delta p & \Delta q & \Delta r \end{bmatrix}^T \quad (2.43c)$$

The resulting linearized equations based on Eq. (2.36) are

$$M[\Delta \dot{u} + \Delta qW + g\Delta \theta] = \Delta Q_x \quad (2.44a)$$

$$M[\Delta \dot{v} - \Delta pW + \Delta rU - g\Delta \phi] = \Delta Q_y \quad (2.44b)$$

$$M[\Delta \dot{w} - \Delta qU] = \Delta Q_z \quad (2.44c)$$

$$I_{xx}\Delta \dot{p} - (I_{xy}\Delta \dot{q} + I_{xz}\Delta \dot{r}) = \Delta Q_\phi \quad (2.44d)$$

$$I_{yy}\Delta \dot{q} - (I_{xy}\Delta \dot{p} + I_{yz}\Delta \dot{r}) = \Delta Q_\theta \quad (2.44e)$$

$$I_{zz}\Delta \dot{r} - (I_{xz}\Delta \dot{p} + I_{yz}\Delta \dot{q}) = \Delta Q_\psi \quad (2.44f)$$

$$\ddot{\eta}_j + \tilde{\omega}^2 \eta_j = \frac{Q_{\eta_i}}{\mathcal{M}_i} \quad (2.44g)$$

Eqs. (2.44) can be further simplified by taking into account symmetry in the airframe design. Since the aircraft is symmetric about the x-z plane, the terms I_{xy} and I_{yz} within the inertia tensor are zero. Therefore, the rotational rigid body equations of motion may be written in a simplified manner as

$$I_{xx}\Delta \dot{p} - I_{xz}\Delta \dot{r} = \Delta Q_\phi \quad (2.45a)$$

$$I_{yy}\Delta \dot{q} = \Delta Q_\theta \quad (2.45b)$$

$$I_{zz}\Delta \dot{r} - I_{xz}\Delta \dot{p} = \Delta Q_\psi \quad (2.45c)$$

2.3 Summary

In this chapter, the equations required for flutter analysis of the BFF vehicle have been developed using the mean axes approach. Based on the work by Waszak and Schmidt, a Lagrangian approach is used to derive the equations by applying mean axes constraints that simplify the expression for kinetic energy by reducing nonlinear coupling terms to zero. Since those terms inertially couple rigid body and structural dynamics states, this directly results in a decoupled set of equations.

Throughout the derivation, important assumptions and technical points are highlighted and discussed in detail. Certain ambiguous or unclear aspects of the derivation are discussed, and alternate approaches used to address those issues are also described. The work by Keyes, Seiler and Schmidt is discussed in the light of the points highlighted in the derivation. These discussions are included here to provide confidence in the mathematical model used for the BFF vehicle based on the equations derived in the mean axes frame. In the next chapter, aerodynamic modeling for flexible aircraft is discussed.

Chapter 3

Aerodynamic Forces for Flexible Aircraft

In the previous chapter, equations of motion for a flexible aircraft were developed using the mean axes approach. The approach combines rigid body dynamics of the aircraft and its structural dynamics represented via a finite element model. The final set of equations seen in Eq. (2.44) and (2.45) are rewritten here.

$$M[\Delta\dot{u} + \Delta qW + g\Delta\theta] = \Delta Q_x \quad (3.1a)$$

$$M[\Delta\dot{v} - \Delta pW + \Delta rU - g\Delta\phi] = \Delta Q_y \quad (3.1b)$$

$$M[\Delta\dot{w} - \Delta qU] = \Delta Q_z \quad (3.1c)$$

$$I_{xx}\Delta\dot{p} - I_{xz}\Delta\dot{r} = \Delta Q_\phi \quad (3.1d)$$

$$I_{yy}\Delta\dot{q} = \Delta Q_\theta \quad (3.1e)$$

$$I_{zz}\Delta\dot{r} - I_{xz}\Delta\dot{p} = \Delta Q_\psi \quad (3.1f)$$

$$\ddot{\eta}_j + \tilde{\omega}^2\eta_j = \frac{Q_{\eta_i}}{\mathcal{M}_i} \quad (3.1g)$$

The terms appearing on the right hand side are called the generalized forces, and they comprise of the external forces and moments acting on the aircraft. For rigid body dynamics, these forces and moments can be considered in an integrated form i.e. assumed to act at a single point on the body, typically the origin of the body reference frame. However, for structural dynamics modeling, the forces and moments are typically considered in their distributed form across the airframe. If the structural

dynamics is expressed in modal coordinates, as done in Eqs. (3.1) above, the modal forces are computed via transformation of the force and moment distribution across the finite element nodes. Therefore, it is important to obtain external forces and moments in form of their distribution across the nodes of the finite element model at hand.

Throughout the derivation in the previous chapter, it has been assumed that the external force distribution across the finite element model is known as a function of the states of the aircraft. Typically, this includes propulsive forces, gravitational force and aerodynamic forces. Out of these, propulsive forces (or thrust) are not critical for the purposes of studying body freedom flutter since they do not play a significant role in the underlying dynamics, which is primarily based on the coupling of short period mode and first wing bending mode.

Gravity is usually assumed to be acting as a concentrated load at the center of mass and therefore can be handled within the mean axes framework in the same way as it is done for a conventional rigid body dynamics model. However, it should be noted that this approach does not account for structural deformations due to gravitational force. For a moderately flexible aircraft undergoing small vibrations, this approximation is considered valid. Finally, the aerodynamic force distribution for the aircraft is determined via an aerodynamic model. Thus, together with rigid body dynamics and structural dynamics models, aerodynamics modeling forms the third crucial component of flexible aircraft dynamics modeling.

Aerodynamic modeling is a cornerstone of mathematical modeling for aircraft. Equations describing aerodynamic flow are derived from the more general equations representing fluid dynamics [42–44]. These equations are often simplified by keeping in mind the physical aspects of the flow such as compressibility and viscosity. Models predicting aerodynamic forces generated by airflow around finite dimensional lifting surfaces first appeared in the early 1900’s in the form of the Lifting Line Theory developed by Ludwig Prandtl (hence known as Prandtl Lifting Line Theory) [43, 44]. The theory assumes the nature of aerodynamic flow to be irrotational, inviscid and incompressible, which is known as potential flow [43, 44]. Since then, significant progress has been made over the last century in modeling flows under various conditions, ranging from subsonic potential flow to a generally viscous, compressible, and supersonic flow using the more general Navier-Stokes equations [42, 43].

An important flow characteristic for aeroelasticity modeling is its time varying nature. As an aircraft deforms in flight, its aerodynamic shape changes with time, thereby changing the flow characteristics around it. This change in flow characteristics takes place in a finite amount of time and is not instantaneous. Also, it is often required to study the response of flexible aircraft to gust loads and other such time varying flow conditions. Unsteady aerodynamics modeling, which involves computation of the forces exerted on a body in a time dependent air flow, is therefore important for reliable flutter analysis [45,46]. There are several methods available to study unsteady aerodynamics, ranging from advanced, high fidelity Computational Fluid Dynamics (CFD) solvers [47–50] which typically solve the Navier-Stokes equations in discretized form, to potential flow based aerodynamic strip theory, which utilizes 2-D infinite wing assumptions [29,51]. CFD methods provide models with very high number of states which are computationally expensive to simulate and unsuitable for control design. On the other hand, strip theory based methods provide computationally inexpensive models, but they lack the desired fidelity we may require for aeroelastic analysis. Fortunately, potential flow based panel methods [52–54] developed in the 1960s and 1970s successfully fulfill the requirement of modeling techniques which are computationally inexpensive while modeling the lifting characteristics of finite wings with reasonable accuracy. These panel methods are essentially sophisticated extensions of the Lifting Line Theory discussed earlier [44].

For unsteady aerodynamics and flutter analysis, one of the most widely used panel methods is called the Doublet Lattice Method (DLM) [55,56]. The DLM provides low order models for unsteady aerodynamics, which lead to aeroelastic models suitable for control design. This is an attractive feature which is missing from the models obtained from CFD, which although rich in detail, have very large number of states which ultimately make control design infeasible. The only significant disadvantage of the DLM is its inability to model drag, since the method is based on potential flow theory [44,57]. However, since drag does not significantly affect flutter analysis, we choose DLM for modeling unsteady aerodynamics.

The following sections elaborate on the unsteady aerodynamics modeling procedure used for the body freedom flutter vehicle using the DLM. This chapter also addresses a few post-processing steps required to obtain the aerodynamic model suitable for aeroelastic analysis. The final model has to be compatible with the modal structural model developed for the aircraft so that structural deflections due to aerodynamic

loads may be computed. Also, the model has to be continuous in time or frequency domain so that the resulting aeroelastic model can be used to run simulations of flexible aircraft dynamics. These issues are discussed ahead in section I.

3.1 Model Overview

The aerodynamic model for the BFF vehicle is developed using the DLM as the primary modeling tool. As explained in later sections, the DLM essentially provides the time varying aerodynamic force distribution across a lifting surface which is subjected to a time varying flow. The model obtained from the DLM has to be implemented into the overall dynamics model described in Eqs. (3.1). In order to do so, the aerodynamic model has to satisfy two requirements which are

1. Since Eqs. (3.1) are continuous, the aerodynamic model should be continuous in time as well. This greatly simplifies analysis of the overall model as well as simulation runs.
2. The aerodynamic model has to be in structural modal coordinates to be compatible with Eqs. (3.1). The model has to relate the modal degrees of freedom of the aircraft to the resulting unsteady aerodynamic force distribution expressed in modal coordinates linearly, as described below.

$$F_{\text{modal}}^A(t) = M_{\text{aero}}(t)\eta(t) \quad (3.2)$$

where F_{modal}^A represents modal aerodynamic forces and M_{aero} is the required linear aerodynamic model. It should be remembered that all three variables in Eq. (3.2) are functions of time. This requirement is advantageous since the number of modal degrees of freedom can be limited using modal truncation. Therefore models expressed in modal coordinates have fewer states.

The aerodynamic model obtained from the DLM does not satisfy either of the two requirements. DLM provides a discrete model in frequency domain which is not in modal coordinates. Therefore, a few post-processing steps are undertaken to obtain the aerodynamic model according to the given requirements.

1. A least squares fit is carried out for a set of discrete DLM solutions obtained at different frequencies to obtain a continuous frequency domain model. This

model is analogous to a transfer function, which can be conveniently incorporated into a time domain simulation.

2. A coordinate transformation is carried out using suitable transformation matrices to express the aerodynamic model in modal coordinates. The transformation matrices depend on the nature of the spatial discretization in both structural and aerodynamic models. They help project degrees of freedom associated with the structural grid on to the aerodynamic grid and forces generated on the aerodynamic grid back on to the structural grid.

These steps are discussed in detail in section III. The final model obtained after these post processing steps is analogous to what is shown in Eq. (3.2) but with one important difference - the continuous model obtained is in Laplace domain. This is not a problem since the linear aeroelastic model represented by Eq. (3.1) can be expressed in Laplace domain, thus ensuring a smooth integration of the aerodynamic model into the overall dynamics equations. The following sections describe the entire modeling approach in greater detail.

3.2 Doublet Lattice Method

The DLM is a potential flow based panel method developed in the 1960s by Albano & Rodden [55] to solve for unsteady aerodynamic flow across a lifting surface in frequency domain. It can also efficiently handle multiple surfaces and their interfering effects on one another. The method assumes the flow to undergo harmonic oscillations with respect to a lifting surface. It should be noted that the oscillatory motion is relative in nature. This means that the DLM solution is equally applicable to either the flow oscillating around a fixed surface or the surface oscillating in steady flow. In the case of a flexible aircraft however, the problem is most suitably visualized as a lifting surface oscillating in steady flow. The DLM essentially provides an aerodynamic model in the form of frequency response where input is the harmonically oscillating angle of attack distribution on the lifting surface and output is the resulting pressure distribution.

The DLM is a panel method, which means that the surface is divided into small trapezoidal lifting elements called panels, as shown in Fig. 3.1.

The collection of the panels describing the lifting surface is referred to as the aerody-

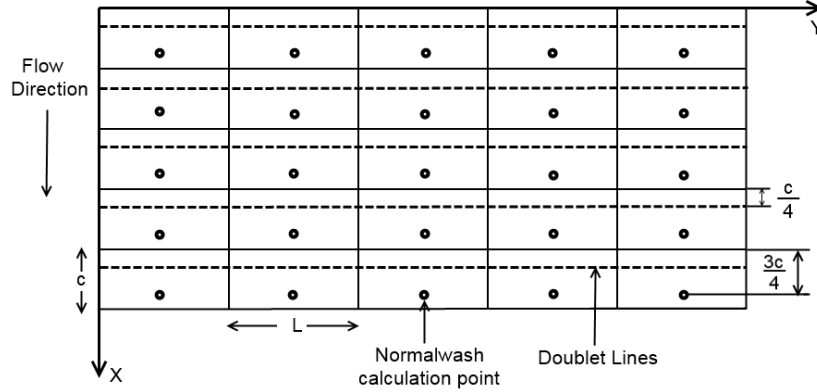


Figure 3.1: A typical discretization of the lifting surface S

namic grid. The dashed lines represent a line of infinitesimal acceleration potential doublets [55,58] at the $1/4^{th}$ chord location of each panel. The doublet line simulates the pressure difference across the lifting surface for each panel. The points located at the $3/4^{th}$ chord location of each panel is the normalwash calculation point or the collocation point [44, 55]. Normalwash is defined as flow normal to the surface at a given point, normalized by free stream flow speed. Normalwash can be induced due to the doublet lines or generated due to the external free stream flow. The strength of a doublet line determines the normalwash it induces at any given point. On the other hand, if the surface shown in Fig. 3.1 oscillates in pitch about the leading edge (Y axis) with a given frequency and small amplitude, each panel experiences a normalwash proportional to the distance from Y axis due to free stream flow. DLM essentially uses this normalwash distribution to calculate the pressure differences across these panels.

There are a number of equations which need to be solved in order to relate the normalwash distribution to the corresponding pressure distribution [55, 59]. These equations also involve a few simplifying approximations. In the interest of keeping the chapter focused on application of the DLM for aeroelasticity, the relevant equations and their simplifications for obtaining results discussed ahead have been provided in Appendix A.1. The following subsections provide an overview of the method and the final model obtained.

3.2.1 Aerodynamic Influence Coefficients Matrix

The objective of the DLM is to find the relation between normalwash distribution due to free stream on a lifting surface and the resulting pressure distribution as the surface undergoes oscillatory motion at a given frequency. The first step towards this computation is discretization of the surface into panels as mentioned earlier. Also, as mentioned earlier and indicated in Fig. 3.1, a doublet line is assumed at the quarter-chord of each panel. Since pressure difference across a panel is directly related to the strength of its doublet line, the flow induced due to the doublet line at any point can be written in terms of the pressure difference it generates.

The next step is to compute the normalwashes induced due to each doublet line at all the normalwash calculation points on the surface and assemble the so called downwash matrix D . The normalwash induced at the i^{th} panel due to a doublet line on the j^{th} panel in terms of the pressure difference generated by the doublet line is given by the line integral

$$w_{ij} = \frac{c_j}{8\pi} \int_{-\frac{L}{2}}^{\frac{L}{2}} K(x_i, y_i, \xi_j(l), \sigma_j(l), \omega, V) \Delta p_j dl \quad (3.3)$$

where going from left to right,

1. w_{ij} : induced normalwash at i^{th} panel due to the doublet line on the j^{th} panel
2. c_j : chord length of the j^{th} panel
3. K : Kernel function which relates the normalwash induced by an infinitesimal acceleration doublet to the pressure difference across it
4. (x_i, y_i) : coordinates of the normalwash calculation point of the i^{th} panel
5. (ξ_j, σ_j) coordinates along the doublet line of the j^{th} panel
6. ω : given oscillating frequency of the lifting surface
7. V : free stream velocity
8. Δp_j : harmonically varying pressure difference across the doublet line on the j^{th} panel

The pressure difference is assumed to be spatially constant across each panel, which is reasonable for sufficiently small panels. Total normalwash at the i^{th} panel can now be written by summing Eq. (3.3) for all panels and written as

$$w_i = \sum_{j=1}^{j=N_p} D_{ij} \Delta p_j \quad (3.4a)$$

$$D_{ij} = \frac{c_j}{8\pi} \int_{-\frac{L}{2}}^{\frac{L}{2}} K(x_i, y_i, \xi_j(l), \sigma_j(l), \omega, V) \quad (3.4b)$$

where N_p is the total number of panels on the lifting surface. It should be noted that since the pressure difference Δp_j is a harmonic function, the resulting induced normalwash w_i is a harmonic function as well. Finally, Eq. (3.3) can be rewritten in matrix form to realize the downwash matrix D as

$$\bar{w}_{\text{ind}} = D\bar{p} \quad (3.5)$$

where \bar{w}_{ind} is the normalwash vector of dimensions $N_p \times 1$ containing total induced normalwash at each panel due to all doublet lines, D is a complex valued matrix of dimensions $N_p \times N_p$ containing all the entries D_{ij} , and \bar{p} is the pressure difference vector dimensions $N_p \times 1$ containing pressure distribution across the panels. Since D_{ij} only depends on the relative location of the panels and known flow conditions, Eq. (3.4) can be evaluated a priori for a given lifting surface. The computation involves integrating the kernel function K along each doublet line, the relevant equations for which may be found in Appendix A.1. However, an important aspect of these equations is that they allow for the oscillating frequency and free stream velocity to be combined into a single non-dimensional parameter called the reduced frequency, given by

$$k = \frac{\omega \bar{c}}{2V} \quad (3.6)$$

where \bar{c} is the reference chord length of the the aircraft under consideration. Thus, for a given panel grid, the D matrix is only a function of the reduced frequency. The matrix D maps the pressure difference across all panels due to their doublet lines to the induced normalwash distribution across the panels. However, it should be remembered that for the problem at hand, it is the pressure difference vector

which is actually the unknown quantity to be computed. This is accomplished by first inverting the downwash matrix to obtain the so called Aerodynamic Influence Coefficients (*AIC*) matrix so that the pressure distribution vector may now be written as

$$\bar{p} = [AIC(k)]\bar{w}_{\text{ind}} \quad (3.7)$$

Next, we apply the zero net normal flow boundary condition to relate the induced normalwash vector \bar{w}_{ind} to the normalwash distribution due to free stream normalwash \bar{w}_{∞} . The zero net normal flow boundary condition enforces the physical constraint that there cannot be any flow perpendicular to the solid lifting surface. Although this condition should ideally be satisfied across the entire surface, in practice it is only satisfied at the normalwash calculation points due to discretization of the surface. According to the condition, normalwash induced due to the doublet lines must exactly cancel out the normalwash due to free stream, as shown.

$$\bar{w}_{\text{ind}} + \bar{w}_{\infty} = 0 \quad (3.8)$$

From Eqs. (3.7) and (3.8) we get

$$\bar{p} = -[AIC(k)]\bar{w}_{\infty} \quad (3.9)$$

The negative sign will be henceforth assumed to be absorbed into the free stream normalwash vector \bar{w}_{∞} for convenience. However, it should be kept in mind for correct results from the DLM. \bar{w}_{∞} is computed separately using the given flow condition and motion of the lifting surface. For small angles, it is identical to the angle of attack on the panels. Eq. (3.9) achieves the objective of mapping free stream normalwash distribution to the resulting pressure distribution for a harmonically oscillating lifting surface. It should be noted that both \bar{p} and \bar{w}_{∞} are harmonic functions in ω , the oscillating frequency.

From Eq. (3.9) we can see that \bar{w}_{∞} contains normalwashes of each individual panel. Although the method may appear to assume rigid motion of the entire lifting surface, in fact there is no such constraint on the motion of the panels while computing the *AIC* matrix. In other words, if an elastic deformation of the surface can be approx-

imately discretized in terms of motion of the panels, the corresponding normalwash vector can be computed and Eq. (3.9) can be readily used to obtain the pressure distribution across those panels. This is the main philosophy behind using the DLM for aerodynamic modeling of flexible aircraft. The representation of elastic deformations in terms of the motion of aerodynamic grid panels is discussed in detail in the later sections. The aerodynamic force distribution can be easily calculated from pressure distribution as shown in Eq. (3.10).

$$F_{\text{aero}}(k) = \bar{q}S_p[AIC(k)]\bar{w} \quad (3.10)$$

where \bar{q} is the free stream dynamic pressure and S_p is a diagonal matrix containing the panel areas. It should be kept in mind that the force distribution given by F_{aero} acts at the midpoint of the doublet line on each panel.

3.2.2 Correction to Steady Solution

Since the DLM involves several simplifying assumptions and approximations, the resulting model is also accurate only up to a certain level of approximation. However, it has been found in practice that the steady solution obtained at zero oscillating frequency for a given aerodynamic grid is not as accurate as the solution obtained from other established panel methods such as the Vortex Lattice Method (VLM) [44,55,56]. Therefore, if a steady state solution is available for the same grid from a more accurate method, it is desirable to improve the accuracy of the DLM using that solution. Thus, a composite aerodynamic model can be envisaged where the unsteady effects computed via the DLM are superimposed on to a steady solution from a more accurate method such as the VLM, as described by Rodden et al in [56].

First, the incremental downwash matrix is calculated for a given frequency using the DLM which represents the unsteady part of the flow solution. This is done by computing the matrix twice, once at the given frequency and again for frequency set to zero. The incremental downwash matrix is then given by

$$D_{\text{uns}}(k) = D_{\omega}(k) - D_0 \quad (3.11)$$

where D_{uns} is the incremental downwash matrix representing unsteady effects, D_{ω} is the complete downwash matrix computed at the given frequency ω and D_0 is the

complete downwash matrix computed at zero frequency. Thus, the steady solution of the DLM is effectively removed from the overall downwash matrix at a given frequency.

The steady state downwash matrix is separately constructed, typically using a panel method such as the VLM. The VLM uses horseshoe shaped vortex lines placed at quarter-chord of each panel to model the pressure distribution, analogous to the doublet lines used in DLM. It is vital to use the same aerodynamic grid for the VLM so that the resulting steady state downwash matrix is compatible to the one obtained from DLM. The new, improved *AIC* matrix is now computed as

$$D_{\text{tot}}(k) = D_{\text{VLM}} + D_{\text{uns}}(k) \quad (3.12a)$$

$$[AIC(k)] = D_{\text{tot}}^{-1}(k) \quad (3.12b)$$

where D_{VLM} is downwash matrix computed from the VLM. This *AIC* matrix now enables an aerodynamic model which exactly converges to the VLM solution for steady state.

As mentioned earlier, in order to use this aerodynamic model in aeroelasticity modeling, it is necessary to be able to express the free stream normalwash distribution vector \bar{w}_∞ in terms of elastic deformation of the lifting surface. This enables the calculation of aerodynamic loads on a deforming aircraft. Also, since the aerodynamic model is available at discrete frequencies, it is desirable to have a model as a continuous function of frequency. These issues are discussed in the next section.

3.3 Continuous Aerodynamic Model in Modal Coordinates

As described in the previous section, DLM provides aerodynamic force distribution for a given normalwash distribution on an aerodynamic grid at a particular oscillating frequency. However, the aerodynamic model should be able to effectively interact with the corresponding structural model built for the aircraft to produce coupled aeroelastic phenomena such as flutter. Hence, there has to be a way to generate normalwash distribution for a given elastic deformation which is provided by the structural grid. Also, the effect of aerodynamic forces computed in Eq. (3.10) on the

structural grid has to be determined. Finally, we need a continuous frequency domain model to carry out aeroelastic analysis as desired. In this section, we address these issues with the help of an example problem. Consider a surface with just four panels, as shown in Fig. 3.2.

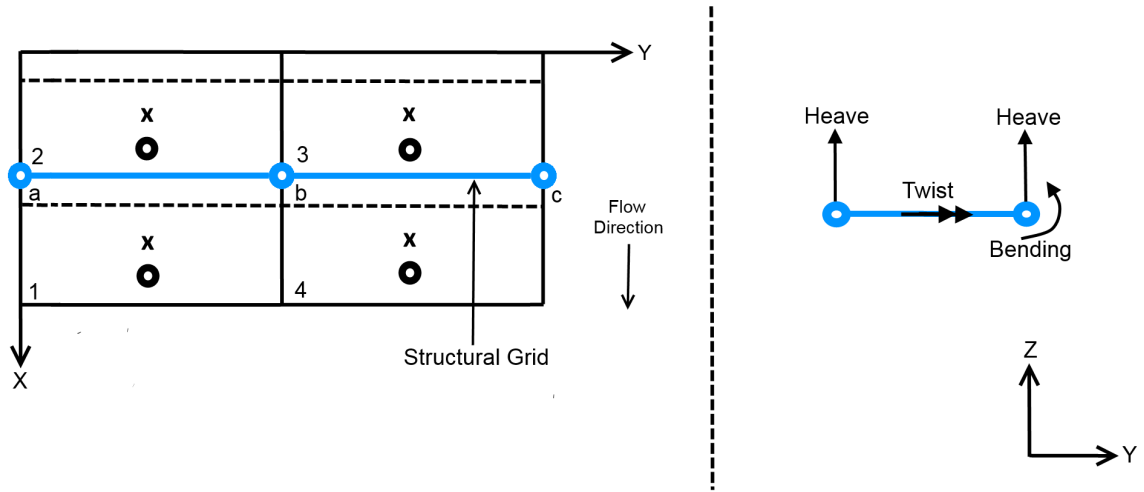


Figure 3.2: The 2×2 grid example in top view, with a superimposed structural model

Fig. 3.2 shows a finite element (FE) grid created for the lifting surface, superimposed on the aerodynamic grid used in the unsteady aerodynamics model. The FE grid is similar to the one described for the BFF aircraft in section II. As seen in the figure, beam elements interconnecting the three nodes are allowed to bend about the x-axis, twist about the y-axis and heave in the direction of z-axis, giving a total of 3 degrees of freedom (DoF) to each of the nodes a, b and c . For the aerodynamic panels, 2 DoF each are considered which are pitch about centerline of each panel parallel to Y axis and heaving motion, which result in a normalwash due to free stream flow. We need a way to project the DoF of the structural grid on to the aerodynamic panels so that the normalwash vector may be calculated for a given elastic deformation. This is done by computing suitable transformation matrices, which is discussed ahead.

3.3.1 Grid Interpolation

Grid interpolation techniques are required to relay information between the aerodynamic grid and structural grid. Specifically, deformations of the aircraft under a given loading predicted by the structural grid have to be projected on the aerodynamic grid. In the other direction, aerodynamics loads computed on the aerodynamic grid need to be transmitted on to the structural grid. If we consider linear interpolation, we

can express them in terms of suitable transformation matrices as

$$u_{\text{aero}} = T_{as} u_{\text{struc}} \quad (3.13a)$$

$$F_{\text{struc}} = T_{sa} \mathcal{F}_{\text{aero}} \quad (3.13b)$$

where u_{struc} , u_{aero} are DoF of the structural nodes and aerodynamic panels respectively, F_{struc} and $\mathcal{F}_{\text{aero}}$ are loads acting on structural grid and aerodynamic grid respectively, and T_{as} , T_{sa} are the relevant transformation matrices between them. Now, u_{aero} is assumed to consist of heave and pitch of the aerodynamic panels about their midpoints marked out in Fig. 3.2 as crosses. Also, unlike F_{aero} in Eq. (3.10), $\mathcal{F}_{\text{aero}}$ consists of lift and pitching moments on each of the panels about their midpoints.

Although it may seem that two different transformation matrices are required, it can be proven that T_{as} and T_{sa} are in fact transpose of one another. This follows from the assertion that projection of aerodynamic loads on to the structural grid requires structural equivalence. Structural equivalence means that the system of loads F_{struc} and $\mathcal{F}_{\text{aero}}$ deflect the structure identically [60,61]. It should be noted that this may not necessarily lead to static equivalence. To enforce structural equivalence, we equate the virtual work done by both systems of forces. Let δu_{aero} and δu_{struc} be virtual displacements corresponding to aerodynamic and structural grids respectively. Then from structural equivalence as well as Eq. (3.13)(a) we have

$$\delta u_{\text{struc}}^T F_{\text{struc}} = \delta u_{\text{aero}}^T \mathcal{F}_{\text{aero}} \quad (3.14)$$

where

$$\delta u_{\text{aero}} = T_{as} \delta u_{\text{struc}} \quad (3.15)$$

Therefore we have

$$\delta u_{\text{struc}}^T [F_{\text{struc}} - T_{as}^T \mathcal{F}_{\text{aero}}] = 0 \quad (3.16a)$$

$$F_{\text{struc}} = T_{as}^T \mathcal{F}_{\text{aero}} \quad (3.16b)$$

Comparing Eq. (3.16)(b) with Eq. (3.13) we see that the two transformation matrices are transpose of one another. Therefore it is sufficient to compute the matrix in one direction.

As indicated in Eq (3.13), let u_{struc} be the set of structural deformations for the structural grid in Fig 3.2. To project this set of nodal displacements on to the aerodynamic model, surface spline theory for thin surfaces is used, see [62]. The NASTRAN User Guide [60] uses this technique as well, and has served as the source for its implementation for the BFF aircraft. The surface spline theory is essentially a mathematical tool for interpolating between a given set of deformations using thin plate deformation equations. It involves solving for the unknown deformations at desired locations of an infinite thin plate, given a set of deformations at known locations. Therefore, interpolation between the two grids is a two step process. The first step involves representing the structural deformations as a set of deformations on an infinite thin plate. The second step then uses the surface spline method to interpolate for deformations at locations corresponding to aerodynamic panels midpoints using the known deformations from the structural grid.

An infinitely thin plate deforms only in the direction normal to the surface, as shown in a representative figure Fig. 3.3.

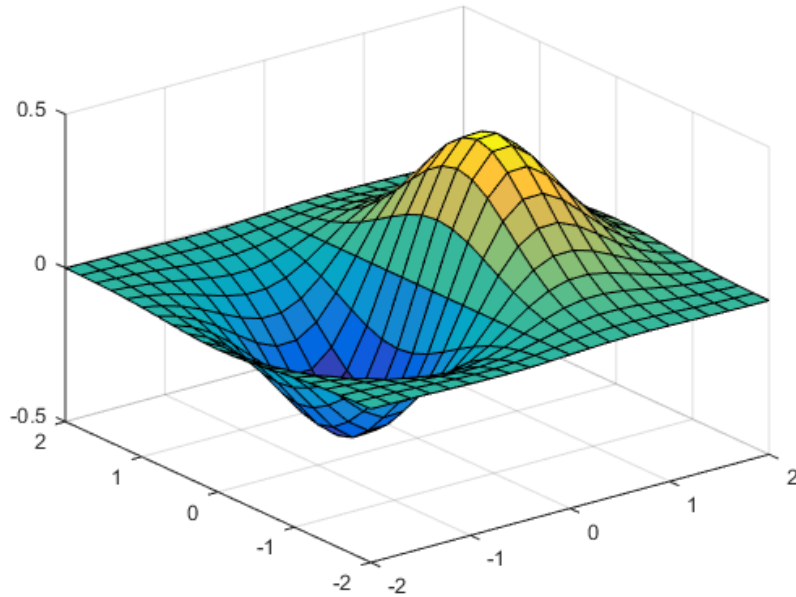
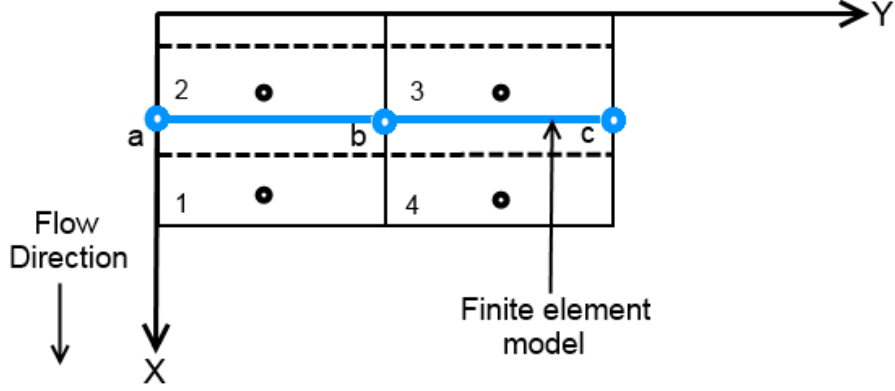


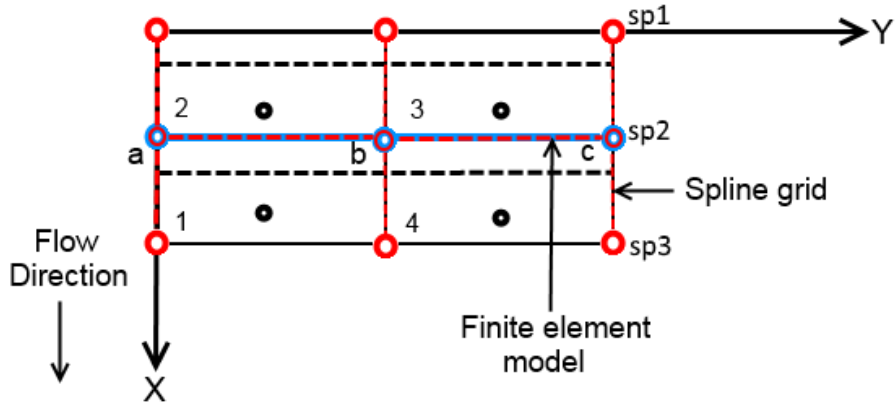
Figure 3.3: A representative infinite thin plate deformation

Since a thin plate is constrained to deform only in the direction normal to its surface, it becomes necessary to represent deformations of the given structural grid purely in terms of heave. In the example problem in Fig. 3.2, the structural nodes can be seen

to have rotational deformations (bending and twist) in addition to heave. Therefore, in order to obtain an equivalent set of purely heave deformations, a so called spline grid is constructed based on the existing structural grid as shown in Fig. 3.4.



(a) Structural grid



(b) Spline grid

Figure 3.4: Spline grid construction

Each of the red connections of the spline grid is assumed to be stiff. The purpose of the spline grid is to transform all the DoF of a node on the structural grid into pure heaving motion of the spline grid nodes attached to it. For example, DoF of the node c can be represented as heaving motion of the spline nodes attached to node c as

$$\begin{bmatrix} h_{sp1} \\ h_{sp2} \\ h_{sp3} \end{bmatrix} = \begin{bmatrix} 1 & 0 & c_3 \\ 1 & 0 & 0 \\ 1 & 0 & -c_4 \end{bmatrix} \begin{bmatrix} h_c \\ \theta_c \\ \chi_c \end{bmatrix} \quad (3.17)$$

where h_{spi} is the heave of the i^{th} spline node for $i = 1, 2,$ and 3 as indicated in Fig. 3.4

(b). $\{h_c, \theta_c, \chi_c\}$ are the heave, bending and twist DoF of node c , c_3 and c_4 are the chord lengths of panel 3 and panel 4. Of course, this is only valid for small deflections, but then so is the linear structural model. The overall transformation matrix can be built in a similar manner covering structural nodes a , b and c . We assume this intermediate transformation to be represented by the matrix T_{spline} . Therefore we get

$$u_{\text{spline}} = T_{\text{spline}} u_{\text{struc}} \quad (3.18)$$

where u_{spline} contains the set of purely heaving deformations of the spline grid. Since the structural model has a total of 9 DoF (3 DoF per node) and the spline grid also has 9 DoF (1 DoF per node), the matrix T_{spline} is of dimension 9×9 . Now, using the surface spline theory, we can obtain deformations at the locations of aerodynamic panel midpoints using the known deformations of the spline grid. This interpolation operation can be expressed in the form of a matrix T_{plate} . For further details on theory and construction of the matrix T_{plate} , see [60, 62]. We can now evaluate T_{as} as

$$T_{as} = [T_{\text{plate}}] [T_{\text{spline}}] \quad (3.19)$$

Thus, we obtain T_{as} matrix which projects the structural grid deformation on to the aerodynamic panels in form of their pitch and heave in a linear manner, which is valid for small deformations. Since each panel has 2 DoF, the overall aerodynamic grid has 8 DoF. Therefore, the dimension of T_{as} in this example would be 8×9 . This approach can be generalized for interpolation between any given aerodynamic and structural grid.

3.3.2 Generalized Aerodynamics Matrices

In the previous subsection, interpolation between the structural and aerodynamic grid has been described. Using the transformation matrix obtained, the aerodynamic loads can be easily written as a function of structural deformations. The loads can then be projected on to the structural grid as well. However, looking back at the equations of motion developed in chapter 2 (Eq. (2.45)), it can be seen that the structural dynamics are represented in generalized modal coordinates. Therefore it is necessary to obtain the aerodynamic model in modal coordinates as well. This enables the computation of aerodynamic forces in the coordinate system compatible

with the modal structural model. The objective is to obtain a matrix which maps the modal deflections to the resulting aerodynamic loads expressed as modal forces. This matrix is called the Generalized Aerodynamics Matrix (GAM). Its construction involves the use of the *AIC* matrix obtained from DLM, transformation matrix T_{as} for grid interpolation and mode shapes obtained from the structural model, as described in chapter 2.

To compute aerodynamic loads for a given structural deformation, the corresponding normalwash distribution is required. The transformation matrix T_{as} converts the structural deformations u_{struc} into motion of the aerodynamic panels u_{aero} as seen in Eq. (3.13)(a). The next step therefore is to calculate the normalwash on panels due to their pitch and heave motion. This is done by constructing the so called differentiation matrices D_1 and D_2 as shown in [59, 63]. D_1 matrix maps the panel displacement and orientation to the downwash at normalwash calculation point, while D_2 does the same for the panel velocity. For the example in Fig. 3.2, the DoF for panel 1 denoted as u_{aero}^1 and the resulting downwash can be written as

$$u_{\text{aero}}^1 = \begin{bmatrix} \theta_1 \\ h_1 \end{bmatrix} \quad (3.20a)$$

$$w_1 = D_1 u_{\text{aero}}^1 + D_2 \dot{u}_{\text{aero}}^1 \quad (3.20b)$$

where θ_1 and h_1 are the pitch and heave displacements respectively and w_1 is the total normalized downwash at panel 1 due to DoF of panel 1. It can be deduced that a heave displacement does not have any contribution to downwash at the normalwash calculation point. However, a pitch displacement results in an equal amount of downwash for small angles, since rotation of a panel about its pitch axis results in a net perpendicular flow at the normalwash calculation point. Similarly, both heave velocity (\dot{h}_1) and pitch rate ($\dot{\theta}_1$) induce normalwash at the collocation point given by $-\dot{h}_1/V$ and $\dot{\theta}c_1/4V$, respectively. Here, c_1 is the chord length of panel 1. Thus, the D_1 and D_2 matrices and the total normalwash expression can be written as

$$D_1 = [1 \quad 0] \quad (3.21a)$$

$$D_2 = \frac{2}{\bar{c}} \begin{bmatrix} c_1 & \\ & -1 \end{bmatrix} \quad (3.21b)$$

$$w_1 = D_1[\theta_1 \quad h_1]^T + D_2[\dot{\theta}_1 \quad \dot{h}_1]^T \frac{\bar{c}}{2V} \quad (3.21c)$$

In D_2 , we normalize the matrix with the reference chord \bar{c} which also appears in the expression for reduced frequency as seen in Eq. (3.6). This is done so that the factor $\bar{c}/2V$ can be isolated as seen in Eq. (3.21)c. Since θ_1 and h_1 are harmonic functions of frequency ω , we can rewrite $\dot{\theta}_1$ and \dot{h}_1 as shown.

$$\theta_1 = \theta_0 e^{i\omega t} \quad (3.22a)$$

$$h_1 = h_0 e^{i\omega t} \quad (3.22b)$$

$$\dot{\theta}_1 = i\omega\theta_1 \quad (3.22c)$$

$$\dot{h}_1 = i\omega h_1 \quad (3.22d)$$

Equation 3.21c can now be rewritten in terms of these Fourier transforms as

$$w_1 = (D_1 + ikD_2)[\theta_1 \quad h_1]^T \quad (3.23)$$

Here we have used Eq. (3.6) to express the normalwash of panel 1 as a function of reduced frequency k . We can similarly compute D_1 and D_2 matrices for all the other panels and combine them in a block diagonal manner to obtain the overall differentiation matrices. From here on, D_1 and D_2 matrices would refer to the overall block diagonal matrices developed for all the panels. Using D_1 and D_2 , in combination with the transformation matrix T_{as} , the free stream normalwash vector distribution vector can now be written in terms of elastic deformations as

$$\bar{w}_\infty = (D_1 + ikD_2)T_{as}u_{\text{struc}} \quad (3.24)$$

Combining Eq. (3.10) and Eq. (3.24), the aerodynamic load distribution at the

quarter-chord point of each panel can be written in terms of structural deformations as

$$F_{\text{aero}}(k) = \bar{q}S_p[AIC(k)](D_1 + ikD_2)T_{as}u_{\text{struc}} \quad (3.25)$$

As discussed earlier in the subsection, it is necessary to obtain aerodynamic loads in terms of generalized modal coordinates, since the equations of motion using mean axes are also expressed in those coordinates. Any deformation of the structural grid given by u_{struc} can be written in terms of mode shapes and generalized coordinates as

$$u_{\text{struc}} = \sum_j^{N_\Phi} \Phi_{f_j} \eta_{f_j} \quad (3.26)$$

where Φ_{f_j} are the flexible mode shapes and N_Φ is the finite number of mode shapes taken into account. The mode shapes are computed by solving the eigenvalue problem shown in Eq. (2.38). Combining Eq. (3.25) and Eq. (3.26), we get

$$F_{\text{aero}}(k) = \bar{q}S_p[AIC(k)](D_1 + ikD_2)T_{as}\Phi_f\eta_f \quad (3.27)$$

where Φ_f is the eigenvector matrix containing all the flexible mode shapes and η_f is the generalized flexible modal coordinates vector. Next, the aerodynamic forces obtained in Eq. (3.27) need to be projected on to the structural grid and then transformed into modal forces as required for the equations of motion shown in Eq. (2.45). Although it has been established that the reverse transformation matrix from forces on aerodynamic grid to structural grid is simply the transpose of T_{as} (see Eq. (3.16)), it has to be remembered that the reverse transformation is only applicable to loads acting at panel midpoints, given by $\mathcal{F}_{\text{aero}}$. Therefore, there is an intermediate transformation required which moves the force distribution F_{aero} acting at panel quarter-chords to panel midpoints. Of course, to maintain static equivalence, a pitching moment will also be added about the midpoints of each panel. For panel 1 in the example considered, this matrix can be written as

$$\underbrace{\begin{bmatrix} F_1 \\ M_1 \end{bmatrix}}_{\mathcal{F}_{\text{aero}}^1} = \underbrace{\begin{bmatrix} 1 \\ c_1 \\ 4 \end{bmatrix}}_{T_{\mathcal{F}}} F_{\text{aero}}^1 \quad (3.28)$$

where F_{aero}^1 is the force acting at the quarter-chord point on panel 1 and $\mathcal{F}_{\text{aero}}^1$ is the equivalent force and moment at the midpoint of the panel. The matrix $T_{\mathcal{F}}$ can be constructed in a block diagonal manner for all panels, denoted $T_{D\mathcal{F}}$. Now, matrix T_{as}^T can be used to transform the force distribution on aerodynamic grid into an equivalent distribution on the structural grid as

$$F_{\text{struc}}(k) = \bar{q} T_{as}^T \underbrace{T_{D\mathcal{F}} S_p}_{S} [AIC(k)] (D_1 + ikD_2) T_{as} \Phi_f \eta_f \quad (3.29)$$

Since $T_{D\mathcal{F}}$ only depends on panel geometry, it can be combined with S_p as a simplifying step to obtain the overall matrix S , as shown above. The last step involves transforming the force distribution on the structural grid into modal forces. This is accomplished using the transpose of the mode shape matrix, as seen in Eq. (2.39). Therefore, we can finally write the aerodynamic forces in the modal form, as a function of generalized modal deflections as

$$F_{\text{modal}}(k) = \bar{q} \Phi_f^T T_{as}^T S [AIC(k)] (D_1 + ikD_2) T_{as} \Phi_f \eta_f \quad (3.30)$$

From Eq. (3.30), the Generalized Aerodynamics Matrix (GAM) can be identified as

$$Q(k) = \Phi_f^T T_{as}^T S [AIC(k)] (D_1 + ikD_2) T_{as} \Phi_f \quad (3.31)$$

Therefore, in terms of the GAM, Eq. (3.30) can be rewritten as

$$F_{\text{modal}}(k) = \bar{q} [Q(k)] \eta_f \quad (3.32)$$

In other words, the GAM is the unsteady aerodynamic model expressed in the structural modal coordinates. Inspecting Eq. (3.31), we find that the dimensions of a GAM are $N_{\Phi} \times N_{\Phi}$. It should be noted that although the structural grid, spline grid and the aerodynamic grid in the example have a similar number of DoF, the method described

in this section is applicable even when the grids have DoF orders of magnitude apart as we know is the case with the BFF aircraft. In fact, since it often happens that the structural grid is of much lower dimensions compared to an aerodynamic grid, the GAMs obtained are also of much lower dimensions since N_{Φ} is essentially a function of the structural grid size. Also, the size may be further reduced by truncating higher modes in the structural model.

Finally, the case of rigid body modes and the associated aerodynamic forces has to be addressed. Eq. (3.31) only involves the flexible mode shapes Φ_f resulting in aerodynamic forces F_{modal} which excite vibrational modes. To obtain rigid body forces and moments in the same way, the rigid body mode shapes Φ_r may be used. These mode shapes are also obtained as a part of the eigensolution of the structural model. However, the modes obtained may not be in the directions associated with the mean axes assumed for the dynamic model in Eq. (3.1). Therefore, the rigid body modes obtained from solving the eigenvalue problem are discarded and reconstructed in the required directions. These rigid body mode shapes are now augmented with the flexible mode shapes as shown

$$\Phi = [\Phi_r \ \Phi_f] \quad (3.33)$$

Therefore the overall aerodynamic force may now be written as

$$\underbrace{\begin{bmatrix} F_{\text{rigid}} \\ F_{\text{modal}} \end{bmatrix}}_{F(k)} = \bar{q} \Phi^T T_{as}^T S[AIC(k)] (D_1 + ikD_2) T_{as} \underbrace{\Phi}_{\eta} \begin{bmatrix} \eta_r \\ \eta_f \end{bmatrix} \quad (3.34)$$

3.3.3 Rational Function Approximation

The GAMs are obtained for discrete reduced frequencies. However, a continuous model is required for time domain aeroelastic simulations and analysis using Eqs. (3.1). Several methods have been developed to obtain such models [64–66] from the frequency response data. Roger’s method [64] is one of the most prevalent methods used for this purpose. It is called rational function approximation (RFA) which basically involves a function fitting for the aerodynamic model data obtained at various reduced frequencies.

Assuming the *AIC* matrices have been computed for a set of m reduced frequencies $\kappa := \{k_1, k_2 \dots k_m\}$, we would now like to fit that data to a predetermined continuous basis function. In the interest of keeping the continuous model analogous to a transfer function, the basis function is defined in terms of reduced frequency Laplace variable $s_k := s \frac{\bar{c}}{2V}$ where s is the usual Laplace variable. The basis function is defined keeping in mind the physical aspects of unsteady flow seen in aeroelasticity, such as added mass effects due to flow acceleration and aerodynamic lag effects. The basis function for fitting the *AIC* matrices is

$$A(s_k) = A_0 + s_k A_1 + \sum_{j=1}^l A_{j+1} \frac{s_k}{s_k + p_j} \quad (3.35)$$

where A_0 represents the steady state aerodynamic effects, A_1 represents the added mass effects and A_{j+1} represents the lag terms associated with the unsteady flow. p_j are a set of l poles which are selected a priori. The fitting can be carried out in a simple least squares manner, determining the values of the matrix coefficients. The fitting is carried out only along the imaginary axis so that substituting $s_k = ik$ returns the *AIC* matrix associated with reduced frequency k . Therefore, the continuous model $A(s_k)$ is only actually valid for zero damping conditions, which agrees with the assumptions of undamped harmonic oscillations of the lifting surface for DLM. This aspect of the model becomes important in flutter analysis, as discussed in later chapters. Also, from the definition of the reduced frequency variable s_k , it can be seen that the continuous model $A(s_k)$ in Eq. (3.35) can be written as a transfer function in s , which is parametrically dependent on airspeed V . As we see later, this results in a parametrically dependent linear model obtained from Eqs. (3.1).

To obtain continuous GAMs from this point, we carry out coordinate transformations for $A(s_k)$ in the same way as indicated in the previous subsection in Eq. (3.31). Therefore, continuous GAM, after some algebraic manipulation, is obtained as

$$Q(s_k) = \Phi^T T_{as}^T S \left[A_0 D_1 + (A_0 D_2 + A_1 D_1 + \sum_{j=1}^l A_{j+1} D_2) s_k + A_1 D_2 s_k^2 + \sum_{j=1}^l A_{j+1} (D_1 - D_2 p_j) \frac{s_k}{s_k + p_j} \right] T_{as} \Phi \quad (3.36)$$

It can be seen that Eq. (3.36) has a quadratic term in s_k with matrix coefficient $A_1 D_2$. This term essentially represents the effects of flow acceleration. We can now express the aerodynamic loads due to structural deformations as a continuous model in frequency domain in terms of generalized modal coordinates using Eq (3.32). The loads themselves are obtained in the modal form as

$$F_{\text{modal}}(s_k) = \bar{q}[Q(s_k)]\eta \quad (3.37)$$

From the definition of s_k we see that $F_{\text{modal}}(s_k)$ is a function of Laplace variable s and airspeed V . In this form, it can be used in the equations of motion in Eq. (2.45). We note that in Eq. (3.36), quadratic terms in s_k appear since the GAM maps structural deformations (which are essentially displacements) to modal forces. $A(s_k)$ on the other hand maps normal washes, which are velocities, to aerodynamic loads. Hence Eq. (3.35) has only linear terms in s_k denoting flow accelerations. Inspecting Eq. (3.36), we find that $Q(s_k)$ can be expressed as a sum of smaller constituents which are

$$Q_{\text{steady}}(s_k) = \Phi^T T_{as}^T S [A_0 D_1 + A_0 D_2 s_k] T_{as} \Phi \quad (3.38a)$$

$$Q_{\text{AddM}}(s_k) = \Phi^T T_{as}^T S \left[(A_1 D_1 + \sum_{j=1}^l A_{j+1} D_2) s_k + A_1 D_2 s_k^2 \right] T_{as} \Phi \quad (3.38b)$$

$$Q_{\text{Lag}}(s_k) = \Phi^T T_{as}^T S \left[\sum_{j=1}^l A_{j+1} (D_1 - D_2 p_j) \frac{s_k}{p_j + s_k} \right] T_{as} \Phi \quad (3.38c)$$

where Q_{steady} represents steady aerodynamics, Q_{AddM} is the unsteady added mass effects and Q_{Lag} are the unsteady aerodynamic lag effects. Separating out these constituents allows for independent access to each of them, allowing for specific improvements in accuracy in any of them if possible. For example, if a more accurate steady aerodynamics model is available, Q_{steady} can be replaced with it to improve model accuracy.

A drawback of the approach outlined above for continuous aerodynamic models is that the *AIC* matrices which are used for the RFA can have significantly large dimensions. A much easier and more accurate way of obtaining the continuous model is to carry out the fitting *after* the construction of GAMs. In this approach, GAMs are first

constructed from the AIC matrices obtained for the reduced frequency set κ , following Eq. (3.30). The m GAM data points are then fitted to a rational function basis defined using the same variable s_k . The structure of the basis function however is slightly different. As pointed out earlier, GAMs map deformations, and not normalwashes, to the modal forces. Therefore, the basis function has a quadratic term in s_k to account for flow accelerations. The basis function used is

$$Q(s_k) = Q_0 + Q_1 s_k + Q_2 s_k^2 + \sum_{j=1}^l Q_{j+2} \frac{s_k}{s_k + p_j} \quad (3.39)$$

Since we obtain a fitted continuous model for the GAMs using both the approaches, $Q(s_k)$ computed from Eq. (3.36) and Eq. (3.39) must be very close. Indeed, it has been confirmed for the BFF vehicle that the model is obtained from either of the two approaches is very similar, accounting for minor differences due to fitting errors. The second approach of course, has the advantage of fitting a much smaller size of matrices to a continuous rational function. However, a disadvantage of this method is that the fitted GAM is not as readily separable into its steady and unsteady constituents as was the case earlier. This can be seen by comparing Eq. (3.36) and (3.39). We find that

$$Q_0 = \Phi^T T_{as}^T S [A_0 D_1] T_{as} \Phi \quad (3.40a)$$

$$Q_1 = \Phi^T T_{as}^T S [A_0 D_2 + A_1 D_1 + \sum_{j=1}^l A_{j+1} D_2] T_{as} \Phi \quad (3.40b)$$

$$Q_2 = \Phi^T T_{as}^T S [A_1 D_2] T_{as} \Phi \quad (3.40c)$$

$$Q_{j+2} = \Phi^T T_{as}^T S [A_{j+1} (D_1 - D_2 p_j)] T_{as} \Phi \quad (3.40d)$$

As seen in Eq. (3.40), the matrix Q_1 obtained in Eq. (3.39) represents the combined effects of the steady and unsteady aerodynamics velocity terms. Specifically, the steady aerodynamic velocity term is represented by $A_0 D_2$ and the unsteady effects are due to $A_1 D_1$. Since, they appear in Q_1 in a lumped up form, it is not as straight forward to access the steady part of aerodynamics in Q_1 . However, if required, one can work around this problem by making use of Eq. (3.40) to determine how the steady and unsteady terms are added up. By accounting for the added unsteady

terms, the steady part of Q_1 can then be manipulated as desired.

In conclusion, this section covers the post-processing techniques which are used to obtain a continuous, unsteady aerodynamic model in frequency domain using the DLM. The next section discusses the implementation of the DLM for the BFF vehicle and the results obtained.

3.4 Unsteady Aerodynamics Model for the BFF Vehicle

The aerodynamic model for the BFF vehicle has been developed using the DLM as described in this chapter. An open source, generally applicable, MATLAB based DLM code was developed for this purpose. The code is capable of handling thin lifting surfaces in all three dimensions. The steady solution of the DLM was corrected using a solution from the VLM, also developed as a part of the DLM software. In this section, implementation and validation of the code is briefly discussed, followed by the description of the resulting aerodynamic model for the BFF vehicle. As mentioned earlier, the software package is open source and can be downloaded from the website of the Aeroservoelasticity Research Group at University of Minnesota www.aem.umn.edu/~AeroServoElastic/.

3.4.1 Implementation and Validation

MATLAB based software tools have been developed to carry out the unsteady aerodynamics modeling procedure discussed in the preceding sections. Although currently the main application is the BFF aircraft, the tools have been developed keeping general applications in mind. All the functionalities are completely modular, enabling their use individually or together as required. The important functionalities of the software are

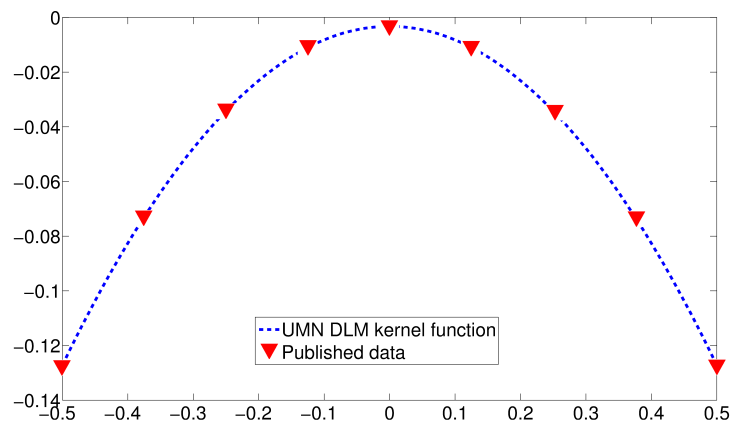
DLM code: Core implementation of the DLM method described in literature. It requires as inputs the aerodynamic grid, reduced frequency and Mach number. It computes the AIC matrix as the output.

VLM code: Implementation of the VLM method. Although the function is used within the DLM code, it is modular so that it can be used independently for steady aerodynamic modeling.

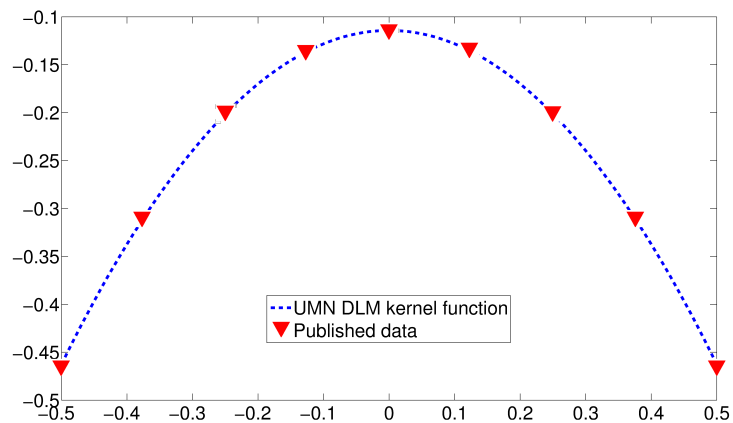
GAM generation: Contains the codes for constructing spline grid from a given structural grid, compute the transformation matrix T_{as} and GAM. Also, contains a code for implementing a least squares based RFA.

BFF model example: Contains the setup file, gridding functions for aerodynamic panel generation and aircraft parameters for the BFF aircraft.

A basic validation of the software is presented here by comparing data generated for a test case to the published data. A test case is taken from a report by Rodden et al [67] which considers the simple grid layout of 5×5 panels. The aspect ratio of each panel is 5 while the flow parameters Mach number and reduced frequency are 0.8 and 2 respectively. The doublet strength distribution is computed for the doublet line of the middle panel of the grid. The results from the paper [67] are superimposed on the results obtained from the software in Fig. 3.5, which verify the DLM implementation.



(a) real part



(b) Imaginary part

Figure 3.5: Kernel function distribution on a panel of AR= 5 at $k = 2$ and Mach 0.8

The VLM code used for steady solution of the aerodynamic model is also validated using an open source, widely used VLM software called XFLR-5 [68] via comparison of the conventional stability derivatives obtained from both.

3.4.2 Aerodynamic Model for BFF Vehicle

Fig. 3.6 shows the aerodynamic grid developed for the BFF aircraft, which consists of 1168 panels. The number of panels is governed by the complexity of the aircraft geometry, as well as certain requirements that need to be fulfilled for acceptable accuracy of the DLM. Specifically, Rodden et al provide a few thumb rules in [67] related to panel sizing.

1. The aspect ratios of individual panels must not be greater than 3.
2. There is a lower limit on the number of panels in the chordwise direction governed by the highest reduced frequency considered for analysis. The thumb rule for calculating the number of panels is 8 to 12 per wavelength of the flow. The wavelength λ can be calculated from reduced frequency k and reference chord \bar{c} using Eq. (3.41)

$$\lambda = \frac{\pi \bar{c}}{k} \quad (3.41)$$

Increasing the number of chordwise panels satisfies this thumb rule, but it also results in increase in panel aspect ratio for a given strip width, thus going against the first rule. Hence, the panels must be optimally constructed to satisfy these thumb rules while remaining as low in number as possible.

The DLM assumes each panel moves individually as discussed in Section 3.2. As a result, the aerodynamic model has thousands of DoFs. It has to be kept in mind that these numbers are reduced to the order of 10's as the aerodynamic model is transformed into modal coordinates by constructing GAMs as discussed further.

The structural grid for the aircraft is shown in the previous chapter in Fig. 2.2, reproduced here along with the spline grid constructed based on it. The spline grid, as explained earlier, is an intermediate step in the computation of transformation matrices for interpolating between the grids shown in Fig. 3.6 and Fig. 3.7.

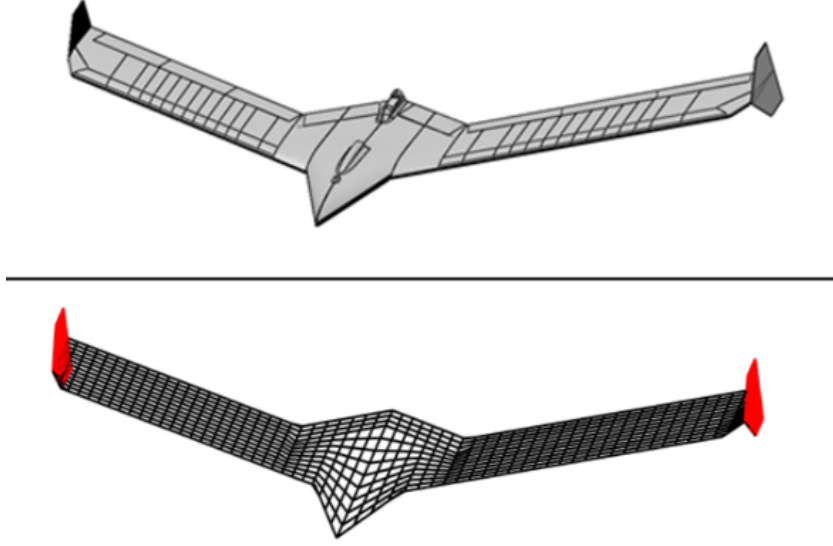
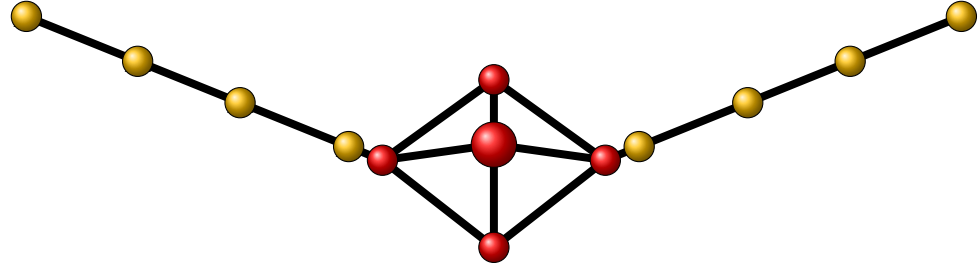


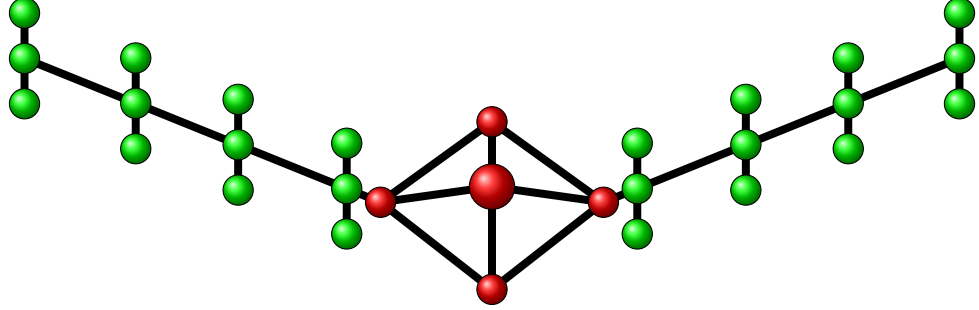
Figure 3.6: CAD model of BFF aircraft and the corresponding aerodynamic grid

Fig. 3.7(b) shows the spline grid as constructed only for the wing sections of the aircraft. The spline grid for center body is also constructed similarly, but is not shown only for the maintaining clarity in the diagram. It should be noted that the structural grid has 14 nodes with 3 DoF each, similar to the nodes in Fig. 3.2. This gives the total number of DoF for the structural grid to be 42. On the other hand, the aerodynamic grid has 1168 panels and each of them have 2 DoF. Therefore, the transformation matrix T_{as} interpolates between the 42 DoF of the structural grid and 2336 DoF of the aerodynamic panels. Also, it can be seen that carrying out the RFA fitting for the GAM matrices is computationally less expensive compared to doing it for the actual AIC matrices, since the GAM matrices are of the same order as the low order structural model. Once the T_{as} matrix is computed, the GAM matrices are computed using Eq. (3.31).

For carrying out the RFA, we calculate the *AIC* matrices at 8 different reduced frequencies ranging from 0 to 3. This range is chosen keeping in mind that according to Lockheed Martin flight test results [16], the body freedom flutter occurs at a reduced frequency of about 0.23. The chosen range therefore ensures that all the necessary dynamics are captured by the model. The GAM matrices are then calculated for these 8 frequencies and a least squares fitting is carried out to give the final aerodynamics model in a MIMO transfer function form as seen in Eq. (3.39). As mentioned earlier, the Roger's method is used for the RFA, which requires the poles for lag states to be specified a priori. A second order lag is chosen for the BFF aircraft and the poles



(a) Structural grid



(b) Spline grid

Figure 3.7: Spline grid construction of the BFF aircraft

are fixed to 0.11 and 0.22. There is no specific procedure behind choosing the poles, except for iterating and checking the fits for different values. Starting values for the iteration may be based on a knowledgeable estimate based on discrete plots of gain values across the set of 8 reduced frequencies selected. It should be remembered that the fitting is done for the dimensionless reduced frequency domain represented by s_k . Therefore the poles in actual frequency domain will vary with airspeed as

$$p_j^* = \frac{2Vp_j}{\bar{c}} \quad (3.42)$$

where p_j^* is the j^{th} lag pole in the actual frequency domain. Fig. 3.8 shows the frequency responses of the aerodynamics transfer functions from the first symmetric bending mode (η_1) and from elevator to lift force at 25 m/s airspeed. They also show the raw GAM matrix data from which these transfer functions have been fitted using the RFA function of the software.

The plots in Fig. 3.8 show lag behavior starting from approximately 10 rad/s, which at higher frequencies is dominated by the acceleration term in Eq. (3.39). This agrees with the fact that at the given velocity of 25 m/s, the poles of the second order lag are 13.5 and 27 rad/s. Fig. 3.9 shows the same transfer functions across a range of

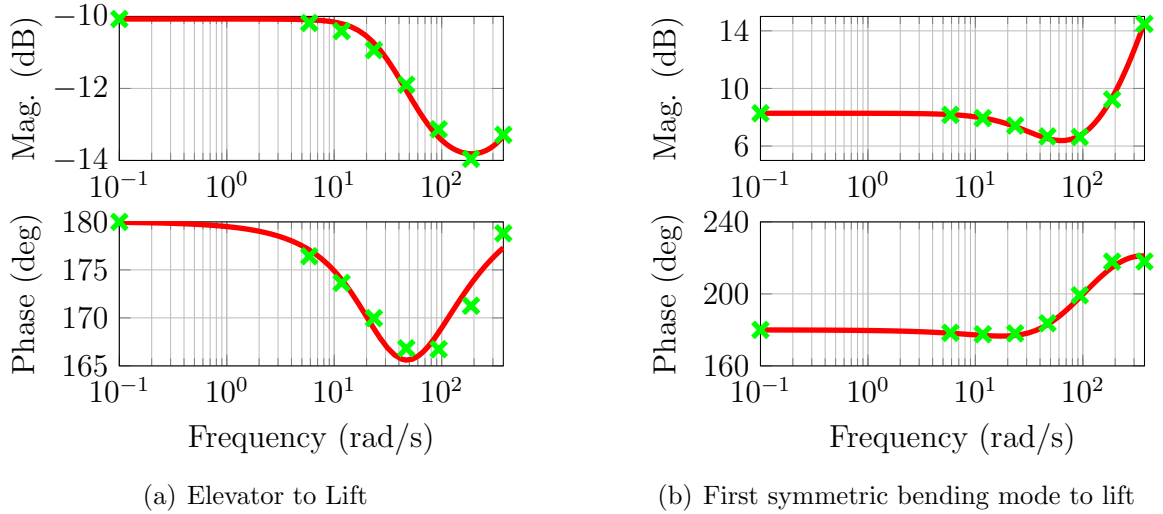
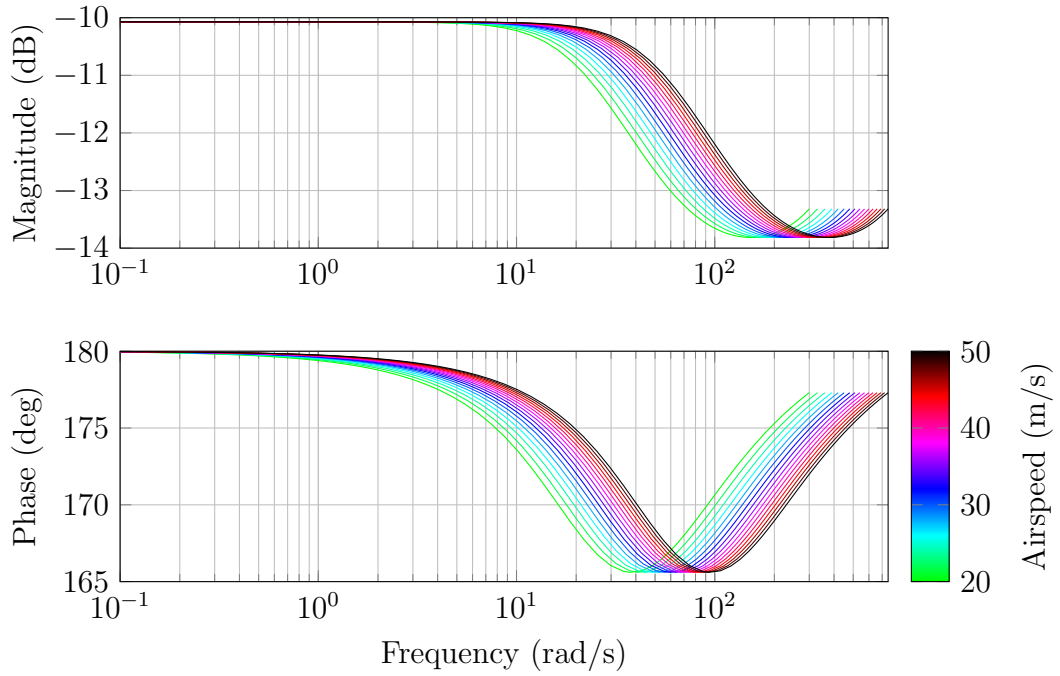


Figure 3.8: Unsteady aerodynamics transfer function fitting for the BFF aircraft, RFA model: —, Raw GAM data: x

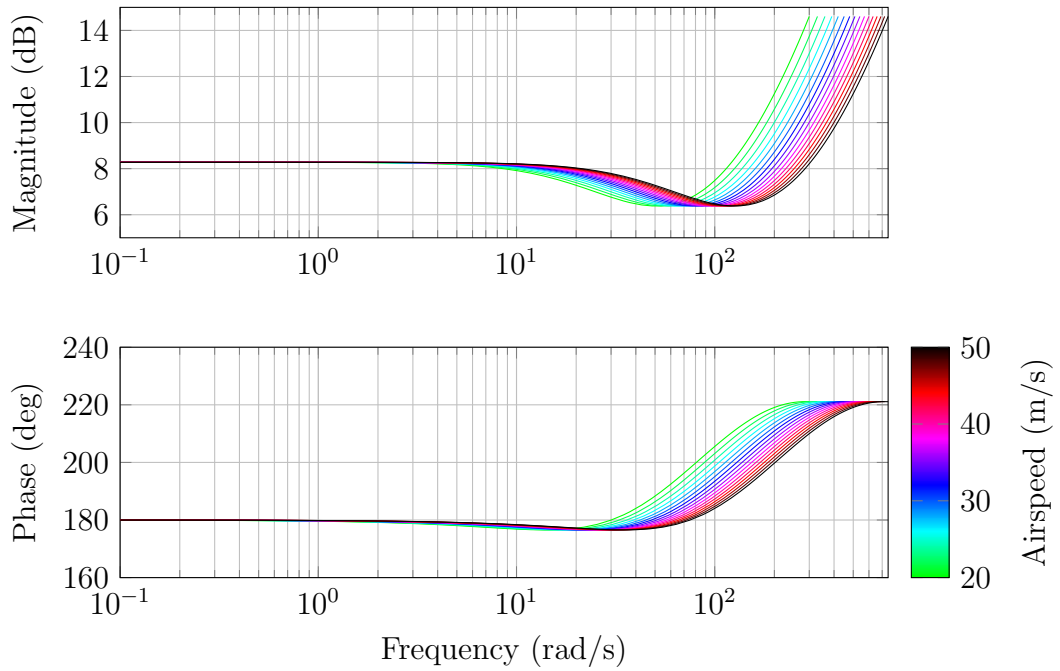
velocities between 20 and 50 m/s.

It can be seen that the onset of unsteady effects is delayed with increase in velocity. This is in agreement with the fact that the aerodynamic lag poles in the actual frequency domain increase in magnitude with increase in velocity. Also, the linear parameter varying nature of the aerodynamics becomes apparent beyond 10 rad/s, since the aerodynamics can be seen to visibly change with airspeed. The change in airspeed depicted in Fig. 3.9 is considered as quasi-static i.e. transient effects due to airspeed change are not modeled.

The aerodynamic model developed for the BFF aircraft in this section forms the third main component of the overall aeroelastic model together with the rigid body and structural dynamics models. Modal transformation using suitable transformation matrices enables a smooth integration of aerodynamics into the linear equations shown in Eqs. (3.1). This complete model forms the basis for building uncertain aeroelastic models and carrying out flutter analysis. The next chapter discusses the construction of uncertain models by considering parametric as well as systemic uncertainties in all the three parts of the model - rigid body dynamics, structural dynamics and aerodynamics.



(a) Elevator to Lift



(b) First symmetric bending mode to lift

Figure 3.9: Aerodynamics transfer functions for the BFF aircraft from 20 to 50 m/s

3.5 Summary

In this chapter, an unsteady aerodynamics model is developed for the BFF vehicle based on the doublet lattice method (DLM). The DLM is a potential flow based panel

method that models unsteady flow around a lifting surface in frequency domain. The main challenge to be addressed in the implementation of the DLM is the compatibility of the resulting aerodynamic model with the mean axes based equations of motion. Specifically, since structural dynamics are represented in modal coordinates, it is important to compute aerodynamic forces in the same coordinate frame.

To solve this problem, a transformation function based on thin plate spline theory is constructed, which effectively transforms the structural degrees of freedom into motion of the aerodynamic panels which can then be used to compute the forces, and it transforms back the resulting force distribution on the aerodynamic grid into the force and moment distribution on the structural grid. The DLM also provides solutions at discrete oscillating frequencies at a given airspeed. To obtain a continuous model in Laplace domain, a rational function fitting is carried out over a range of reduced frequencies (oscillating frequency normalized by reference length and airspeed). The rational function, the structure of which is fixed a priori, is called the Roger's function. The fitting is done in a least squares manner and provides an unsteady aerodynamics model in continuous Laplace domain, which can be easily integrated within the mean axes framework.

Chapter 4

Uncertainty Modeling

4.1 Introduction

Uncertainty modeling is an essential part of robustness analysis of a given system. Most engineering problems have to deal with either unquantified, inaccurate or approximate model dynamics or parametric values which lead to incorrect system response. Therefore, the effects of such inaccuracies or approximations on system response need to be rigorously analyzed. Uncertainty modeling involves systematically identifying and quantifying the uncertainty in various aspects of the model as well as the modeling approach itself. The final objective is to build an uncertain model, or more specifically, a family of models which together represent all possible system responses due to model uncertainties.

The previous two chapters outline the aeroelastic model for the BFF vehicle comprising of rigid body dynamics, structural dynamics and unsteady aerodynamics of the aircraft. In this chapter, the model is used as a basis for incorporating uncertainty with robustness analysis in mind. Hence this chapter lays the foundation for the robust stability and sensitivity analyses discussed in the following chapters. As discussed in the Introduction, the overall model is obtained by modeling each subsystem such as structural dynamics or aerodynamics individually and then integrating them under a common coordinate system. The uncertain model can also be constructed by examining each subsystem individually and accounting for modeling errors and approximations at the subsystem level. This approach is advantageous since it helps determine the required accuracy to model each subsystem for obtaining overall sta-

bility and performance predictions within acceptable limits of error.

Uncertainty in a system can be modeled in many different ways. A broad classification of ways to model uncertainty is given by Pettit [69] who classifies them into two approaches - probabilistic and nonprobabilistic. The probabilistic modeling approach (also referred to as stochastic modeling) is a popular method in the field of uncertainty modeling and reliability analysis [69–72]. Therefore there is considerable amount of research into extending its applications to aeroelastic problems as well [73–75]. Stochastic methods typically categorize uncertainties into parametric (or aleatory) uncertainty and nonparametric (or epistemic, model form) uncertainty [70]. The former deals with uncertainty in specific model parameters while the latter deals with uncertainty due to simplified and therefore approximate modeling of the physics of the problem. The most basic analysis techniques involve specification of probability density functions (PDFs) for random variables associated with uncertain parameters and then running Monte Carlo simulations to obtain the probability distributions of desired model outputs. Challenges in this approach include specifying PDFs in a justifiable manner, often accounting for correlation within parameters, and increasing the sophistication of Monte Carlo sampling to reduce computational effort [73, 75]. An essential and often limiting requirement for these methods is the need for a large amount of stochastic data to specify the PDFs for uncertainties in the model. This is the primary disadvantage of using these methods even for simple models.

Nonprobabilistic methods avoid the requirement of stochastic data [69, 76, 77]. Nonprobabilistic methods typically work with bounds or intervals within which an uncertain model can vary. Several methods have been developed in the field of structural reliability and uncertainty modeling such as the interval methods [77, 78] and convex modeling [76, 79]. However, most of these methods are developed for static and linear structural systems and are difficult to adapt to an aeroelasticity problem. One of the most widely used uncertainty description methods has been developed in the robust control community within the framework of the structured singular value (μ) analysis [17, 18, 80]. Robust control theory essentially separates the uncertain parts of a given linear model from its known ones and combines them in a closed feedback loop. Bounds on the uncertainties can then be computed for which the closed loop system remains stable. In addition, the effect of uncertainties on performance can be assessed. Robust control theory also identifies parametric and nonparametric uncertainties distinctly and these are analyzed within a common framework.

Since the problem of aeroservoelasticity combines multiple subsystems as discussed earlier, the μ framework is suitable for building uncertain models on the account of its flexibility in handling different forms of uncertainty descriptions. It is also more generally applicable for linear systems (with few technical constraints) and requires very little stochastic data for determining uncertainty bounds. Its flexibility is evident from the fact that several researchers have used μ analysis in different ways for the problem of robust stability and performance of aeroservoelastic systems. Borglund et al [19, 81, 82] specify uncertainty in the force distribution across aerodynamic panels as well as material properties of each structural element in the finite element model. Lind and Brenner [20, 21] on the other hand focus on developing online tools based on μ computations to predict onset of flutter in a robust manner. Uncertainties include exact airflow conditions, unmodeled high frequency dynamics and parametric uncertainties in structural and aerodynamics models. Other approaches for uncertainty modeling within μ framework may also be found [83, 84], but will not be reviewed here.

In this chapter, uncertainties in the structural model and aerodynamic model will be defined and modeled separately. The resulting combined uncertain model can essentially be seen as a family of models representing the variation in system dynamics as the uncertain parts vary. This sets up the model for robust stability and performance analysis and also sensitivity studies which follow in later chapters.

4.2 Uncertainty Descriptions

In μ analysis, uncertainties are specified to be a combination of norm bounded uncertain elements Δ and weighting functions W which determine the bounds of uncertainty. The properties of both Δ and W depend on the nature of the uncertainty description. As mentioned earlier, in μ analysis the uncertain elements are separated from the known parts of the model and recombined with them in a feedback loop. This operation is called the linear fractional transformation (LFT). A typical LFT feedback loop is shown in Fig. 4.1.

In Fig. 4.1, G is the known part of the model containing nominal dynamics, data corresponding to interconnection with uncertainties as well as the weighting functions associated with the uncertainties. Δ represents all the norm bounded uncertain elements defined in the model. v and w are the interconnecting channels while d and

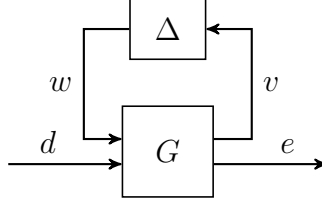


Figure 4.1: LFT feedback loop

e are conventionally considered as input disturbances and output errors respectively. The LFT interconnection has powerful properties which μ analysis takes advantage of, as seen in later chapters.

For the analysis of BFF vehicle, both parametric and nonparametric uncertainties are considered. An uncertainty can be defined in a multiplicative or additive manner, as shown below.

$$X = X_0(1 + W_X\Delta_X) \quad (\text{Multiplicative}) \quad (4.1a)$$

$$X = X_0 + W_X\Delta_X \quad (\text{Additive}) \quad (4.1b)$$

For a parametric uncertainty, X_0 represents the nominal value of the parameter, Δ_X is a norm bounded, real parametric uncertainty and W_X is a scalar weighting function representing bounds on the uncertainty. For instance, suppose X an uncertain real parameter known to be in the interval $[1.4, 2.6]$. In this case, the nominal value is the interval mean $X_0 = 2$. An additive uncertainty model is $X = X_0 + W_X\Delta_X$ with $W_X = 0.6$ as the interval radius and $|\Delta_X| \leq 1$ as the normalized real parameter uncertainty. A multiplicative uncertainty model is $X = X_0(1 + W_X\Delta_X)$ with $W_X = 0.3$ representing 30% uncertainty and $|\Delta_X| \leq 1$ again as the normalized real parameter uncertainty. Depending on the nature of the uncertainty, either multiplicative or additive descriptions may be used.

Nonparametric uncertainties such as uncertain dynamics can also be modeled using descriptions similar to that shown in Eq. (4.1). In such cases, X_0 can represent a nominal, frequency dependent object with known dynamics while Δ_X represents an uncertain element with a known gain bound, e.g. $|\Delta(j\omega)| \leq 1 \forall \omega$. The weight $W_X(j\omega)$ is frequency dependent and the magnitude $|W_X(j\omega)|$ represents either the absolute or relative uncertainty at each frequency for additive or multiplicative models. It should be noted that all these variables need not be single input single output (SISO). Rather, they can be multiple input multiple output (MIMO) as long as the

inner matrix multiplications are possible. Also, it is possible to have frequency dependent weights of different dimensions multiplied on either side of the uncertain element. These descriptions are very useful for modeling unmodeled dynamics at certain frequencies or nonlinear dynamics which a nominal linear model fails to capture. See [17, 80] for further details. The next few sections describe the parametric as well as nonparametric uncertainties for the structural dynamics and aerodynamics models.

4.3 Uncertainties in Structural Dynamics

Uncertainties in the structural dynamics can arise mainly due to deviation of the theoretical model from experimental results as well as measurement errors within experimental data used to construct the model. The theoretical finite element model may be constructed using nominal values of model parameters such as stiffness and mass distribution which are themselves either estimated from known properties of various structural components or experimentally determined. If experimental data is used to determine values of model parameters, the parametric uncertainty due to measurement errors and other systemic errors in the experiments has to be taken into account. On the other hand, experiments such as ground vibration tests are designed to obtain dynamic system responses under external loading. The differences between the dynamic responses obtained from experiments and theoretical model then become the basis for defining nonparametric or model form uncertainty. It is important to determine which uncertainties must be included in the model to avoid making the analysis overly conservative. For example, if the dynamic responses from ground vibration tests are satisfactorily simulated by an uncertain model constructed using only parametric uncertainties, then the nonparametric uncertainties need not be defined.

In this section, we first look at some of the typical ground tests conducted for structural model identification purposes. Next, we explore the different types of uncertainties defined using the data generated from these tests and also examine various methods to handle them efficiently.

4.3.1 Ground Tests for Structural Model Identification

4.3.1.1 Static Deformation Tests

Static ground tests typically involve constrained and controlled elastic deformation of individual parts of the aircraft via static loading. The tests can either be performed on the fully constructed aircraft or more preferably, on the structural components of the aircraft. The primary goal of these tests is to determine the material properties of the structural components by measuring the elastic deformations due to a known static loading. For example, a spar designed for the wing section of an aircraft may be subjected to cantilever loading to determine the bending stiffness properties. If linear deformation is assumed, then the parameter of interest would be the Young's modulus which could be estimated by measuring deflections along the length of the spar for a known loading at the cantilever tip. The expression for deflection δ_c as a function of location along the cantilever is given by

$$\delta_c(x) = \frac{Px^2}{6EI}(3L - x) \quad (4.2)$$

where P is the force applied at the tip, L is total length of the cantilever, I is the second moment of inertia of spar cross-section and x is the variable location measured from clamped end. Using Eq. (4.2) and experimental data obtained as described above, the Young's modulus E may be obtained.

As discussed earlier, an important source of uncertainty is measurement errors while conducting these tests. However, there are other sources to keep in mind as well. Since the structural elements in the finite element model constructed is not often a direct representation of the actual structural components in the aircraft, there are several approximations involved in associating the material properties determined in these tests to the structural elements of the model. Even though it may not be always possible to quantify these approximations, they must be kept in mind while constructing the model. Uncertainties based on these tests are primarily parametric in nature and are defined accordingly, as described in the previous section.

4.3.1.2 Ground Vibration Tests

A ground vibration test (GVT) helps evaluate the vibrational response of a structure under a given dynamic external forcing [10, 85, 86]. The external forcing (seen as the

excitation signal) can range from an impulse to a frequency sweep. The vibrational response is typically recorded using sensors such as accelerometers and strain gauges located across the structure. These experiments are more representative of the actual system dynamics since

1. The complete structure is tested in these experiments, as opposed to the static tests performed on individual components for obtaining the parametric values discussed in the previous subsection.
2. These tests typically involve dynamic loading, which reveals much more information regarding system response under a range of forcing frequencies.

The fundamental vibrational frequencies of the structure are identified from the frequency response data generated by the GVT. Mode shape construction from modal data has been extensively researched [11,87]. However, the mode shapes are obtained as a function of the locations of sensors which measure displacements or accelerations. Therefore, additional post-processing is required to extract mode shapes which are in the eigenspace of the finite element model. The post-processing can be any tractable interpolation/extrapolation technique which helps reconstruct the mode shapes in the relevant eigenspace. Finally, the difference between experimental and theoretical values of mode shapes and frequencies may be obtained, which provides an uncertainty range for eigenvectors and eigenvalues of the structural model. Since eigenvectors and eigenvalues do not enter the structural model parametrically or in any systemic manner, incorporating the mode shape differences in form of uncertainties becomes a nontrivial exercise. In the next two subsections, uncertainties within mode shapes are given special attention as they form a vital part of constructing the uncertain structural model.

4.3.2 Parametric Uncertainties

Model parameters of a typical finite element model can include material properties of the constituent elements such as bending and torsional stiffnesses (represented by Young's modulus E and shear modulus G), as well as mass distribution across the elements. Eq. (4.1) can be readily used to define the corresponding uncertain parameters. However, a very basic inconvenience comes to surface when constructing the model with such parametric uncertainties. Although real parametric uncertainty

descriptions can be used to build an uncertain structural model, it makes the transformation of that model into its modal form as shown in Eq. (2.39) complicated. Eq. (2.39) shows the modal transformation for a given K and M matrices, rewritten here for convenience.

$$\underbrace{\Phi^T M \Phi}_{M_{mod}} \ddot{\eta} + \underbrace{\Phi^T K \Phi}_{K_{mod}} \eta = \underbrace{\Phi^T F}_{F_{mod}} \quad (4.3)$$

The complication arises from the fact that the transformation matrix for such a transformation is the eigenvector matrix, which itself is a function of these matrices. This can be understood as follows.

Let $p := \{p_1, p_2, \dots, p_n\}$ be the set of model parameters within the finite element model described by mass and stiffness matrices $M(p)$ and $K(p)$. Let the uncertainties corresponding to the parameter set p be defined as $\Delta_p := \{\Delta_{p_1}, \Delta_{p_2}, \dots, \Delta_{p_n}\}$. We can assume that Δ_p is defined as a set of additive uncertainties. Also, let the set of weights associated with the uncertainties be defined as $W_p := W_{p_1}, W_{p_2}, \dots, W_{p_n}$. Therefore, the i^{th} uncertain parameter may be written as

$$\tilde{p}_i = p_i + W_{p_i} \Delta_{p_i} \quad (4.4)$$

The uncertain structural dynamics can now be described mathematically in terms of the set of uncertain parameters \tilde{p} as

$$M(\tilde{p})\ddot{x} + K(\tilde{p})x = F_{\text{ext}} \quad (4.5)$$

To express the model in its modal form, we compute the eigenvectors from the eigenvalue problem

$$[K(\tilde{p}) - \lambda_k M(\tilde{p})] \phi_k = 0 \quad (4.6)$$

We see that eigenvectors are a function of the stiffness and mass matrices and consequently are indirectly dependent on the parametric uncertainties. Computation of eigenvectors in Eq. (4.6) while accounting for uncertainties is difficult. Hence, carrying out modal transformation using eigenvectors for the uncertain model is not a straight forward process. We look at two ways to handle this problem, as discussed ahead.

4.3.2.1 Approximation using Dynamic Uncertainty bounds

This is a simple, ad-hoc approach to the problem, where a given parameter is perturbed from its nominal value to the maximum and minimum possible value within its prescribed uncertainty range. At these extreme parametric values, the overall modal structural model (or perhaps aeroelastic model) is constructed, which is then used to define upper and lower bounds for a dynamic uncertainty for the model. In other words, the parametric uncertainty is modeled equivalently as a model form or nonparametric uncertainty. As an example, consider the parameter C.G. location, which does not directly enter the mass matrix of the system. By constructing 2 different mass matrices reflecting the extreme C.G. locations corresponding to $\pm 5\%$ of the mean aerodynamic chord, the overall aeroelastic models are constructed. These models are used to upper and lower bound a dynamic uncertainty using appropriate frequency weighting. The bounds may be visualized as shown in Fig. 4.2, which shows the variation in transfer function from elevator to first flexible mode (first wing bending) of the aircraft due to uncertainty in C.G. location. In Fig. 4.2, the enve-

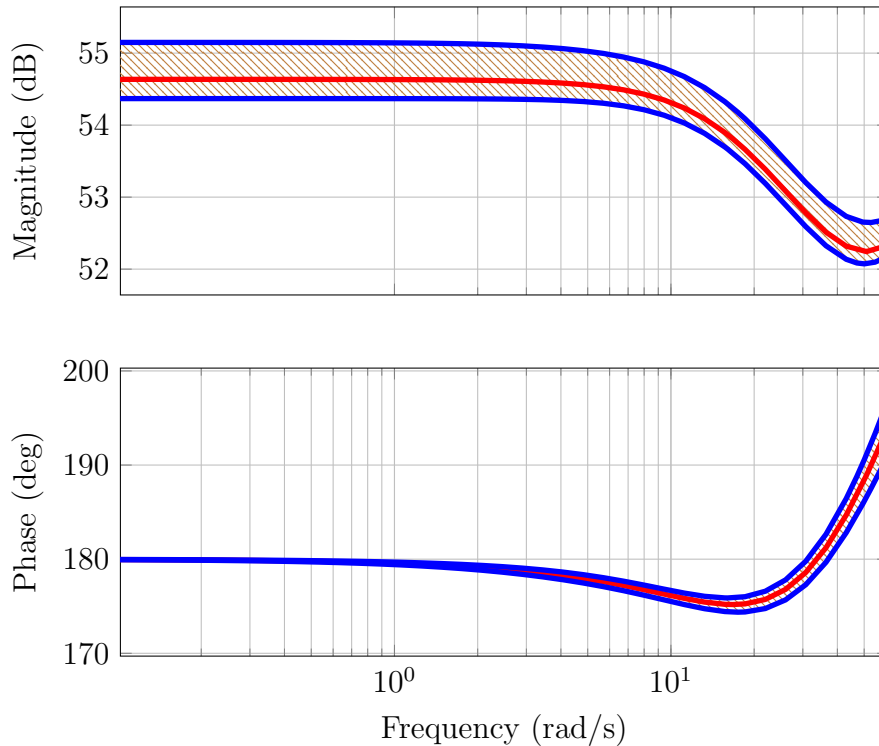


Figure 4.2: Upper and Lower bound models obtained via C.G. perturbation. Nominal model indicated by —, Bounds indicated by —

lope surrounding the nominal model frequency response represents the scope of the uncertain model. As mentioned earlier, the uncertain model is essentially a family of models, and the shaded envelope represents the region where all possible models within the uncertain model lie.

A similar exercise can be carried out for any parameter which is a part of the mass or stiffness matrices. The main problem with this approach is that it accounts for multiple uncertain parameters in an ad-hoc manner. Theoretically, the bounds for an uncertain model comprising of n parametric uncertainties Δp could possibly be constructed by considering all the 2^n combinations of the upper and lower bound values of each of the parameters and constructing models using all of them. A dynamic uncertainty can then be chosen which covers all the models generated by considering those combinations. However, the assumption that all the models covered under such an uncertain model are stable is a non-trivial one. Specifically, even if a model built at any of those extreme parametric values are stable, it does not guarantee stability of a model built from a random combination of parametric values which lie within the bounds. The method is not rigorous enough in that sense and is therefore is deemed ad-hoc. Hence, a more rigorous approach involving derivatives of eigenvectors with respect to model parameters has been developed, as described next.

4.3.2.2 Eigenvector Derivatives Method

A more rigorous approach for incorporating parametric uncertainties is proposed which accounts for the uncertainties up to the first order of accuracy. To achieve the objective of constructing uncertain modal mass and stiffness matrices from a given set of uncertain model parameters, we use the concept of perturbations. The approach involves deriving closed form expressions for perturbed modal mass and stiffness matrices as linear functions of perturbations of its constituent parameters. The coefficient of a given perturbation in those expressions can then be used to compute the effect of uncertainty in that parameter on the modal matrices. This idea is further explained in detail ahead.

Let $p := \{p_1, p_2, \dots, p_n\}$ be the set of model parameters, Δ_p be the corresponding additive parametric uncertainties W_p be the set of parametric weights as defined earlier. Additionally, we also define a set of parametric perturbations $\delta p := \{\delta p_1, \delta p_2, \dots, \delta p_n\}$. It should be remembered that δp_i denotes perturbation of the i^{th} parameter p_i and Δ_{p_i}

denotes the corresponding uncertainty. While an uncertainty represents the possible range of variation in p_i owing to modeling errors, a perturbation is an exact, measurable deviation from the nominal value. Finally, it should be noted that this derivation assumes additive uncertainty for all parameters and modal matrices, although the derivation and the results can be easily modified to accommodate multiplicative uncertainties as well.

We need to compute perturbations in the modal mass (δM_{mod}) and stiffness (δK_{mod}) matrices as a function of parametric perturbations up to first order approximation in the following form -

$$\delta M_{\text{mod}} = \sum_{j=1}^n \frac{\partial M_{\text{mod}}}{\partial p_j} \delta p_j \quad (4.7a)$$

$$\delta K_{\text{mod}} = \sum_{j=1}^n \frac{\partial K_{\text{mod}}}{\partial p_j} \delta p_j \quad (4.7b)$$

As mentioned earlier, coefficients of i^{th} perturbation δp_i in Eqs. (4.7) can be used to obtain an uncertain modal mass and stiffness matrix as a function of uncertainty in the i^{th} parameter p_i . If the required coefficients $\frac{\partial M_{\text{mod}}}{\partial p_i}$ and $\frac{\partial K_{\text{mod}}}{\partial p_i}$ are available, the uncertain modal matrices can be written as

$$\Delta_{M_{\text{mod}}}(\Delta_{p_i}) = \frac{\partial M_{\text{mod}}}{\partial p_i} W_{p_i} \Delta_{p_i} \quad (4.8a)$$

$$\Delta_{K_{\text{mod}}}(\Delta_{p_i}) = \frac{\partial K_{\text{mod}}}{\partial p_i} W_{p_i} \Delta_{p_i} \quad (4.8b)$$

where $\Delta_{M_{\text{mod}}}$ and $\Delta_{K_{\text{mod}}}$ represent additive uncertainty in the mass and stiffness modal matrices. We can consider Eq. (4.8) to hold as true since within limits of linearity, any perturbation δp_i can be accounted for in the mass and stiffness matrices using these coefficients, as seen in Eqs. (4.7). Therefore, for any value of parameter p_i obtained by deviating from the nominal value within the uncertainty bound $W_{p_i} \Delta_{p_i}$, effect of that deviation on the modal matrices will be represented suitably as well. Eqs. (4.8) essentially formalize this by directly relating uncertainty in p_i to the resulting uncertainty in the modal matrices.

Furthermore, all the uncertain parameters represented by Δ_p can be considered together via summation of their contribution towards the overall uncertain mass and

stiffness matrices as

$$\Delta_{M_{\text{mod}}} = \sum_{j=1}^n \frac{\partial M_{\text{mod}}}{\partial p_j} W_{p_j} \Delta_{p_j} \quad (4.9a)$$

$$\Delta_{K_{\text{mod}}} = \sum_{j=1}^n \frac{\partial K_{\text{mod}}}{\partial p_j} W_{p_j} \Delta_{p_j} \quad (4.9b)$$

$$(4.9c)$$

As we can see from Eqs. (4.9), computing the coefficients $\frac{\partial M_{\text{mod}}}{\partial p_j}$ and $\frac{\partial K_{\text{mod}}}{\partial p_j}$ for all parameters is key to obtaining modal matrix uncertainties as a function of parametric uncertainties. The coefficients for p_i can be computed by differentiating the expressions of modal mass and stiffness matrices in Eqs. (4.3) with respect to p_i . We obtain

$$\frac{\partial M_{\text{mod}}}{\partial p_i} = \Phi^T \frac{\partial M}{\partial p_i} \Phi + 2\Phi^T M \frac{\partial \Phi}{\partial p_i} \quad (4.10a)$$

$$\frac{\partial K_{\text{mod}}}{\partial p_i} = \Phi^T \frac{\partial K}{\partial p_i} \Phi + 2\Phi^T K \frac{\partial \Phi}{\partial p_i} \quad (4.10b)$$

The derivatives of the actual mass and stiffness matrices with respect to the modeling parameters, $\frac{\partial M}{\partial p_j}$ and $\frac{\partial K}{\partial p_j}$, can be computed analytically for any typical finite element model. The eigenvector derivatives $\frac{\partial \Phi}{\partial p_j}$ on the other hand are not computable in an obvious manner. There are several approaches to compute them in an efficient manner [88–90]. However, most of the methods use the Nelson’s method [88] as the base to build upon their approaches which typically seek to bring down computational costs for large systems. Since we deal with low order systems in this thesis, the original method is sufficiently fast. The derivation for Nelson’s method is reproduced in Appendix A.2. The final result can be summarized as shown ahead. For i^{th} parameter p_i , we have $\frac{\partial \Phi}{\partial p_i} = \left[\frac{\partial \phi_1}{\partial p_i} \frac{\partial \phi_2}{\partial p_i} \dots \frac{\partial \phi_m}{\partial p_i} \right]$. Now, the derivative of the k^{th} eigenvector with respect to p_i may be obtained as

$$\frac{\partial \phi_k}{\partial p_i} = \sum_{s=1}^{s=n} \beta_{ks} \phi_s \quad (4.11a)$$

$$\beta_{ks} = \frac{1}{\lambda_k - \lambda_s} \phi_s^T \left[\frac{\partial K}{\partial p_i} - \lambda_k \frac{\partial M}{\partial p_i} \right] \phi_k \quad \forall k \neq s \quad (4.11b)$$

$$\beta_{kk} = -\frac{1}{2} \phi_k^T \frac{\partial M}{\partial p_i} \phi_k \quad k = s \quad (4.11c)$$

Eqs. (4.11) along with Eqs. (4.10) can be used to compute the required coefficients in Eqs. (4.9). Thus, Eqs. (4.9) then provide us with modal mass and stiffness uncertainties ($\Delta_{M_{\text{mod}}}$ and $\Delta_{K_{\text{mod}}}$) as a linear function of parametric uncertainties Δ_{p_i} .

However, it is important to be aware of the limitations of this approach owing to linearity assumptions in Eqs. (4.9), (4.10). More precisely, the eigenvector derivatives in Eq. (4.10), obtained via the Nelson method, are themselves a nonlinear function of the eigenvectors. Hence, the linear relation between parameter perturbations (Δ_{p_i}) and corresponding modal matrix uncertainties ($\Delta_{M_{\text{mod}}}, \Delta_{K_{\text{mod}}}$) holds true (within acceptable tolerance) only for small values. By computing actual perturbed mass and stiffness matrices for a parameter which is perturbed by a known amount, the results can be compared to the linear function assumed in Eqs. (4.7). This comparison serves as a useful indication of whether the modal matrix uncertainties computed using Eqs. (4.9) are accurate within reasonable tolerance limits.

Uncertain modal matrices can be computed by adding the uncertainties computed in Eqs. 4.9. The total uncertain matrices are

$$\tilde{M}_{\text{mod}} = M_{\text{mod}} + \Delta_{M_{\text{mod}}} \quad (4.12a)$$

$$\tilde{K}_{\text{mod}} = K_{\text{mod}} + \Delta_{K_{\text{mod}}} \quad (4.12b)$$

Of course, it should be kept in mind that the uncertainty range for the parameters must fall within the limits prescribed for linearity to hold in the perturbation equations. The uncertain modal matrices \tilde{M}_{mod} and \tilde{K}_{mod} can now be used to construct the uncertain structural model and subsequently, the uncertain aeroelastic model. Thus, the eigenvector derivative based approach provides a simple yet mathematically rigorous approach for incorporating multiple parametric uncertainties into the structural model. This approach can also be modified to incorporate uncertainties in mode shapes themselves, which may be defined on the basis of data from ground vibration tests. This is discussed in the following subsection.

4.3.3 Mode Shape Uncertainties

Parametric uncertainties represent the inaccuracies in experimental values of model parameters. But we also have experiments like ground vibration tests which are designed to directly measure the fundamental frequencies of vibration and their associated mode shapes of the complete structure. These quantities are theoretically

obtained from eigenvalues of the linear finite element model and their corresponding eigenvectors. The finite element model itself may be constructed using the nominal parametric values estimated from static ground tests as discussed in earlier. It now becomes desirable to have a way to account for the deviation between the experimental and theoretical results via an uncertainty model. In this subsection we discuss a way to incorporate results from a ground vibration test into an uncertain structural dynamics model expressed in modal coordinates.

A good starting point is to go back to the definition of modal mass and stiffness matrices as shown in Eq. (4.3). Let $\Delta_{\Phi} := [\Delta_{\phi_1} \Delta_{\phi_2} \cdots \Delta_{\phi_m}]$ represent a mode shape uncertainty matrix comprising of uncertainties of m eigenvectors. Also, let $W_{\Phi} := \text{diag}(W_{\phi_1}, W_{\phi_2}, \cdots, W_{\phi_m})$ be a diagonal matrix consisting of weights for each eigenvector uncertainty. These weights can be chosen so that the overall uncertainty in a mode shape accounts for discrepancies seen in experimental data. From Eqs. (4.3), the corresponding uncertain modal mass and stiffness matrices can be written as

$$\tilde{M}_{\text{mod}} = [\Phi + \Delta_{\Phi} W_{\Phi}]^T M [\Phi + \Delta_{\Phi} W_{\Phi}] \quad (4.13a)$$

$$\tilde{K}_{\text{mod}} = [\Phi + \Delta_{\Phi} W_{\Phi}]^T K [\Phi + \Delta_{\Phi} W_{\Phi}] \quad (4.13b)$$

Simplifying on the right hand side by ignoring terms which are nonlinear in Δ_{Φ} , we get

$$\tilde{M}_{\text{mod}} = \Phi^T M \Phi + \Delta_{\Phi}^T M \Phi + \Phi^T M \Delta_{\Phi} \quad (4.14a)$$

$$\tilde{K}_{\text{mod}} = \Phi^T K \Phi + \Delta_{\Phi}^T K \Phi + \Phi^T K \Delta_{\Phi} \quad (4.14b)$$

Eqs. (4.14) can form the basis for constructing uncertain modal mass and stiffness matrices for a given set of uncertain mode shapes. However, there are a few drawbacks in this approach. Firstly, modal data from GVT may not be available for all modes considered in the finite element model. Consequently, Δ_{Φ} may only be available for some mode shapes. Also, defining uncertainties based on the available modal data results in Δ_{Φ} in form of a matrix of real parametric uncertainty elements which is computationally more expensive for μ analysis compared to scalar uncertainties. And finally, even though GVT data is incorporated into the uncertain model, mode shape uncertainties themselves do not have any direct physical significance. Therefore, there is little insight gained from studying the effect of uncertainty bounds of mode shapes on the stability and performance of the model.

To incorporate modal data from GVT into an uncertain structural model in a more meaningful manner, we seek to represent mode shape uncertainties via an equivalent set of uncertainties on model parameters such as Young’s modulus or mass distribution. This approach is motivated from the assumption that any discrepancies in experimentally obtained modal data are mainly due to inaccuracies in the assumed nominal values of the model parameters.

As done previously, we can use the concept of perturbations to study the relationship between mode shape uncertainties and an equivalent set of parametric uncertainties. Essentially, we project a given perturbation in mode shapes on to a set of perturbations of model parameters using eigenvector derivatives as the directions for projection. The mode shape perturbation is based on the upper bound value of the corresponding mode shape uncertainty. Thus, the assumed mode shape perturbation represents the maximum possible deviation within the uncertainty bound defined for it. The results, which are in the form of model parametric perturbations, may then be used to compute the uncertainty bounds in model parameters. We can then consider these parametric uncertainties as *equivalent* to the mode shape uncertainties. This approach is explained in detail ahead.

Let Φ represent the mode shapes as defined earlier and $\delta\Phi := [\delta\phi_1\delta\phi_2\cdots\delta\phi_m]$ represent the corresponding perturbation. Also, let $p := \{p_1, p_2, \dots, p_n\}$ represent the set of model parameters and the corresponding perturbations be δp as defined in the previous subsection. Then for k^{th} mode shape we have

$$\delta\phi_k = \sum_{j=1}^n \frac{\partial\phi_k}{\partial p_j} \delta p_j \quad (4.15)$$

In Eq. (4.15), the eigenvector derivatives can be computed via the Nelson’s method as discussed in the previous subsection. $\delta\phi_i$ is assumed to be a known perturbation - equal to the upper bound value of the corresponding uncertainty $W_{p_k}\Delta_{p_k}$. The objective is to find the set δp which satisfy the Eq. (4.15). Once we have an equivalent set of parametric perturbations, they can be used as the uncertainty bounds on those parameters and incorporated into the structural model as described in the previous subsection. The parametric uncertainties obtained in this manner are considered equivalent to the mode shape uncertainties from GVT data.

Obtaining the parametric perturbation set δp is essentially an optimization problem

since Eq. (4.15) is usually overdetermined in nature. To understand the problem better, Eq. (4.15) can be rewritten as

$$\delta\phi_k = \underbrace{\begin{bmatrix} \frac{\partial\phi_k}{\partial p_1} & \frac{\partial\phi_k}{\partial p_2} & \dots & \frac{\partial\phi_k}{\partial p_n} \end{bmatrix}}_{\nabla\phi_k} \delta p \quad (4.16)$$

Since the number of model parameters is usually small compared to the length of a mode shape vector, $\nabla\Phi_i$ is usually a tall and skinny matrix. Such problems are typically solved via least squares fitting which minimizes the square of the fitting errors [91], and can be expressed compactly as

$$\delta p^* = \arg \min_{\delta p} \|\delta\phi_k - \nabla\phi_k \delta p\|_2^2 \quad (4.17)$$

where δp^* is the least squares optimal solution to the problem. However, it must be kept in mind that there are additional constraints on δp which need to be satisfied in addition to Eq (4.17). As discussed in the previous subsection, the linearity assumption made in Eq. (4.15) is valid only for small perturbations in the parameters p . Therefore, it is necessary to have additional penalty on the magnitude of the parametric perturbations. Also, it is desirable to keep the number of parametric uncertainties to the minimum, which means sparse solutions are preferable.

A common approach involves solving the so called least squares regulation optimization problem. Regulation essentially adds additional penalty to the objective function for optimizing ill-posed problems. For the problem at hand, since it is desirable to reduce the magnitude of the parametric perturbations Δp and also promote sparse solutions, a regulation term based on the L_1 norm of Δp can be added to the problem. Equation (4.17) is therefore modified as

$$\begin{aligned} \delta p^* &= \arg \min_{\delta p} \|\delta\phi_k - \nabla\phi_k \delta p\|_2^2 + \lambda \|\delta p\|_1 \\ &\text{subject to } \|\delta p\| \leq \delta p_{max} \end{aligned} \quad (4.18)$$

There are several open source solvers available to solve the optimization problem described in Eq. (4.18). The problem may be posed as a basis pursuit denoising problem [92,93] or a least absolute shrinkage and selection operator (LASSO) problem [94]. It should be noted that the basis pursuit solvers typically work better for sparsity promoting cases.

Although there are mathematically rigorous approaches based on least squares regularization are available as discussed, a simpler, more ad-hoc approach is suggested for acceptable solutions. This approach involves solving the least squares problem as described in Eq. (4.17) iteratively. After each iteration, it is checked if the resulting optimal Δp^* contains perturbations which are too large to justify the linearity assumptions in Eq. (4.15). Parameters with large perturbations are left out of the parameter set of the next iteration. The iterations stop when all the parameters within the set are ‘small’. The approach is summarized below.

1. Determine upper bounds on all parametric perturbations within which they are considered to satisfy the linear relation in Eq. (4.15).
2. Compute the simple least squares solution shown in Eq. (4.17) for the set of parametric perturbations Δp .
3. Identify the parameters where perturbation magnitudes exceed the upper bounds determined in step 1. If all parameters fall within the upper bounds, stop iterations.
4. Remove the subset of parameters identified in step 3 from the perturbation set Δp . Repeat from step 2 with the updated set.

This procedure does not guarantee a solution since it is possible that removing parameters which cross the specified upper bounds may result in some of the remaining parameters to do the same in the next iteration. Also, there is no convergence on the fitting errors across the iterations, which means the errors could possibly go worse with each iteration. Therefore the final solution, if obtained, must be plugged into Eq. (4.16) and the resulting mode shape perturbation compared to that obtained from GVT data. Setting limits on acceptable magnitudes of fitting error as well as the upper bounds in the first step above is essentially based on engineering judgment.

4.3.4 Uncertain Structural Model

The previous two subsections deal with the uncertainty descriptions based on experimental data. It can be seen that data from both, static tests and GVT are finally transformed into parametric uncertainties using eigenvector derivatives. Since uncertainty bounds are determined using data from multiple experiments, the final

uncertain structural model is constructed using the worst case bounds for each parameter. For instance, to determine the bounds on uncertainty in Young’s modulus, we compare the bounds based on measurement errors in static tests to the value obtained from mode shape uncertainty projection and choose the higher of the two. Once the complete set of real parametric uncertainties are determined, the uncertain structural model may be constructed as described in Eq. (4.9) and Eq. (4.10).

4.4 Uncertainties in Aerodynamics

Uncertainties in the aerodynamic model arise from model parameters associated with steady aerodynamics such as aerodynamic stability and control derivatives as well as frequency dependent model form uncertainties in the unsteady aerodynamics. As seen in Chapter 3, the aerodynamic model is developed as a rational function in frequency domain analogous to a MIMO transfer function, see Eq. (3.39), reproduced here

$$Q(s_k) = Q_0 + Q_1 s_k + Q_2 s_k^2 + \sum_{j=1}^l Q_{j+2} \frac{s_k}{s_k + p_j} \quad (4.19)$$

As seen in Chapter 3, the aerodynamic model can be separated into steady and unsteady parts if required using Eqs. (3.40). Since we are interested in defining uncertainties for both steady and unsteady aerodynamics, we rewrite the aerodynamics model as

$$Q(s_k) = \underbrace{Q_0 + Q_1^S s_k}_{Q_{steady}} + \underbrace{Q_1^{unS} s_k + Q_2 s_k^2 + \sum_{j=1}^l Q_{j+2} \frac{s_k}{s_k + p_j}}_{Q_{unsteady}} \quad (4.20)$$

where Q_1^S and Q_1^{unS} are the steady and unsteady partitions of the Q_1 matrix in Eq. (4.19). This separation allows for parametric uncertainty descriptions for stability and control derivatives within the steady aerodynamics matrices and dynamic uncertainty descriptions for unsteady aerodynamics. The steady aerodynamics model is developed using a vortex lattice (VLM) code as described in the previous chapter, while the unsteady incremental part comes from the doublet lattice method (DLM). Often, wind tunnel tests are also conducted to update parts of the aerodynamic model. The next few subsections cover the process of defining parametric and nonparametric uncertainties for an aerodynamic model.

4.4.1 Experiments for Aerodynamic Model

The most widely conducted ground based experiment conducted to identify an aerodynamic model is wind tunnel testing [95, 96]. A basic wind tunnel test capable of measuring forces and moments about all three axes can provide all the steady aerodynamics stability derivatives. Like any other experimental procedure, there are significant measurement errors which must be taken into account.

The extent up to which an aerodynamic model is identifiable using wind tunnel data essentially depends on the capabilities of the experimental setup. Most basic wind tunnel setups are capable of only estimating the steady derivatives such as the angle of attack derivatives (lift coefficient $C_{L\alpha}$, pitching moment coefficient $C_{m\alpha}$) or sideslip derivatives like side force derivative $C_{Y\beta}$ or rolling moment derivative $C_{l\beta}$. But there are also experiments such as the Benchmark Active Control Technology wind tunnel model [97] which are capable of testing and measuring aeroelastic phenomena using accelerometers and strain gauges. Therefore, depending on the wind tunnel test data, parametric or dynamic uncertainties for the aerodynamic model can be defined.

4.4.2 Parametric Uncertainties

4.4.2.1 Aerodynamic Stability Derivatives

Parametric uncertainties in the aerodynamic model are associated with errors in estimating steady aerodynamics stability coefficients such as alpha derivatives of lift and pitching coefficients ($C_{L\alpha}, C_{m\alpha}$) as well as control derivatives. These values are typically obtained from fluid flow solvers of varying fidelity and updated using wind tunnel test based system identification results. If results from multiple sources are available, the uncertainties can be specified as to account for variation in the data.

In Chapter 3, Eq. (3.33) and Eq. (3.34) show how steady, rigid body aerodynamics enter the model. The first six mode shapes in the matrix Φ are the rigid body mode shapes associated with rectilinear and rotational motion along x,y and z axes as seen in Eq. (3.33). Following the procedure described in Chapter 3 to obtain the final aerodynamic model, it can be seen that the aerodynamic model represented by $Q(s_k)$ in Eq. (4.20) can be partitioned as

$$Q(s_k) = \left[\begin{array}{c|c} Q_{rr}(s_k) & Q_{rf}(s_k) \\ \hline Q_{fr}(s_k) & Q_{ff}(s_k) \end{array} \right] \quad (4.21)$$

where Q_{rr} is a 6×6 matrix relating rigid body states to the corresponding rigid body forces, Q_{rf} contains coupling terms which represent the effect of vibrational modes on rigid body forces and moments of the aircraft, Q_{fr} is the reverse coupling matrix which relates the rigid body states to the modal forces and finally, Q_{ff} is the structural dynamics matrix which deals with pure structural dynamics of the aircraft. Therefore, the steady aerodynamics stability coefficients are a part of the Q_{rr} partition of the Q_{steady} matrices in Eq. (4.20). For example, the α derivative for lift $C_{L\alpha}$, relates the normalized heave velocity w to the force in z direction. Therefore, the parameter associated with $C_{L\alpha}$ appears at the 3^{rd} row and 3^{rd} column of the velocity matrix of Q_{steady} , i.e. $Q_1^S(3,3)$.

4.4.2.2 Structural Parametric Uncertainties

Structural parametric uncertainties affect the aerodynamic model since it is expressed in modal coordinates as well. Although it may seem counter-intuitive that uncertainties related to structural model affect aerodynamics, it must be remembered that aerodynamic model is also projected into the eigenspace of the structural model for compatibility, as explained in the previous chapter. Since the modal transformations via mode shapes are a function of the structural model parameters as seen in Eq. (4.6), the resulting uncertainty in the modal aerodynamic model must be taken into account. This can be accomplished using the perturbation based approach as shown.

We consider the discrete modal aerodynamic model $Q(k)$ obtained at a given reduced frequency k . Let δp be the set of structural parametric perturbations. The resulting perturbation in $Q(k)$ is given by

$$\delta Q(k) = \sum_{j=1}^n \frac{\partial Q(k)}{\partial p_j} \delta p_j \quad (4.22)$$

Now, the partial derivative $\frac{\partial Q(k)}{\partial p_j}$ can be evaluated using the expression for $Q(k)$ as

described in Eq. (3.34), reproduced here as well.

$$Q(k) = \Phi^T \underbrace{T_{as}^T S[AIC(k)](D_1 + ikD_2)T_{as}}_{Q_{aero}} \Phi \quad (4.23a)$$

$$\frac{\partial Q(k)}{\partial p_j} = \underbrace{\Phi^T \frac{\partial Q_{aero}(k)}{\partial p_j} \Phi}_{=0} + 2\Phi^T Q_{aero}(k) \frac{\partial \Phi}{\partial p_j} \quad (4.23b)$$

As indicated, the first term in Eq. (4.23)b is zero since the core aerodynamic model itself does not depend on any structural model parameters. The second term essentially represents the uncertainty in modal transformation due to uncertainty in model parameters of the structural model. The eigenvector derivative may be computed via Nelson's method shown in Eq. (4.11). To obtain a continuous model with these uncertainties, rational function fitting can be carried out for the partial derivative $\frac{\partial Q(k)}{\partial p_j}$ computed at various reduced frequencies, using the same basis function described in Eq. (3.39). Then, using coefficients of the parametric perturbations in Eq. (4.22), uncertainty in aerodynamics may be written as

$$\Delta_{Q(s_k)} = \sum_{j=1}^n \frac{\partial Q(s_k)}{\partial p_j} W_{p_j} \Delta p_j \quad (4.24)$$

Thus, we can now use Eq. (4.24) to obtain uncertainty in modal aerodynamic model due to parametric uncertainties in structural model.

4.4.3 Dynamic Uncertainties

Since there is an unsteady component associated with aerodynamics which is frequency dependent as discussed in previous chapters, the corresponding uncertainty is best represented using a dynamic uncertainty. Since there are typically no experiments or tests dedicated to unsteady aerodynamics, this uncertainty typically represents the errors arising from assumptions and approximations made in the theoretical model. For instance, the rational function fitting has fitting errors which may need to be accounted for. Also, it may be necessary to account for unmodeled dynamics at high frequencies. Finally, if data from wind tunnel tests or flight tests is available for unsteady effects in aerodynamics, a general dynamic uncertainty across the frequency range of interest can be defined which accounts for any deviation of experimental data from the theoretical model. These uncertainties are applied for the

unsteady part of the aerodynamic model, since the steady aerodynamics modeling and the corresponding uncertainties are dealt with separately and then combined to get the overall uncertain aerodynamic model.

The overall uncertain aeroelastic model can be obtained by combining the uncertain structural and aerodynamic models. The next section provides the details of the uncertain structural and aerodynamic models constructed for the BFF vehicle.

4.5 Uncertain Model for BFF Vehicle

Ground tests conducted for the BFF vehicle included static deformation tests on the wing spars to determine material properties, inertia swing tests for moments of inertia about the three axes and ground vibration tests for vibrational response under dynamic external loading. For the aerodynamic model, wind tunnel tests have been carried out to determine steady aerodynamic stability derivatives for angle of attack. The inertia swing tests and static deformation tests are conducted to provide initial values for structural model parameters. The GVT data is used for model updating [11]. Since wind tunnel data is available only for a small part of the aerodynamic model, the data is used as a part of a set of data points used for determining bounds on parametric uncertainties associated with stability derivatives. The following subsections provide details on the data obtained from these experiments and the procedure involved in specifying uncertainties using that data.

4.5.1 Parametric uncertainties in structural model

By carefully accounting for various sources of measurement errors in static tests and inertia swing tests conducted for values of various model parameters, an estimation is obtained for magnitude of the errors [15]. Bounds on the associated parametric uncertainties is determined from these estimates. The model parameters taken into account are Young's modulus (E) and Shear modulus (G) of the wing spar, pitching moment of inertia (I_{yy}) and location of center of mass of the aircraft. The uncertainties are specified in either multiplicative or additive form as described in Eq. (4.1). Based on the error estimates in [15], bounds on the parametric uncertainties are determined as follows.

As mentioned earlier, the location of center of gravity does not enter the structural model parametrically. Therefore in order to compute the relevant eigenvector, mass

Table 4.1: Weights for structural parametric uncertainties and corresponding bounds

Uncertainty	Type	Source	Weight	Bound
Δ_E	Multiplicative	Young's Modulus	0.1	$\pm 10\%$
Δ_G	Multiplicative	Shear Modulus	0.1	$\pm 10\%$
$\Delta_{I_{yy}}$	Multiplicative	Pitch Mom. of Inertia	0.05	$\pm 5\%$
$\Delta_{x_{cg}}$	Additive	Center of Gravity	0.02	$\pm 0.02\text{m}$

and stiffness matrix derivatives, an equivalent parameter is created in the form of a concentrated point mass load at the cargo area node of the aircraft. The node is located forward to the C.G. location. Since point masses related to flight computers and sensors is already modeled at that node, an additional variable point mass is added to it. This added mass parameter can be used to handle uncertainty in C.G. location as follows.

Let total mass of the aircraft be denoted M , distance of the cargo area node from C.G. be d and added variable mass at that node δm , all in SI units. It should be noted that the same parameter is subtracted from the point mass at the C.G. node to keep the mass of the aircraft constant at M . Then as δm varies, the distance of new C.G. location from the original location varies as

$$x_{cg} = \delta m \frac{d}{M} \quad (4.25)$$

Therefore, after computing the partial derivatives with respect to the added mass parameter δm , Eq. (4.25) can be used to indirectly compute the derivatives with respect to C.G. location as

$$\frac{\partial M}{\partial x_{cg}} = \frac{\partial M}{\partial \delta m} \frac{M}{d} \quad (4.26a)$$

$$\frac{\partial K}{\partial x_{cg}} = \frac{\partial K}{\partial \delta m} \frac{M}{d} \quad (4.26b)$$

$$\frac{\partial \Phi}{\partial x_{cg}} = \frac{\partial \Phi}{\partial \delta m} \frac{M}{d} \quad (4.26c)$$

Eqs. (4.26) can now be used to compute the partial derivatives of modal mass and stiffness matrices with respect to C.G. location as shown in Eq. (4.10). Then uncertainty in modal mass and stiffness matrices can be constructed as

$$\Delta_{M_{mod}} = \frac{\partial M_{mod}}{\partial E} E_0 W_E \Delta_E + \frac{\partial M_{mod}}{\partial G} G_0 W_G \Delta_G + \frac{\partial M_{mod}}{\partial I_{yy}} I_{yy0} W_{I_{yy}} \Delta_{I_{yy}} + \frac{\partial M_{mod}}{\partial x_{cg}} W_{cg} \Delta_{x_{cg}} \quad (4.27a)$$

$$\Delta_{K_{mod}} = \frac{\partial K_{mod}}{\partial E} E_0 W_E \Delta_E + \frac{\partial K_{mod}}{\partial G} G_0 W_G \Delta_G + \frac{\partial K_{mod}}{\partial I_{yy}} I_{yy0} W_{I_{yy}} \Delta_{I_{yy}} + \frac{\partial K_{mod}}{\partial x_{cg}} W_{cg} \Delta_{x_{cg}} \quad (4.27b)$$

Here W_p are the weights associated with the parameters $p = \{E, G, I_{yy}, x_{cg}\}$, whereas E_0 , G_0 and I_{yy0} are the nominal values of Young's modulus, shear modulus and pitching moment of inertia. The partial derivatives can be computed as shown in Eq. (4.10). The overall uncertain modal mass and stiffness matrices may now be written using Eq. (4.12). It should be noted that there are other model parameters such as mass distribution which are not included here. Only those parameters which form a part of the ground tests can be included in this analysis. However, GVT provides an opportunity to include additional variables. For including GVT data associated with mode shapes, we project the mode shape errors on to a set of model parameters. This set can be extended to include parameters we did not include above.

4.5.2 Uncertainties from GVT data

Modal data for the BFF vehicle is obtained via ground vibration tests conducted in the UAV laboratory [10, 11]. The data is primarily used for updating the finite element model constructed using data from static ground tests and mass properties tests described earlier. However, the data can also be used to determine uncertainties in the structural model. As discussed in preceding section, differences in the experimentally and theoretically obtained modal data can form the basis for computing bounds on parametric uncertainties for the structural model. However, some processing of GVT data is required to obtain the mode shape differences as discussed further.

From the GVT data obtained, the fundamental frequencies and their corresponding mode shapes are obtained in terms of heave data at the locations of sensors across the aircraft body as shown in Fig. 4.3.

Mode shapes from the structural model are obtained as a function of location of the nodes of the finite element model since mode shapes are essentially the eigenvectors

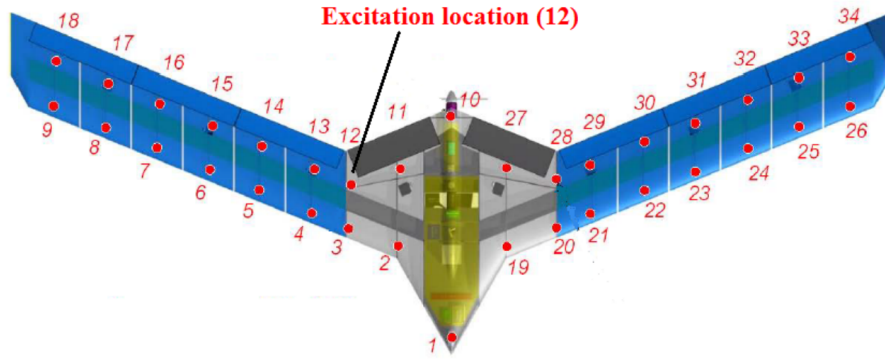


Figure 4.3: Sensor locations for GVT tests

of the model. Therefore, the GVT data in its original form is incompatible with the mode shapes obtained theoretically. To transform the estimated GVT mode shapes into the eigenspace obtained from the FE model, a thin plate splining function is used to carry out the interpolation. For the first structural mode corresponding to the first symmetric bending, the spline is shown in Fig (4.4).

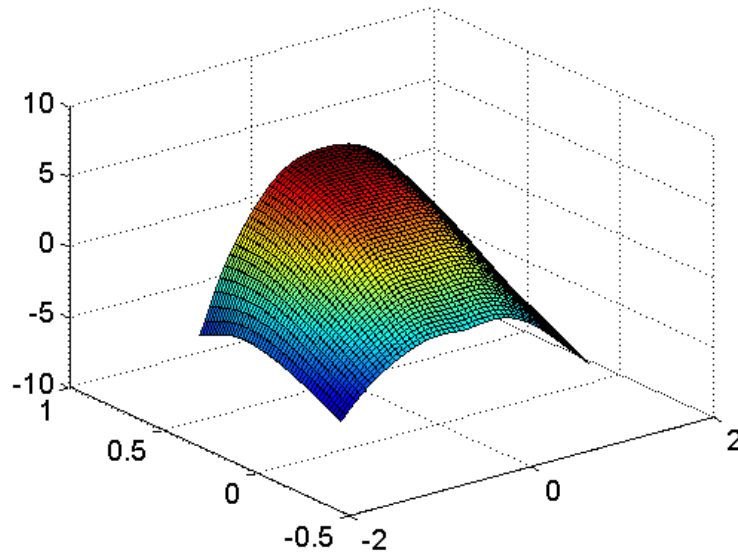


Figure 4.4: Thin plate spline for extracting mode shape data from GVT tests

It should be noted that some of the data points from the GVT test which cause unrealistically sharp deviations in the spline surface are ignored in the construction. The resulting first mode shape from the GVT is compared against that obtained from FE model after splitting them into three parts corresponding to heave, bend and twist

degrees of freedom of each node as shown in Fig. 4.5.

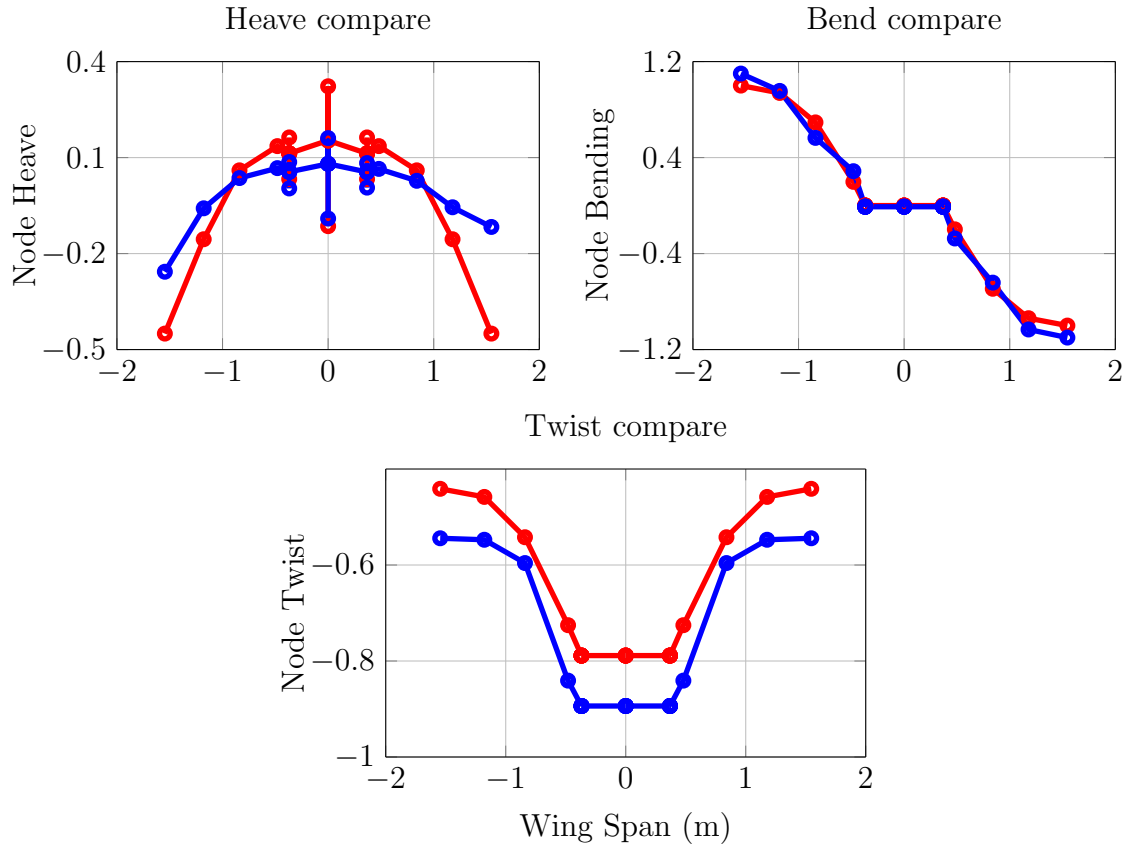


Figure 4.5: Mode shape errors between GVT data (—●—) and FE model (—●—)

As seen in Fig. 4.5, the heave portion of the mode shape does not match very well, whereas the bend and twist portions match very well. Possible reasons for ill-matching in heave is additional dynamics due to the spring from which the aircraft is mounted which is not taken into account in the theoretical model and sensor faults like loose attachments to the airframe. For the BFF vehicle, only the first structural mode is considered for computing parametric uncertainties since it is the dominant mode involved in body freedom flutter.

As described in section 4.3, an iterative least squares procedure is applied to determine the parametric uncertainty bounds which adequately represent the mode shape data from the GVT. We first check if the set of parametric uncertainties defined in Table 4.1 is adequate for this purpose. We compute the mode shape perturbations generated by parameter perturbations of magnitude equal to the upper bound of the uncertainties as specified in Table 4.1. We then compare the mode shape perturbations to the mode

shape differences seen in Fig. 4.5 to determine whether the parametric uncertainties can account for these differences.

Let $\delta\Phi_{GVT}$ denote the difference between mode shapes obtained from FE model and GVT data respectively and $\delta\Phi_{par}$ be the mode shape perturbations computed from positive parametric perturbations using Eq. (4.16). We require that the absolute value of $\delta\Phi_{par}$ *over bounds* that of $\delta\Phi_{GVT}$ for each constituent element. Fig. 4.6 plots the absolute values of the entries of both these vectors for comparison. In Fig. 4.6,

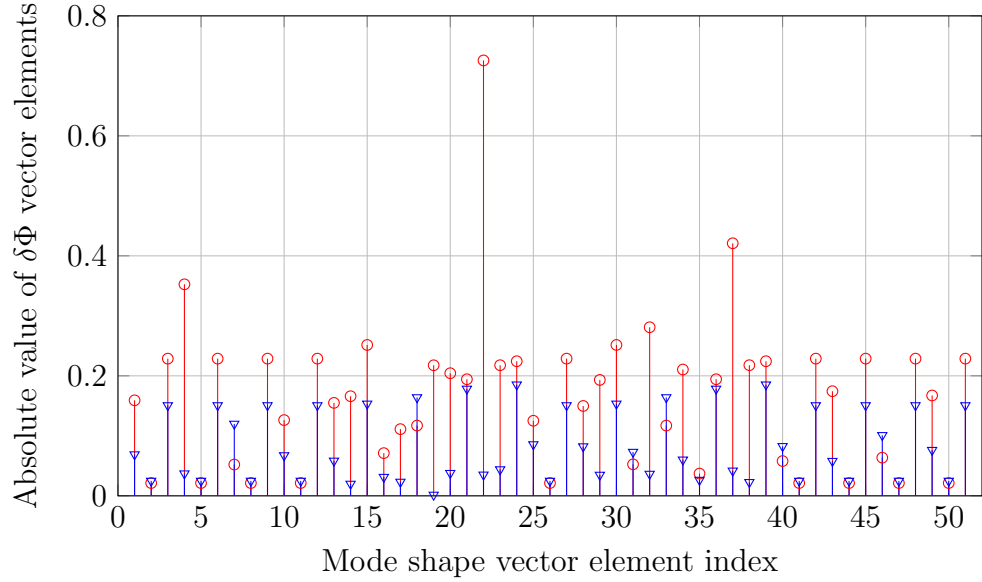


Figure 4.6: Mode shape error comparison: GVT-FEM difference (\circ), Theoretical perturbation due to parameters (∇)

each vertical line represents the absolute value of every element of $\delta\Phi_{GVT}$ and $\delta\Phi_{par}$. Absolute values are plotted since the parametric uncertainty bounds specified corresponding to $\delta\Phi_{par}$ range from positive to the negative of the perturbation values, shown in Table 4.1. For instance, if the C.G. position is perturbed by 0.03 m/s, the resulting mode shape shape perturbation computed from Eq. (4.15) may have elements with signs opposite to those obtained from GVT data. However, the sign differences can be ignored since the C.G. uncertainty is modeled as ± 0.03 m/s. Therefore as long as the absolute values of the mode shape differences are accounted for using positive parametric perturbations, the uncertainty specifications are adequate.

As we can see, perturbation in the first mode shape generated due to parametric perturbations based on uncertainty specifications in Table 4.1 do not sufficiently over

bound the mode shape differences seen between GVT data and FE model. This means that incorporating parametric uncertainties specified in Table 4.1 do not sufficiently represent the deviations in mode shapes between the theoretical model and GVT data. Hence, the uncertainties of the model parameters need to be modified to account for GVT data. As mentioned earlier, this also provides an opportunity to include parameters for which no static tests were conducted, since addition of new parameters helps account for the gap in experimental and theoretical modal data using lower bounds on each individual uncertainty. In other words, if uncertainty in mode shapes is represented using a higher number of parameters, bounds on each of the parametric uncertainties is potentially lower.

The model parameter set is expanded to include mass distribution between the wings and center body. The mass of the center body is essentially modeled as a point mass at the center of gravity, while mass of the wing is in terms of mass per unit length along the spar. By adding a small perturbation δmd to the wing spar's mass per unit length parameter, and subtracting the resulting added mass from the center body, we can effectively redistribute the mass by a small amount. Mass of the wings and center body is measured very accurately, which is why including this parameter would normally be considered unnecessary. However, it should be remembered that for the BFF vehicle, masses of individual airframe components was not available. Also, the vehicle is suspended from a light spring during its GVT testing, and addition of extra sensors and attachments inducing dynamic forcing may add to the apparent mass. Also, this accounts for differences in mass occurring after the initial measurements, due to additional repairs, change of electronics and even regular wear and tear. Finally, an important source of error is the finite element modeling process, in which a nominal wing mass distribution is assumed and point masses and inertias are added to bring the overall mass and moments to the experimentally measured values. The uncertainty corresponding to this parameter Δ_{md} helps account for small errors in these assumptions.

The iterative least squares procedure is used owing to its simplicity. It is modified so that the difference between absolute values of $\delta\Phi_{GVT}$ and $\delta\Phi_{par}$ are minimized, for reasons discussed earlier. It is determined from iterative least squares that in addition to uncertainties in other parameters specified in Table 4.1, a 10% uncertainty in mass distribution and $\pm 3\text{cm}$ uncertainty in C.G. location satisfactorily accounts for mode shape data differences. Perturbations in other parameters such as bending and

torsional stiffness do not seem to contribute to mode shape perturbations significantly. This is discussed in detail later. The comparison of $\delta\Phi_{par}$ and $\delta\Phi_{GVT}$ based on the updated parameter set can be seen in Fig. 4.7.

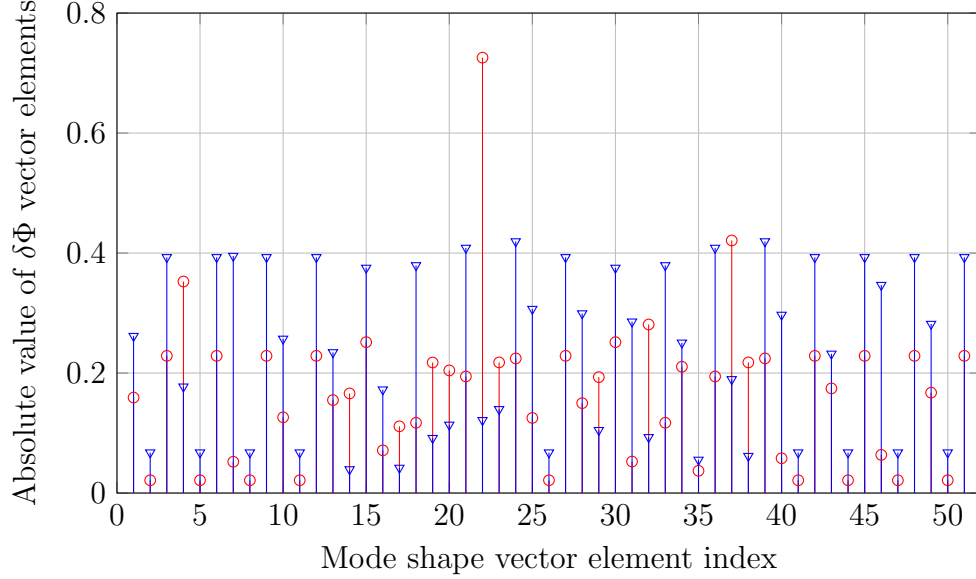


Figure 4.7: Mode shape error comparison: GVT-FEM difference (\circ), Perturbation due to parameters (∇)

In Fig. 4.7 we see that there are a few elements within $\delta\Phi_{GVT}$ which are not completely over bounded by the corresponding entries of $\delta\Phi_{par}$. However, a closer inspection of these elements reveals that most of them belong to the heave portion of the mode shape. Element number 22 for example, which corresponds to the largest element in $\delta\Phi_{GVT}$ and is much larger than the corresponding element in $\delta\Phi_{par}$, represents the heave of node 8 at the left wing tip of the aircraft. Fig. 4.5 confirms that at the left wing tip, heave portion of the mode shapes are the most ill-matched. Therefore, in order to avoid overly conservative uncertain models, the solution obtained from iterative least squares is considered acceptable. Now, since the C.G. location parameter was only designated a $\pm 2\text{cm}$ uncertainty and mass distribution was not among the parameters considered in Table 4.1, the parametric uncertainties are modified to include these new parameters and bounds.

It is interesting to note that mode shapes show sensitivity only to parameters associated with mass properties of the aircraft. It requires exceptionally large perturbations in Young's modulus or shear modulus to generate significant mode shape perturba-

tions using Eq. (4.15). In other words, changing stiffness properties of the aircraft does not affect the resulting mode shapes significantly. On the other hand, eigenvalues, associated with natural frequencies of the system, seem to be exclusively affected by stiffness properties as opposed to mass properties. This phenomenon is an interesting area for further study.

The final set of parametric uncertainties along with their bounds are given in Table 4.2. The uncertain modal mass and stiffness matrices can be constructed as described in Eq. (4.28).

Table 4.2: Weights for structural parametric uncertainties and corresponding bounds

Uncertainty	Type	Source	Weight	Bound
Δ_E	Multiplicative	Young's Modulus	0.1	$\pm 10\%$
Δ_G	Multiplicative	Shear Modulus	0.1	$\pm 10\%$
$\Delta_{I_{yy}}$	Multiplicative	Pitch Mom. of Inertia	0.05	$\pm 5\%$
Δ_{xcg}	Additive	Center of Gravity	0.03	$\pm 0.03m$
Δ_{md}	Multiplicative	mass distribution	0.1	$\pm 10\%$

$$\begin{aligned} \Delta_{M_{mod}} = & \frac{\partial M_{mod}}{\partial E} E_0 W_E \Delta_E + \frac{\partial M_{mod}}{\partial G} G_0 W_G \Delta_G + \frac{\partial M_{mod}}{\partial I_{yy}} I_{yy0} W_{I_{yy}} \Delta_{I_{yy}} \\ & + \frac{\partial M_{mod}}{\partial x_{cg}} W_{cg} \Delta_{xcg} + \frac{\partial M_{mod}}{\partial md} md_0 W_{md} \Delta_{md} \end{aligned} \quad (4.28a)$$

$$\begin{aligned} \Delta_{K_{mod}} = & \frac{\partial K_{mod}}{\partial E} E_0 W_E \Delta_E + \frac{\partial K_{mod}}{\partial G} G_0 W_G \Delta_G + \frac{\partial K_{mod}}{\partial I_{yy}} I_{yy0} W_{I_{yy}} \Delta_{I_{yy}} \\ & + \frac{\partial K_{mod}}{\partial x_{cg}} W_{cg} \Delta_{xcg} + \frac{\partial K_{mod}}{\partial md} md_0 W_{md} \Delta_{md} \end{aligned} \quad (4.28b)$$

4.5.3 Parametric Uncertainties in Aerodynamic Model

A basic wind tunnel test has been carried out for a scaled model of the BFF vehicle. The results from wind tunnel tests provide data for only two parameters - the angle of attack (α) derivatives of lift coefficient ($C_{L\alpha}$) and pitching moment coefficient ($C_{m\alpha}$). Therefore, data from other sources such as open source flow solvers is also incorporated into the uncertain model.

The steady aerodynamics model is obtained from a VLM code as discussed in Chapter 3. However, several other open source VLM codes are available for researchers such

as XFLR-5 by Drela [68] and TORNADO [98]. Both these codes have been used to compute aerodynamic stability derivatives as well. Also, a doublet lattice code solution for BFF vehicle along with steady aerodynamics solution was provided by DLR [63]. Combining data from all these sources, a set of nominal values as well as uncertainty bounds are determined which account for the small differences in the data. Since we only have experimental data related to longitudinal aerodynamics forces, we only specify uncertainties for α and q (pitch rate) derivatives, listed in Table 4.3.

Table 4.3: Weights for aerodynamic parametric uncertainties and corresponding bounds

Uncertainty	Source	Weight	Bound
$\Delta_{C_{L\alpha}}$	Lift - α derivative	0.1	$\pm 10\%$
$\Delta_{C_{M\alpha}}$	Pitching Mom. - α derivative	0.05	$\pm 5\%$
$\Delta_{C_{Lq}}$	Lift - pitch rate derivative	0.1	$\pm 10\%$
$\Delta_{C_{Mq}}$	Pitch damping derivative	0.05	$\pm 5\%$

Finally, as discussed in the previous section, parametric uncertainties in structural dynamics also affect the aerodynamic model since it is in modal coordinates. The uncertainty can be constructed as shown in Eq. (4.29)

$$\Delta_{Q(s_k)} = \frac{\partial Q(s_k)}{\partial E} E_0 W_E \Delta_E + \frac{\partial Q(s_k)}{\partial G} G_0 W_G \Delta_G + \frac{\partial Q(s_k)}{\partial I_{yy}} I_{yy0} W_{I_{yy}} \Delta_{I_{yy}} + \frac{\partial Q(s_k)}{\partial x_{cg}} W_{cg} \Delta_{x_{cg}} + \frac{\partial Q(s_k)}{\partial md} W_{md} \Delta_{md} \quad (4.29)$$

The required partial derivatives can be computed as described in Eq. (4.23). $\Delta_{Q(s_k)}$, along with uncertainties listed in Table 4.3 together make up the parametric uncertainties in the aerodynamic model. The stability derivative uncertainties in Table 4.3 can be incorporated into the aerodynamic model by adding them to their corresponding nominal values within the GAM $Q(s_k)$ which can be written as shown in Eq. (4.20). The procedure is described in section 4.4.2.

4.5.4 Dynamic Uncertainty in Unsteady Aerodynamics

For the BFF vehicle, we consider a dynamic uncertainty in the unsteady part of the aerodynamic model which accounts for the fitting errors in the rational function

fitting carried out via least squares. Since the fitting is carried out over a given frequency range, the fitting errors vary with frequency. Therefore we define a linear time invariant (LTI) uncertain element Δ_{unS} with gain bound of unity. The weighting associated with the uncertainty decides the magnitude of uncertainty as a function of frequency. The frequency dependent weighting function is therefore determined keeping the fitting errors in mind. Fig. 4.8 shows the Bode plot of one of the fitted input-output transfer functions of the aerodynamic model $Q(s_k)$ along with the raw data used for the fitting.

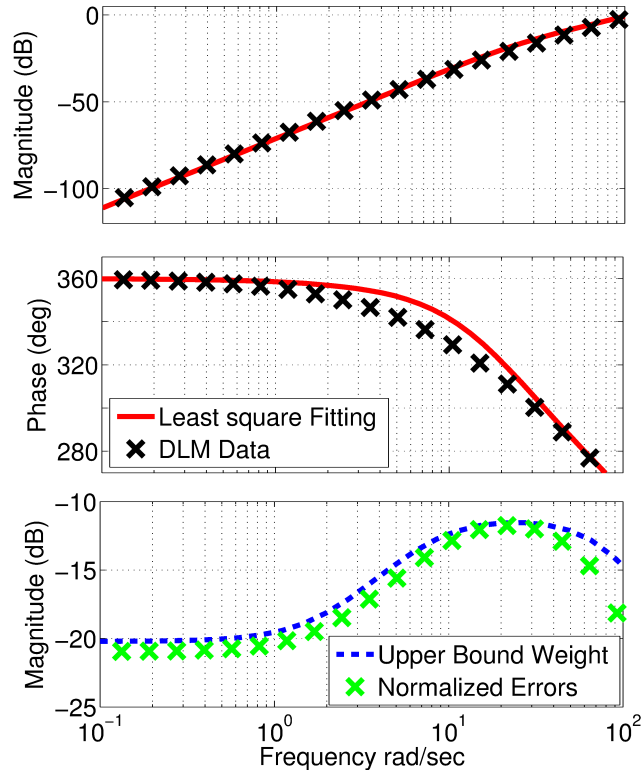


Figure 4.8: Rational Function Fitting of Unsteady Aerodynamics

The bottom plot in Fig. 4.8 shows the normalized fitting errors for that input-output channel as a function of frequency. The weighting function for the dynamic uncertainty is required to be an upper bound on the fitting errors. This is achieved by first fitting the errors across all input-output channels which are considered uncertain to a MIMO transfer function, then increasing the magnitude of that transfer function by 5% to ensure the over bound. The transfer function for fitting errors in this particular input-output channel is shown along with the fitting errors in the same bottom plot. As we can see, the fitted function in Fig. 4.8 suitably covers the magnitude of error

due to function fitting.

For the BFF vehicle, all the output channels corresponding to the first bending mode η_1 are considered for uncertainty. Essentially, the column in $Q(s_k)$ corresponding to the first symmetric bending mode is multiplied by the appropriate weight and the dynamic uncertain element. This selective application of dynamic uncertainty is carried out to prevent conservative results. Also, since uncertainty in steady state dynamics associated with heave and pitching moment are already accounted for via parametric uncertainties in stability derivatives, a dynamic uncertainty associated with the first wing bending mode complements them and covers all the dynamics involved in body freedom flutter.

Frequency weighting for this is defined as the MIMO transfer function constructed by using RFA fitting errors as described above for the column of $Q(s_k)$ associated with the first symmetric bending mode. Let the column be denoted $Q^{\eta_1}(s_k)$. The weighting functions obtained from normalized fitting errors for each RFA fitted transfer function in $Q^{\eta_1}(s_k)$ are considered in the form of a diagonal matrix $W_{\Delta_{unS}}$. Then, the overall uncertain column can be written as

$$\tilde{Q}^{\eta_1}(s_k) = Q^{\eta_1}(s_k) [I + W_{\Delta_{unS}}] \quad (4.30)$$

The uncertain column $\tilde{Q}^{\eta_1}(s_k)$ can directly replace the nominal column $Q^{\eta_1}(s_k)$ within the aerodynamic model, thus providing output dynamic uncertainty for unsteady aerodynamics associated with the first bending mode.

4.6 Summary

In summary, this chapter discusses the methods and tools used for uncertainty modeling in aeroelastic systems constructed as described in the previous two chapters. A sub-system based approach is selected for identifying and incorporating uncertainties by looking at structural/rigid body dynamics and aerodynamics individually. Both parametric and systemic (dynamic) uncertainties are considered in a unified manner, keeping in mind the overall conservativeness of the uncertain model. The key challenge of incorporating experimental data from ground tests into models expressed in modal coordinates is given special attention, and important mathematical tools derived and used for that purpose.

The next chapter outlines the construction of state-space models based on the equations derived in Chapters 2 and 3 as well as the uncertainty descriptions discussed in this chapter. Uncertain state space models are used for robust flutter analysis as well as sensitivity analysis.

Chapter 5

Robust Flutter Analysis

Flutter is a dynamic instability which occurs in flexible structures due to unstable interactions between aerodynamics, structural dynamics and rigid body dynamics [2,3]. It can cause severe performance degradation and even loss of aircraft. Therefore, flutter analysis is one of the most basic and important parts of the study of aeroservoelastic systems. For flexible aircraft, flutter analysis is essential for determining the flight envelope of the aircraft.

Flutter can occur in different ways and affect various areas of the aircraft. For example, the body freedom flutter, where the first wing bending mode combines in an unstable manner with the short period mode, affects the entire airframe. On the other hand, there are several forms of control surface flutter which combine control surface motion along with some nonlinear free play of the actuators and structural modes of the aircraft [99,100]. Since World War I when emphasis was put on fast and maneuverable aircraft designs, flutter has been a major design concern and challenge for aircraft designers [3,101]. Today, as emphasis increases on lightweight composite structures which increase the flexibility of the airframe, flutter continues to be a major design challenge to be addressed.

Flutter analysis involves identifying the flight conditions like airspeed, Mach number, altitude and the maneuvers under which flutter occurs. The critical flight condition at which flutter occurs is called the flutter boundary. Although many computational methods have been developed to predict onset of flutter, flight testing has consistently played a vital role in determining the true flutter boundary of new aircraft

designs [101, 102]. Since flight testing new aircraft or a known aircraft beyond its stipulated flight envelope runs the risk of damage or even loss of aircraft, there has been persistent effort towards developing ever more reliable and sophisticated methods for predicting flutter computationally.

Flutter prediction or flutter boundary computation can be accomplished in different ways depending on the aeroservoelastic model at hand and desired computational expense. High fidelity computations can be carried out using a model which is constructed using computational fluid and structural dynamics (CFD/CSD modeling) [49, 50, 103]. These methods are known to considerably increase the accuracy of flutter prediction, but at a large computational cost. The number of states in these models is typically of the order ranging from ten million to a billion, which makes them unsuitable for real time, onboard computations for flutter prediction. Furthermore, these models are also unsuitable for any control design due to the prohibitively long runtime of the associated simulations. This necessitates computation methods which involve simpler models of low to medium fidelity and low number of states.

In Chapter 2 and Chapter 3, an aeroelastic model for the BFF vehicle in mean axes frame involving linear structural dynamics and unsteady aerodynamics has been developed. While structural dynamics modeling is done using a linear Euler beam based finite element model, the aerodynamic model is based on the doublet lattice method (DLM). The DLM provides the aerodynamic model in the reduced frequency domain, where reduced frequency is a function of frequency and airspeed (see Chapter 3, Eq. (3.6)). Combining the aerodynamic forces computed from the DLM with the linearized equations of motion in the mean axes, the complete equations describing the dynamics of the BFF vehicle are obtained. These equations can be developed for a flight condition, and expressed in the form of a standard state-space model [18]. The state space model can then be used for stability analysis (in this case flutter analysis) as well as control design. Therefore in addition to the matrix equation related to state dynamics, the model needs to include an appropriate output vector equation which provides outputs for feedback control design. The construction of the state space model for the BFF vehicle is described in section 1.

The state space model for the BFF aircraft can be used in one of the several flutter analysis methods developed over the decades. Owing to the popularity of both finite element modeling and DLM (and other such potential flow based methods), several

flutter boundary computation methods have been developed for aeroelastic models similar to the model developed in this chapter [104–106]. An overview of some of these methods is presented in section 2, which also describes the procedure used for the BFF vehicle and compares it to the classical methods.

A major drawback of using low to medium fidelity models is the inherent inaccuracies owing to simplifications and approximations. Errors in parametric values used in a model coupled with systemic errors due to linearity assumptions as well as unmodeled dynamics can make reliable prediction of flutter boundary a difficult task. To overcome this difficulty, uncertain models can be constructed which account for uncertainties in parametric values as well as model form uncertainties due to unmodeled or linearized dynamics. Depending on the method used for constructing the uncertain model, a stability analysis procedure can be formulated which calculates the worst case flutter boundary for the uncertainties specified. Chapter 4 describes the uncertainty modeling carried out for model parameters as well as some subsystems the BFF vehicle. The uncertainty models are constructed within the framework of robust control theory which utilizes structured singular value (μ) analysis to address the problem of robust stability. The flutter boundary computed using μ is usually referred to as the robust flutter boundary.

In this chapter we look at robust flutter analysis for the BFF vehicle using the μ framework where the effects of different modeling errors on flutter prediction are taken into account. The structured singular value (μ) is a widely used measure of robust stability for systems with predefined uncertainties [17, 18]. A short summary of μ analysis is provided in section 3. The uncertainties considered can range from unmodeled high frequency dynamics to parametric errors in the model. The μ based framework has been used in recent years to carry out robust flutter analysis for aeroservoelastic systems [19, 20]. Lind and Brenner have also demonstrated the method for updating model uncertainties using flight data, both offline and in real time during flight [21]. It should be noted that a more general approach for representing modeling errors, called the Integral Quadratic Constraints (IQCs), is also used as a framework for flutter analysis [22–24] which accounts for various nonlinearities in the model in addition to the above mentioned uncertainties.

Finally, a procedure for sensitivity analysis for the BFF vehicle based on the robust flutter analysis method is described in section 4. The objective of this analysis is

to study sensitivity of the predicted robust flutter boundary to variation in bounds of each individual uncertainty description. This analysis helps us find out which parameters or subsystems need to be modeled with improved accuracy in order to reduce the conservativeness of the corresponding robust flutter boundary prediction.

5.1 State Space Model

The state space model for BFF vehicle is derived from the linear model obtained in Chapters 2 and 3. Specifically, Eq. (2.44) in Chapter 2 can be combined with Eq. (3.37) in Chapter 3 to obtain the complete linear equations of motion at a given trim condition, as shown in Eq. (5.1).

$$m[\Delta\dot{u} + \Delta qW + g\Delta\theta] = \bar{q}[Q_x] \begin{bmatrix} \eta^T & u^T \end{bmatrix}^T \quad (5.1a)$$

$$m[\Delta\dot{v} - \Delta pW + \Delta rU - g\Delta\phi] = \bar{q}[Q_y] \begin{bmatrix} \eta^T & u^T \end{bmatrix}^T \quad (5.1b)$$

$$m[\Delta\dot{w} - \Delta qU] = \bar{q}[Q_z] \begin{bmatrix} \eta^T & u^T \end{bmatrix}^T \quad (5.1c)$$

$$I_{xx}\Delta\dot{p} - I_{xz}\Delta\dot{r} = \bar{q}[Q_\phi] \begin{bmatrix} \eta^T & u^T \end{bmatrix}^T \quad (5.1d)$$

$$I_{yy}\Delta\dot{q} = \bar{q}[Q_\theta] \begin{bmatrix} \eta^T & u^T \end{bmatrix}^T \quad (5.1e)$$

$$I_{zz}\Delta\dot{r} - I_{xz}\Delta\dot{p} = \bar{q}[Q_\psi] \begin{bmatrix} \eta^T & u^T \end{bmatrix}^T \quad (5.1f)$$

$$\ddot{\eta}_j + \tilde{\omega}^2\eta_j = \bar{q}[Q_{\eta_f}] \begin{bmatrix} \eta^T & u^T \end{bmatrix}^T \quad (5.1g)$$

where η is a column vector containing both rigid body states $\eta_r := [x \ y \ z \ \phi \ \theta \ \psi]^T$ and m structural vibration states $\eta_f := [\eta_1 \ \eta_2 \ \dots \ \eta_m]^T$ while u is the set of control surface inputs. The matrices on the right hand side, generally referred to here as Q_X , are essentially row-wise partitions of the generalized aerodynamics matrix $Q(s_k)$ shown in Eq. (3.37). The partitions are in accordance with the rigid body and structural generalized coordinates of the mean axes. It follows that the terms on right-hand side of Eq. (5.1) are in frequency domain, since s_k represents the reduced Laplace variable. Therefore, Eq. (5.1) is written in a *mixed* domain comprising of both time and frequency domain terms. This can be resolved as discussed ahead.

The first step is to consolidate the equations in (5.1) into a matrix form comprising of overall mass and stiffness matrices and rewriting them in a pseudo state space form

as shown below.

$$\begin{bmatrix} \dot{\eta}(t) \\ \dot{\eta}(t) \end{bmatrix} = \begin{bmatrix} 0 & I \\ M^{-1}K & M^{-1}E \end{bmatrix} \begin{bmatrix} \eta(t) \\ \dot{\eta}(t) \end{bmatrix} + \begin{bmatrix} 0 \\ I \end{bmatrix} Q(s_k) \begin{bmatrix} \eta(s_k)^T & u(s_k)^T \end{bmatrix}^T \quad (5.2)$$

The matrices M , K and E are overall mass, stiffness and damping matrices which include the vehicle mass m , moments of inertia, modal mass, stiffness and damping matrices associated with structural dynamics. Next, $Q(s_k)$ is rewritten in the time domain. As seen in Chapter 3, Eqs. (3.38), $Q(s_k)$ is a rational function of s_k and comprises of lag states which represent the unsteady aerodynamic lag in the model. s_k in turn is a function of the airspeed V and Laplace variable s . Therefore for a given airspeed V , $Q(s_k)$ may be rewritten as $Q(s, V)$ and may be expressed in terms of a state space matrix with aerodynamic lag terms η_{aero} as

$$\dot{\eta}_{aero}(t) = A_Q(V)\eta_{aero}(t) + B_Q^1(V)\eta(t) + B_Q^2(V)u(t) \quad (5.3a)$$

$$Q_V(t) = C_Q(V)\eta_{aero}(t) + D_Q^1(V)\eta(t) + D_Q^2(V)u(t) \quad (5.3b)$$

We can see that the state space matrices in Eq. (5.3) are expressed as a function of airspeed. This acknowledges the fact that the state space model varies with variation in the given airspeed V . Of course, in real flight the airspeed is a function of time ($V(t)$) which means that Eq. (5.3) represents a linear-parameter-varying (LPV) system. However, the DLM theory does not account for varying airspeed, which is why the model above is strictly valid for quasi-static cases. Moving further, the dependence on airspeed is dropped from notation for convenience.

Eq. (5.3) can now be incorporated into the overall state space model constructed for the BFF vehicle using Eq. (5.2). The state space model is shown in Eq. (5.4) below.

$$\begin{bmatrix} \dot{\eta} \\ \dot{\eta} \\ \dot{\eta}_{aero} \end{bmatrix} = \underbrace{\begin{bmatrix} 0 & I & 0 \\ M^{-1}K + D_Q^1 & M^{-1}E & C_Q \\ B_Q^1 & 0 & A_Q \end{bmatrix}}_A \begin{bmatrix} \eta \\ \dot{\eta} \\ \eta_{aero} \end{bmatrix} + \underbrace{\begin{bmatrix} 0 \\ D_Q^2 \\ B_Q^2 \end{bmatrix}}_B u \quad (5.4)$$

Eq. (5.4) is the desired state space model in time domain which includes rigid body, structural and aerodynamic lag states. The state and input matrices are conventionally named A and B respectively. Of course, it should be remembered that in this case the matrices A and B are also functions of the airspeed V because of aerodynamics

state space matrices involved in their construction. Therefore the overall BFF state space model is essentially a quasi-static LPV model.

To construct the synthesis model, we choose an appropriate set of outputs needed for feedback. The BFF vehicle has a total of six accelerometers as shown in Fig. 5.1. In

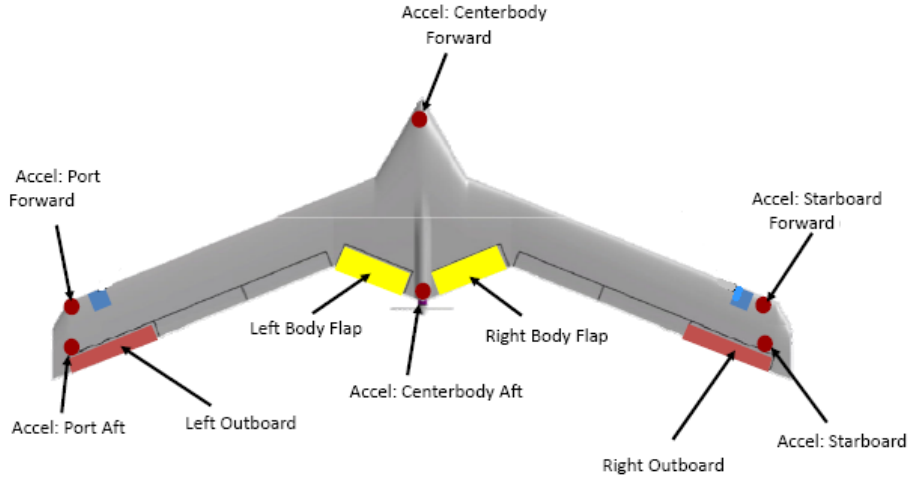


Figure 5.1: Location of accelerometers on BFF aircraft and control surfaces used for flutter suppression

addition, angular velocities of the vehicle are measured by an inertial measurement unit (IMU) located in the instruments bay in the center body. We require a controller which uses the control surfaces designated for flutter suppression, indicated in Fig. 5.1 and takes in as inputs the accelerometer outputs as well as the pitch rate provided by the IMU.

For simplifying the problem, it is assumed that the accelerometers output accelerations of the finite element nodes located closest to them, as indicated in Fig. 5.2. Similarly, pitch rate output from the IMU is simulated as the pitch rate corresponding to the node at the center of gravity, indicated by the enlarged circle in Fig. 5.2. The output matrices, conventionally named C and D , relate the states and inputs to the desired outputs. Keeping the sensors mentioned above in mind, C matrix is constructed which provides heave accelerations as well as the pitch rate of the nodes indicated in Fig. 5.2. The sensors are assumed to be fixed relative to the associated nodes. Therefore, the corresponding measurements may be simulated by adding the rigid body pitch rate q and heave acceleration \dot{w} obtained in Eq. (2.45) to the nodal

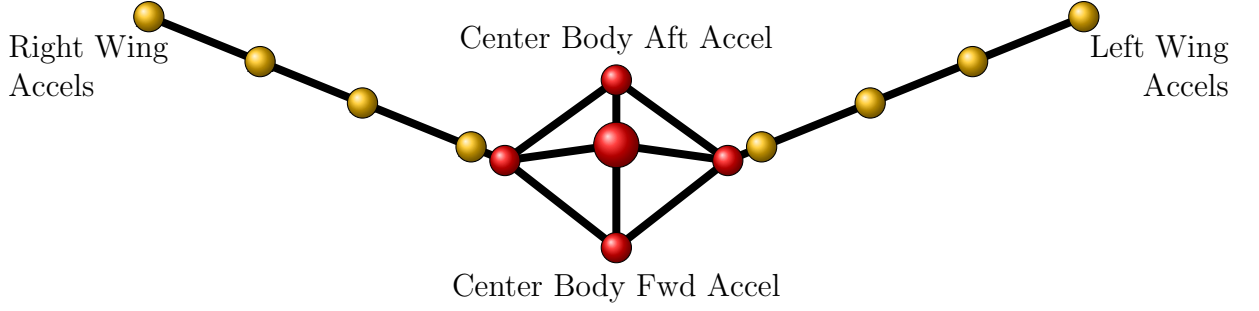


Figure 5.2: Finite Element Model

deformations.

Since the vibrational dynamics of all the nodes is expressed in terms of modal coordinates and mode shapes, the accelerations and rotational deformation also need to be expressed in the same manner. Let the collective mode shape matrix obtained for the BFF vehicle be denoted as Φ . Since each node in the BFF finite element model has three degrees of freedom (heave, bend and twist - see Chapter 2, Fig. 2.3), Φ has dimensions $3n \times n_m$ where n is the total number of nodes in the model and n_m is the number of modes considered. From Eq. (2.23) in Chapter 2, accelerations in all vibrational degrees of freedom of the nodes are given as

$$\ddot{\delta} = \Phi \ddot{\eta}_f \quad (5.5)$$

δ is a column vector of length $3n$ denoting the heave, bending and twist degrees of freedoms of each node, as shown here -

$$\delta = \left[h_1 \quad \theta_1 \quad \phi_1 \quad h_2 \quad \theta_2 \quad \phi_2 \quad \cdots \quad h_n \quad \theta_n \quad \phi_n \right]^T \quad (5.6)$$

Therefore, $\ddot{\delta}$ represents the heave, bending and twist accelerations, computed from modal accelerations denoted by $\ddot{\eta}_f$. For obtaining only heave accelerations, the corresponding rows in δ and Φ may be isolated into column vector δ_H of length n and $n \times n_m$ matrix Φ_H respectively. This is done by selecting every third row in the matrix equation in Eq. (5.5), starting with the first row. Now, total heave acceleration of the i^{th} node may be written as

$$\ddot{h}_H^i = \dot{w} + \underbrace{\Phi_H^i \ddot{\eta}_f}_{\ddot{\delta}_H^i} \quad (5.7)$$

where δ_H^i and Φ_H^i represent the i^{th} row of δ_H and Φ_H respectively. A similar approach is used to simulate the pitch rate output from the IMU. Denoting the isolated rows of δ and Φ corresponding to the twist degree of freedom of each row as δ_ϕ and Φ_ϕ respectively, we have for the i^{th} node

$$\dot{h}_\phi^i = q + \underbrace{\Phi_\phi^i \dot{\eta}_f}_{\ddot{\delta}_\phi^i} \quad (5.8)$$

Eqs. (5.7) and (5.8) are used to compute accelerations for the wing tip nodes and pitch rate at the center body node. Since pitch rate measurement is essentially a linear combination of the states of the model as seen from Eq. (5.8), the corresponding part of the C matrix is easily constructed based on that equation as shown -

$$C_q^c = \begin{bmatrix} 0 & \dots & 0 & 0 & 0 & 0 & 0 & 1 & 0 & \Phi_\phi^c & 0 & \dots & 0 \end{bmatrix} \quad (5.9a)$$

$\underbrace{\hspace{10em}}_{6+n_f} \qquad \underbrace{\hspace{10em}}_{n_{aero}}$

$$y_q^c = C_q^c \begin{bmatrix} \eta_r \\ \eta_f \\ \dot{\eta}_r \\ \dot{\eta}_f \\ \eta_{aero} \end{bmatrix} \quad (5.9b)$$

where Φ_ϕ^c refers to the row in the mode shape matrix Φ corresponding to the twist of center body node c where the IMU is assumed to be located. n_f and n_{aero} are the number of structural and aerodynamic states respectively.

On the other hand, accelerometer outputs are a linear combination of acceleration of the states, as seen in Eq. (5.7). To express them in terms of positions and velocities, A and B matrices of the state space model are incorporated into the C and D matrices,

as shown for the right wing tip accelerometer outputs here -

$$C_{accel}^{rw} = \begin{bmatrix} 0 & \dots & 0 & 0 & 0 & 1 & 0 & 0 & 0 & \Phi_{\phi}^{rw} & 0 & \dots & 0 \end{bmatrix} A \quad (5.10a)$$

$$D_{accel}^{rw} = \begin{bmatrix} 0 & \dots & 0 & 0 & 0 & 1 & 0 & 0 & 0 & \Phi_{\phi}^{rw} & 0 & \dots & 0 \end{bmatrix} B \quad (5.10b)$$

$$y_{accel}^{rw} = C_{accel}^{rw} \begin{bmatrix} \eta_r \\ \eta_f \\ \dot{\eta}_r \\ \dot{\eta}_f \\ \eta_{aero} \end{bmatrix} + D_{accel}^{rw} u \quad (5.10c)$$

Eqs. (5.10) show the construction of the output equation for right wing tip accelerometers, where Φ_{ϕ}^{rw} is the row corresponding to heave of the right wing tip node indicated in Fig. 5.2. Similar equations can be constructed for the center body and left wing accelerometers as well. The overall C and D matrices for the state space model is then obtained as

$$C = \begin{bmatrix} C_q^{cT} & C_{accel}^{cf T} & C_{accel}^{cr T} & C_{accel}^{lw T} & C_{accel}^{lw T} & C_{accel}^{rw T} & C_{accel}^{rw T} \end{bmatrix}^T \quad (5.11a)$$

$$D = \begin{bmatrix} 0 & D_{accel}^{cf T} & D_{accel}^{cr T} & D_{accel}^{lw T} & D_{accel}^{lw T} & D_{accel}^{rw T} & D_{accel}^{rw T} \end{bmatrix}^T \quad (5.11b)$$

where the superscript cf refers to the forward center-body node, cr is the rear center-body node and lw is the left wing tip node. The left and right wing tip nodes are featured twice in the matrices since they are used for both forward and rear wing tip accelerometers on either side. The final state space model has the 8 control surfaces as inputs and 7 outputs which are the pitch rate and six accelerometer outputs. For a given airspeed V , the state space model for the BFF vehicle is given as

$$\begin{bmatrix} \dot{\eta} \\ \ddot{\eta} \\ \dot{\eta}_{aero} \end{bmatrix} = A(V) \begin{bmatrix} \eta \\ \dot{\eta} \\ \eta_{aero} \end{bmatrix} + B(V)u \quad (5.12a)$$

$$\begin{bmatrix} y_q^c \\ y_{accels} \end{bmatrix} = C(V) \begin{bmatrix} \eta \\ \dot{\eta} \\ \eta_{aero} \end{bmatrix} + D(D)u \quad (5.12b)$$

where $\eta = [\eta_r \ \eta_f]^T$ as mentioned earlier and y_{accels} contains acceleration outputs for all six accelerometers. The state space matrices are constructed using Eqs. (5.4), (5.10) and (5.11) for a given airspeed V .

In the next section, the state space model described in Eq. (5.12) is used to carry out nominal flutter analysis for the BFF vehicle. The section also provides an overview of classical flutter analysis methods developed in literature and compares the BFF flutter analysis with them for a deeper understanding of the flutter analysis process.

5.2 Nominal Flutter Analysis

One of the primary objectives for building aeroservoelastic models is to analyze the behavior of such systems under different flight conditions with regards to flutter. The flight conditions under which an aeroservoelastic system begins to experience flutter is called the flutter boundary, as discussed earlier. Therefore flutter analysis, which deals with estimating the flutter boundary, is essentially a stability analysis problem. Flutter analysis can be carried out in many different ways, depending on the model under consideration. Some of the classical flutter analysis techniques are discussed first to provide some background, followed by the method and results for the BFF vehicle state space model described in the previous section.

5.2.1 Classical Flutter Analysis Background

The aeroelastic model for the BFF vehicle can be generally described as a combination of linear structural dynamics and linear, unsteady aerodynamics. We also seek to include nonlinear rigid body dynamics, which makes the modeling more challenging as seen in Chapter 2. Rigid body dynamics are important since the body freedom flutter mechanism involves coupling between the structural first wing bending and the rigid short period modes. However, many widely studied models in aeroelasticity ignore rigid body dynamics. For example, in aeroelastic systems such as a flapping wing model [107,108] or a cantilevered wing undergoing bending and torsional deformations [45,46], the rigid body dynamics are generally ignored since they do not play a role in inducing flutter. Rather, flutter occurs due to unstable interactions between two different structural modes. The equation describing flutter dynamics in such systems is conventionally written in literature as

$$\left[\frac{V^2}{c^2} Mp^2 + K - \bar{q}A(p) \right] \eta = 0; \quad (5.13)$$

where M and K are the structural mass and stiffness matrices, η is the set of generalized state variables, \bar{q} is the dynamic pressure and $A(p)$ represents the unsteady aerodynamics. p is the nondimensionalized Laplace variable given by $\frac{c}{V}s$ where s is the usual Laplace variable. V is the airspeed and c is the reference chord of the lifting surface under consideration. The derivation of the equation above may be found in any standard text for aeroelasticity [45, 46]. Eq. (5.13) is valid for small structural deformations for which linearity assumptions are deemed valid. It should be reiterated that Eq. (5.13) has been written only for flutter dynamics and in the classical sense does not contain any rigid body modes.

The mass and stiffness matrices are usually constructed using finite element methods. Depending on how the aerodynamics model is obtained, there are different approaches to solve Eq. (5.13) and compute the flutter boundary. Approaches such as the p method, k method and the $p - k$ method [104–106] and their variations have been the most prevalent methods not just in academic research but also in industry. In this subsection we briefly discuss these three methods, and later relate them to the flutter analysis done for the BFF vehicle.

5.2.1.1 p Method

If the aerodynamic model is known as a simple polynomial function of the normalized variable p in the Laplace domain, then Eq. (5.13) can be solved in a straight-forward manner. In [104], Hassig points to a simple application of the p method using quasi-steady aerodynamics, there the aerodynamic forces are a function of only positions and velocities and not accelerations. Therefore, the aerodynamic model assumes a simple form as shown.

$$A(p) = A_1p + A_0 \quad (5.14)$$

Eq. (5.14) can be substituted back in Eq. (5.13) to obtain

$$\left[\frac{V^2}{c^2} Mp^2 - \bar{q}A_1p + K - \bar{q}A_0 \right] \eta = 0 \quad (5.15)$$

We can solve for the variable p at a given airspeed by enforcing nonzero solutions for η which require the determinant consisting of the matrix coefficients in the square brackets to be zero. The zero determinant condition can be enforced to obtain a polynomial in terms of p . The order of the polynomial depends on the number of modes or states considered for the model. p is computed as a set of complex conjugate values which are the roots of the polynomial. This is essentially analogous to the characteristic polynomial for a linear system. The roots represent the damping and frequencies associated with different aeroelastic modes. p for a mode of interest may be written as

$$p = \zeta\omega \pm i\omega\sqrt{1 - \zeta^2} \quad (5.16)$$

where ζ is the damping ratio of oscillations associated with the given mode and ω is the frequency. Therefore, for a given airspeed V , Eq. (5.15) can be solved for p and the damping of the modes of interest can be obtained. By tracking the damping across a range of airspeeds, it is possible to estimate the airspeed at which damping becomes zero. The variation of damping with airspeed can be visualized via a V - ζ plot, which essentially plots the damping ratio against the set of airspeeds chosen. The airspeed where the curve intersects zero damping is the flutter boundary for the system, beyond which the system is unstable.

5.2.1.2 k Method

Several commonly used unsteady aerodynamics modeling techniques such as the doublet lattice (DLM) or other similar kernel function based methods provide discrete models in the reduced frequency domain. The models are only valid for undamped oscillations at discrete reduced frequencies. Reduced frequency can be defined as $k := \omega \frac{c}{V}$, analogous to the normalized Laplace variable p . The DLM for example, provides the aerodynamic model as a complex valued matrix $A(ik)$ for a discrete set of values of k . The p method is not capable of incorporating such models since it requires the aerodynamic model to be continuous and in the Laplace domain. Therefore, the k method is adopted for flutter analysis [104, 106].

For the k method, Eq. (5.13) is rewritten in terms of $p = ik$ as

$$\left[-M + \frac{1}{\omega^2}K - \frac{1}{2}\rho \left(\frac{c}{k}\right)^2 A(ik) \right] \eta = 0; \quad (5.17)$$

Unlike the p method, Eq. (5.17) does not inherently take into account any damping of the system since undamped harmonic oscillations are assumed for the aerodynamic model. Therefore a hysteretic, proportional damping $H := igK$ is assumed, where g is the hysteretic damping coefficient [104, 109]. Eq. (5.17) is rewritten as

$$\left[-M - \frac{1}{2}\rho \left(\frac{c}{k}\right)^2 A(ik) + \frac{1+ig}{\omega^2} K \right] \eta = 0 \quad (5.18)$$

Eq. (5.18) can be reformulated as a generalized eigenvalue problem given by

$$[L - \lambda K] \eta = 0 \quad (5.19)$$

where

$$L = -M - \frac{1}{2}\rho \left(\frac{c}{k}\right)^2 A(ik) \quad (5.20a)$$

$$\lambda = \frac{1+ig}{\omega^2} \quad (5.20b)$$

For a given range of reduced frequencies, the eigenvalue problem can be solved to obtain complex the eigenvalues values λ . Then the oscillating frequency and damping may be obtained from the eigenvalue as

$$\omega = \frac{1}{\sqrt{\text{Re}(\lambda)}} \quad (5.21a)$$

$$g = \frac{\text{Im}(\lambda)}{\text{Re}(\lambda)} \quad (5.21b)$$

where $\text{Re}(\cdot)$ and $\text{Im}(\cdot)$ denote real and imaginary parts of a complex number. In practice, k method is implemented as follows.

1. Select a range of discrete reduced frequency values k , typically beginning close to zero.
2. Compute the aerodynamics matrix and solve for the eigenvalue problem defined in Eqs. (5.20).
3. Compute values of oscillating frequency ω and hysteric damping ratio g from the eigenvalues corresponding to the modes of interest.
4. From the selected value of k and computed value ω , compute the airspeed V .

5. Repeat steps 1-4 for all values of k .
6. Collect the resulting values of airspeed and damping ratio for each mode at each reduced frequency value, plot them on a V-g plot.

The V-g plot should reveal the variation of damping for each mode as a function of airspeed. The airspeed at which damping ratio of the mode of interest crosses $g = 0$ line and becomes unstable is determined as the flutter speed.

5.2.1.3 p-k method

The k method is useful in cases where the aerodynamic model is only obtainable in the reduced frequency domain for discrete values of k . However, a major disadvantage of this method is the artificially included damping. To handle this problem, Hassig [104] developed the $p - k$ method which combines the advantages of p method with the convenience of k method, as discussed ahead.

The $p-k$ method assumes that for lightly damped oscillations, the aerodynamic model developed for an undamped system is reasonably accurate. Therefore models built using methods like the DLM can be used with this method. The flutter equation however is not modified for the part representing structural dynamics, which is still expressed in Laplace domain. Therefore the $p-k$ method is essentially a hybrid of the p and k methods, where Eq. (5.13) is rewritten as

$$\left[\frac{V^2}{c^2} Mp^2 + K - \bar{q}A(ik) \right] \eta = 0; \quad (5.22)$$

In Eq. (5.22), the complex valued matrix $A(ik)$ is only valid at a specified reduced frequency k which is a function of the frequency of oscillations as well as airspeed. Since oscillation frequencies are not known a priori, the equation cannot be solved directly for p as done in the p method. An iterative procedure is therefore applied to solve for flutter boundary. The procedure is as follows.

1. Select a range of airspeeds $V := V_1, V_2, \dots, V_n$ over which the analysis needs to be conducted.
2. At the i^{th} airspeed V_i , fix an initial guess value for the oscillating frequency ω_{init} for the mode of interest. The initial reduced frequency can now be computed

as $k_{init} = c \frac{\omega_{init}}{V_i}$. At this airspeed, carry out following steps -

- (a) Obtain the aerodynamics matrix $A(ik_{init})$ at the initial reduced frequency and substitute it in Eq. (5.22).
 - (b) Solve for complex conjugate values of p , from which the damping (ζ_{new}) and new oscillation frequency (ω_{new}) of the mode of interest may be obtained.
 - (c) Compute the difference between ω_{new} and the initially assumed ω_{init} to check if the error falls within accepted threshold. If not, repeat steps 2-4 for ω_{new} as the assumed oscillating frequency.
 - (d) Repeat steps a-c until ω_{init} and ω_{new} converge within the error threshold. Note the value of the associated damping ratio ζ_{new} after convergence.
3. Move on to the next airspeed and repeat step 2. Store all values of damping ratios obtained in 2(d) above.

At the end of these iterations, we obtain the set of modal damping ratios associated with the set of airspeeds chosen. A V - ζ plot can again be used to estimate the flutter boundary. The p - k method is known to be close to the p method in predicting the damping of lightly damped modes close to the flutter boundary [104]. It therefore provides a more reliable estimate of the flutter boundary compared to the k method while using an aerodynamic model which is more conveniently obtained.

A common disadvantage of all three methods is their inability to predict system dynamics before the flutter boundary with any degree of accuracy. Specifically, the k and p - k methods predict the flutter boundary well, but the equations used in those methods do not accurately represent the system dynamics. Therefore no investigation is possible of the system prior to instability. This issue is overcome in the BFF vehicle analysis as discussed next.

5.2.2 BFF Vehicle Flutter Analysis

The previous subsection briefly discussed various methods for flutter analysis of linear aeroelastic systems. Although these methods work well for prediction of flutter boundary (where damping is zero), the solutions below the flutter speed do not represent true dynamics of the system. Also, it is not possible to obtain continuous time

domain models for simulation unless a continuous aerodynamic model in Laplace domain is used in Eq. (5.13). And finally, Eq. (5.13) is typically written for flutter mechanisms involving only structural modes. Rigid body modes may be included within the same equations under the special circumstances where nonlinear coupling between rigid and structural modes is absent.

For the BFF vehicle, equations of motion are developed within the mean axes framework, as described in Chapter 2, which finally result in linear dynamics equations given in Eqs. (2.45). Eqs. (2.45) contain rigid body dynamics as well and can be rewritten in the Laplace domain easily. As described in Chapter 3, the aerodynamic model is obtained using the DLM which provides models at discrete reduced frequencies. A rational function approximation then provides a continuous aerodynamic model which parametrically varies with airspeed. The aerodynamic model is of the form shown in Eq. (3.39) in Chapter 3. It should be noted that while comparing the BFF aerodynamic model to the flutter equation Eq. (5.13), some variables have the same meaning yet defined differently. Specifically, the normalized Laplace variable p in Eq. (5.13) is defined as $p := \frac{c}{\bar{v}}s$, while its counterpart s_k in the BFF aerodynamic model in Eq. (3.39) is defined as $s_k = \frac{c}{2\bar{v}}s$. The reduced frequency k is also defined accordingly. As mentioned before, the physical meaning and interpretation of these terms remains the same and these differences are only in scaling. Since the aerodynamic model is available as a rational function of the normalized Laplace variable s_k , flutter analysis may be carried out in a manner analogous to the p method.

Linear models are derived across a range of trim airspeeds between 5 and 25 m/s in the form of Eq. (5.12). Tracking the eigenmodes associated with first wing bending and short period for models across the airspeed grid, the flutter boundary is obtained. The variation of short period and first symmetric wing bending modes with respect to airspeed is shown in Fig. 5.3.

Fig. 5.3 is essentially a form of V-g plot where instead of only damping ratio, the real and imaginary parts of complex roots are plotted as airspeed varies. It is analogous to a root locus plot in this regard. From Fig. 5.3 we see that the first wing bending mode goes unstable between 23 and 24 m/s. A closer search between that interval gives the flutter speed to be 23.8 m/s. Thus, the flutter boundary for the BFF vehicle in straight and level flight is estimated to be 23.8 m/s.

Although it may appear that the method used for the BFF vehicle analysis is a version

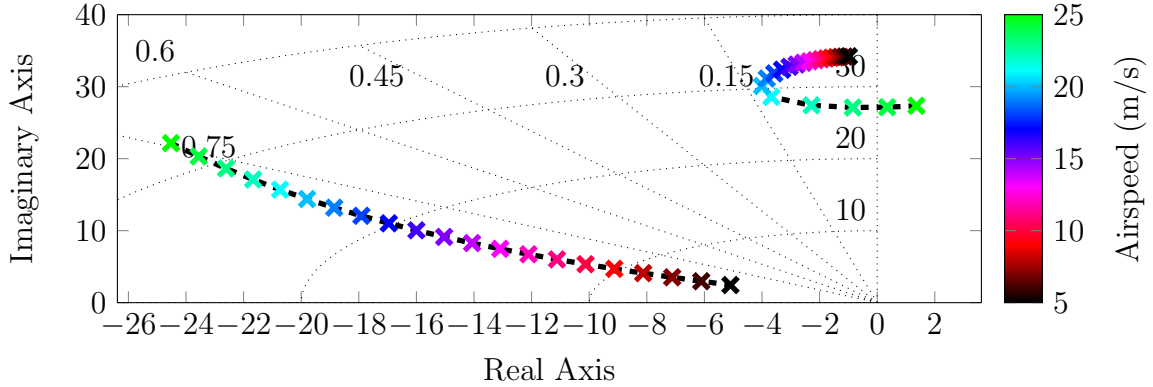


Figure 5.3: Short period and first symmetric wing bending modes variation with airspeed

of the p method, it needs to be remembered that the aerodynamic model obtained as a rational function is only actually valid at zero damping conditions where $s_k = ik$, as discussed in Chapter 3. Therefore, the BFF analysis is actually closer to the $p-k$ method where we assume zero damping for aerodynamics modeling and yet solve the flutter equation in Laplace domain. The rational function fitting actually only helps avoid the iterative process required to carry out frequency matching. In principle, the BFF flutter analysis may be considered a hybrid of the p and the $p-k$ methods.

This flutter boundary will be referred to as the nominal flutter boundary, since it is associated with the nominal model which has no uncertainties. Next, we will discuss the procedure for obtaining a robust flutter boundary with respect to the uncertain model constructed for the BFF vehicle in Chapter 4.

5.3 Robust Flutter Analysis

Flutter analysis described for the BFF vehicle in the previous section takes advantage of a continuous, linear Laplace domain model available due to a rational function fitted linear model for the aerodynamics and a linear finite element model for structural dynamics. However, these simplifications come at the cost of accuracy of the model. As noted in the previous chapter, modeling inaccuracies arise from errors in parametric values as well as systemic errors due to the modeling procedure itself. To account for these errors, uncertain models are constructed as described in the previous chapter.

In this section, we discuss the flutter analysis method applied to an uncertain aeroe-

lastic model using the structured singular value or μ . We first provide a mathematical description and overview of μ and then describe its use in computing robust flutter margins using an uncertain model. Finally, we look at the robust flutter analysis results for the BFF vehicle using the uncertain model constructed as described in the previous chapter.

5.3.1 Structured Singular Value

The structured singular value (μ) is essentially a measure of robustness of a linear, stable system with respect to specified uncertainties within it. Since an uncertain model is essentially a bounded family of models representing multiple possibilities corresponding to the uncertainties, μ helps determine the worst case stability characteristics for the family. In this subsection a brief mathematical background is provided on the definition and interpretation of μ . Detailed descriptions and derivations may be found in standard robust control textbooks [17,18]. .

For a mathematical description of μ , we begin with the linear fractional transformation (LFT) representation of a given uncertain model. An uncertain model can be partitioned into known and unknown parts and interconnected as shown in Fig. 4.1 in the previous chapter. The figure is reproduced here in Fig. 5.4. In Fig. 5.4, the

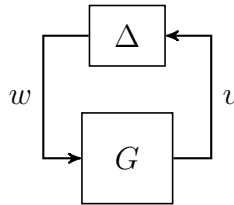


Figure 5.4: LFT feedback loop

Δ block represents the uncertainties specified for the model while G block contains the nominal model and additional terms associated with uncertainties. The interconnection can be better understood introducing input/output signals d and e and partitioning G into four parts as shown in Fig. 5.5.

In Fig. 5.5, G_{22} is the nominal model dynamics, G_{11} is the known dynamics associated with the uncertainties and the cross-diagonal terms represent the interacting dynamics between the model and the uncertainties. The uncertainty block Δ can be a general, complex valued full matrix. Such an uncertainty is usually specified to account for overall model uncertainties due to unmodeled dynamics, typically at high

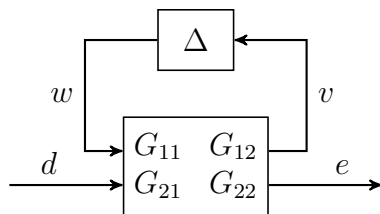


Figure 5.5: LFT feedback loop

frequencies. However, if the model is constructed by specifying uncertainties for each subsystem and model parameters as opposed to an overall specification, the block Δ is obtained as a specifically structured block diagonal matrix. Such a description is called structured uncertainty. For example, overall uncertainty for an uncertain model containing real parametric uncertainties as well as dynamic uncertainties for constituent subsystems can be expressed in terms of an uncertainty set Δ which can describe a structure as shown in Eq. (5.23)

$$\Delta = \{diag [\delta_1 I_{n_1} \quad \delta_2 I_{n_2} \quad \Delta_{m_1} \quad \Delta_{m_2}] : \delta_i \in \mathbb{R}, \Delta_j \in \mathbb{C}^j \times \mathbb{C}^j\} \quad (5.23)$$

where δ_i is a real parametric uncertainty repeated n_i times and Δ_j is a complex valued matrix of size (m_j, m_j) . Eq. (5.23) is an example of a convex uncertainty set Δ which describes the block diagonal structure of an *allowable* uncertainty. In this context, an allowable uncertainty is any norm bounded $\Delta \in \Delta$ (i.e. $\|\Delta\|_\infty \leq 1$). For convenience, the set of such uncertainties will be referred to in text simply as allowable uncertainties. Although bounds for different uncertainties may be specified independently, weighting functions are typically used to normalize the uncertainty variables as described in Chapter 4. Therefore, using suitable weighting functions, it can always be ensured that the overall uncertainty block is norm-bounded. Significantly tighter stability conditions may be derived by taking advantage of the structure of an uncertainty block as compared to the stability conditions for an unstructured one. Further details can be found in standard robust control books, see [17,18]. For a given nominal model and associated uncertainty specifications, structured uncertainty construction can be carried out conveniently using commercially available software like the robust control toolbox in MATLAB [80].

We now look at the robust stability condition for an uncertain model and the definition of μ following from it. For an uncertain system shown in Fig. 5.4, given both $G(s)$ and any allowable uncertainty $\Delta \in \Delta$ are internally stable, the closed loop is stable

for all allowed Δ if and only if

$$\det(I - G(i\omega)\Delta) \neq 0 \quad \forall \omega \forall \Delta \in \mathbf{\Delta}, \|\Delta\|_\infty \leq 1 \quad (5.24)$$

Equation (5.24) follows from the Nyquist stability theorem applied to a feedback system with a stable open loop transfer function [18]. Thus, system evaluated at a given frequency with an allowable uncertainty Δ remains stable as long as Eq. (5.24) is satisfied at that frequency. Based on this stability condition a measure of robustness μ is defined for a given frequency ω and any allowable uncertainty Δ as

$$\mu_\Delta(G(i\omega)) = \frac{1}{\min\{K \mid \det(I - G(i\omega)K\Delta) = 0, \bar{\sigma}(\Delta) \leq 1\}} \quad (5.25)$$

Eq. (5.25) shows that μ is defined as the inverse of the minimum scaling factor K for which $(I - GK\Delta)$ is singular at a given frequency ω , where Δ is norm-bounded. The norm boundedness of Δ can be achieved via suitable rescaling of G . The scaling factor K can be considered to be analogous to robustness margin of $G(i\omega)$ with respect to all allowable uncertainties at a given frequency ω . Using Eq. (5.25), a robust stability condition can now be written as

$$\mu_\Delta(G(i\omega)) < 1 \quad \forall \omega \forall \Delta \in \mathbf{\Delta}, \bar{\sigma}(\Delta) \leq 1 \quad (5.26)$$

It basically states that if the minimum scaling K required for the closed loop to become unstable is greater than unity for all frequencies, then the system is robustly stable for all norm bounded structured uncertainty $\Delta \in \mathbf{\Delta}$. Typically, Eq. (5.25) is computed on a frequency grid which is specified across a given frequency range of interest for the system at hand. The condition in Eq. (5.26) can then be checked at these frequency points for robust stability. For an aeroelastic model, a robust flutter boundary can thus be computed based on this robust stability condition.

5.3.2 Robust Flutter Analysis for BFF vehicle

Under straight and level flying conditions, robust flutter boundary can be considered as the smallest airspeed at which an uncertain aeroelastic system becomes unstable. Since model uncertainties are taken into account for stability analysis, the flutter

boundary computed is deemed robust to any modeling inaccuracies which fall within the uncertainty bounds specified. This can also be understood by recalling that an uncertain model is essentially a family of models. The robust flutter boundary refers to the flight condition at which at least one possible model within that family becomes unstable.

Stability analysis for an uncertain model can be carried out using μ , as described in the previous subsection. Chapter 4 describes the uncertainty specifications for structural dynamics and aerodynamics subsystems for the BFF vehicle. Both parametric and dynamic uncertainties are modeled in the two subsystems. An uncertain model suitable for μ analysis can be constructed using the state space model developed in section 1 by incorporating uncertainties as specified in Chapter 4.

For structural dynamics, uncertainty in modal mass and stiffness matrices can be constructed as shown in Eqs. (4.28) using uncertainty specifications from Table 4.2 in Chapter 4. These uncertainties can now be added to the modal mass and stiffness matrices used in the construction of state space matrix A and B shown in Eq. (5.4). Similarly, uncertainties specified for rigid body moments of inertia can be directly incorporated into the state space model as parametric uncertainties.

Parametric uncertainties in steady aerodynamics stability derivatives and dynamic uncertainty in unsteady aerodynamics are incorporated into the GAM matrix $Q(s_k)$ as described in the previous chapter. Uncertain aerodynamics can now be incorporated into the BFF state space model in a similar manner as the nominal aerodynamics in Eq. (5.4). The main difference is that the state space matrices for the aerodynamic model in Eq. (5.3) are now uncertain matrices. In practice, Matlab has several functionalities that allow for a direct integration of the uncertain aerodynamics matrix in Laplace domain with the state space dynamics model, thus avoiding the need for explicit computations shown in Eq. (5.4). The uncertain model is built in Matlab using the Robust Control Toolbox [80].

The overall uncertain model of the BFF vehicle is now partitioned into its known and unknown constituents which can be connected to each other in the form of an LFT interconnection. Since the uncertainties have been specified for individual parameters and subsystems, the overall uncertainty can be constructed as a structured one. Therefore, the resulting overall structured uncertainty block can be written as

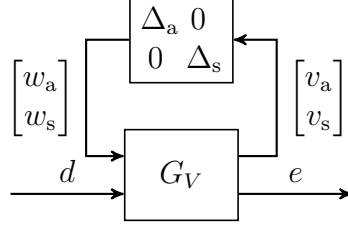


Figure 5.6: Aeroelastic model with Structured Uncertainty

where Δ_s represents a block diagonal structure consisting of structural parametric uncertainties while Δ_a corresponds to the aerodynamic parametric and dynamic uncertainties. G_V contains the entire aeroelastic model along with the uncertainty interaction terms shown in Fig. 5.5. The subscript V indicates that the state space model is obtained at trim airspeed V . For robust stability analysis, we obtain linear models for a range of airspeeds and carry out a point-wise analysis at each airspeed.

Using Eq. (5.26), a robust flutter boundary can be computed as the trim airspeed V_{rfb} at which the maximum occurring $\mu_{\Delta} G_V(i\omega)$ across a specified frequency range is equal to unity. Thus, for a given set of block structured uncertainties Δ , V_{rfb} is defined as the smallest airspeed V such that

$$\max_{\omega \in \Omega} \mu_{\Delta} G_V(i\omega) = 1 \quad (5.27)$$

Here Ω represents the frequency grid specified across the desired frequency range for the analysis. The frequency grid can be specified based on prior knowledge of the frequency at which instability is expected to occur, usually based on the results obtained from nominal flutter analysis. The range of airspeeds is similarly chosen. For accurate results in terms of the exact frequency and airspeed associated with instability, the frequency and airspeed grid has to be fairly dense. However, it is computationally expensive to have a dense grid of both frequencies and airspeeds. Therefore, a graphical approach is proposed to reduce the computational burden. V_{rfb} can be obtained graphically as described ahead.

For a given frequency grid Ω and airspeed V , compute instability scaling factor \bar{K} as

$$\bar{K} = \frac{1}{\max_{\omega \in \Omega} \mu_{\Delta}(G_V(i\omega))} \quad (5.28)$$

Note that \bar{K} is simply the inverse of the value of maximum $\mu_{\Delta}(G_V)$ occurring over Ω

at a given airspeed. \bar{K} can be computed over a relatively coarse grid of airspeeds and plotted on a $\bar{K} - V$ graph. From Eq. (5.27) it can be seen that the point where this plot intersects $\bar{K} = 1$ line on the graph corresponds to the robust flutter boundary.

For the BFF vehicle, the $\bar{K} - V$ graph is plotted for the uncertain system described above, constructed across a range of velocities from 17.5 m/s to 23.5 m/s. A frequency grid of 200 points is chosen between 10 and 65 rad/s at each airspeed for the analysis, which is found to be sufficiently dense via a few iterations. The $\bar{K} - V$ graph obtained for the BFF vehicle is shown in Fig. 5.7. From Fig. 5.7, it can be seen that the airspeed

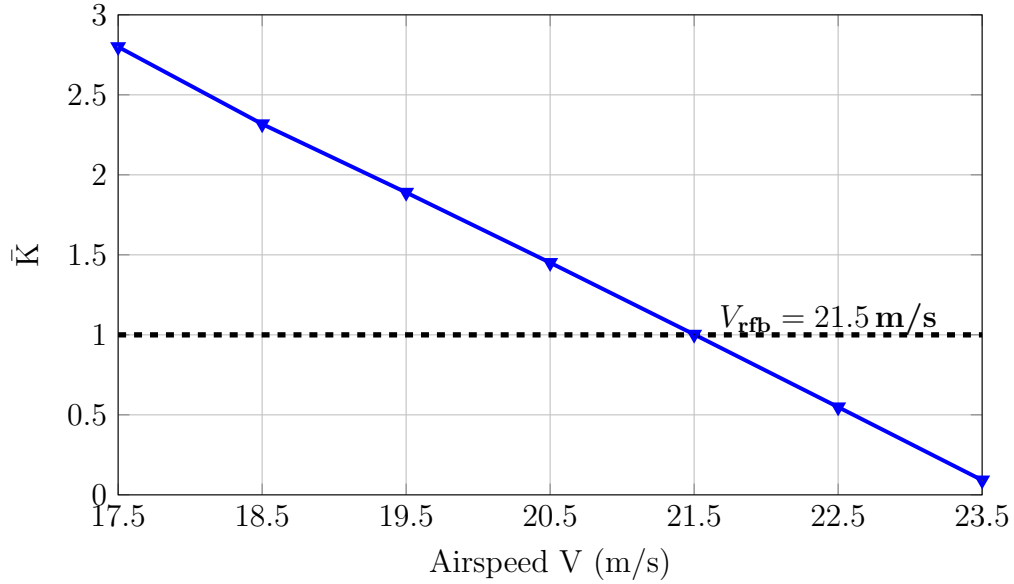


Figure 5.7: $\bar{K} - V$ graph for the BFF vehicle

associated with robust flutter boundary is $V_{\text{rfb}} = 21.5$ m/s. Thus, the uncertainties specified for the model push the flutter boundary from a nominal value of 23.8 m/s obtained in the previous section down by more than 3 m/s. In other words, stability cannot be guaranteed above 21.5 m/s due to possible modeling inaccuracies. Also, as \bar{K} approaches zero on the right end of the Fig. 5.7, it will intersect the x axis at the nominal flutter speed of the system. This is because at the nominal flutter speed, the system would be unstable at flutter frequency even if Δ is set to zero i.e. zero uncertainty. Therefore the corresponding value for $\mu_{\Delta}(G_V)$ would be infinite at the flutter frequency (which means $\bar{K} = 0$). Therefore by graphically extrapolating the $\bar{K} - V$ graph, nominal flutter speed can be estimated in an alternate manner.

The $\bar{K} - V$ graph has been developed as the primary tool for computing robust flutter

boundary in this analysis. Although we can just as easily plot the maximum $\mu_{\Delta}(G_V)$ instead of its inverse, $\bar{K}-V$ graph is more intuitive to work with in terms of robustness since \bar{K} is analogous to robustness margin. It is easy to see how much scaling of the uncertainty would make the aeroelastic system unstable at any given airspeed. For example, if accuracy of the modeling procedure were to be improved so as to reduce all uncertainty bounds down to 50% of their original values, the robust flutter boundary then rises up to be approximately 22.6 m/s corresponding to $\bar{K} = 0.5$ in Fig 5.7.

However, it is often not feasible or desired to improve all aspects of the modeling procedures. It is much more useful to analyze specifically which individual aspects of the model can be improved in accuracy for maximum gains in terms of predicted robust flutter boundary. this can be achieved by carrying out a sensitivity analysis, which determines which uncertainties affect the robust flutter boundary the most. The next section describes sensitivity analysis based on the robust flutter boundary computation framework outlined in this chapter.

5.4 Sensitivity Analysis

In the previous section, a method for robust flutter analysis was developed within the framework of robust control theory using the structure singular value μ . The analysis is carried out for an uncertain aeroelastic model consisting of both parametric and nonparametric uncertainties. One of the important advantages of such an approach is the ability to interpret model uncertainties in a physical sense. In addition to estimating robust flutter boundary, the analysis also enables us to know the exact parameters and subsystems to which the boundary is robust. Since the flutter boundary depends on the size of the uncertainty bounds specified in the model, it is important to ensure that the bounds are not too conservative. An important question which arises with regards to all the uncertainties specified is - how does variation in the bounds of each of the uncertainties affect the flutter boundary. In other words, how sensitive is the flutter boundary to each of the uncertainties specified in the model.

Sensitivity analysis is an important part of model development and analysis for complex engineering systems. Several methods have been developed and studied over the years which cater to different types of models. For example, it is possible to have statistical models which are analyzed using probabilistic methods [110, 111] or analytical models which may use differential analysis or perturbation based meth-

ods [111, 112]. There are two distinct approaches in which a sensitivity analysis may be carried out and the results interpreted [111–114]. In the first approach, effect of variation in parameters of a model on its outputs is analyzed. The ones which affect the output the most are called *sensitive* parameters. The second approach deals with the variation in specified uncertainty of parameters and the resulting change in the outputs or uncertainty of the outputs. Here, we are primarily interested in how a model responds to a change, not in parametric values, but in the confidence we have in those values. Parameters whose change in uncertainties affect output uncertainties the most are called *important* parameters. The distinction between the two is subtle and lies essentially in their interpretation. Important parameters are sensitive by default, since a change in their uncertainties can only reflect in the outputs if the model is sensitive to them. However, a sensitive parameter may not be important if, for instance, its value is known with high degree of accuracy. Therefore, analyses which determine the important parameters give a richer insight into the model.

In this section, we develop an approach for systematic sensitivity analysis for an uncertain aeroelastic model with structured uncertainty. The objective is to study the effect of variation in uncertainty bounds in the model on the flutter boundary computed. Therefore it may be seen as an analysis to identify the important parameters of the model. However, it is the flutter boundary whose variation is to be observed, which is a quantity associated with stability of the model and not its output. The results from this analysis give significant insights into the effect of model uncertainties on robustness analysis. It helps determine which parameters or subsystems need to be modeled more accurately to reduce the conservativeness of the flutter boundary. Conversely, we can also determine the parts of the model that need not have any uncertainty specifications since those uncertainties do not affect the robustness analysis much.

5.4.1 Approach for Sensitivity Analysis

For sensitivity analysis, the uncertain model of the BFF vehicle constructed using specifications from Chapter 4 is considered as the baseline uncertain model. A sensitivity scaling parameter is defined for each of the specified uncertainties, which varies from 0.5 to 2. This parameter gets multiplied to the weights associated with all uncertainty bounds. The baseline uncertain model can now be obtained by setting the value of all scaling parameters as 1. As the sensitivity scaling parameter for a par-

ticular uncertainty varies within its specified range, it scales the uncertainty bound between 50% and 200% of its baseline value. By carrying out robust stability analysis as a particular scaling parameter is varied, the effect of its corresponding uncertainty bound on the flutter boundary can be studied. For instance, for uncertainty associated with bending stiffness parameter (Young’s modulus, E), the sensitivity scaling parameter is incorporated as shown in Eq. (5.29)

$$E_{\text{unc}} = E_{\text{nom}} k_{\text{Esens}} W_E \Delta_E \quad (5.29)$$

E_{nom} represents the nominal value of Young’s modulus of the material used in the wing spar, Δ_E is a norm bounded real valued uncertainty, W_E is the baseline bound and k_{Esens} is the sensitivity scaling parameter. The baseline bounds are set as shown in Table 4.2. A new uncertain model for the BFF aircraft can be constructed based on uncertainty descriptions which include sensitivity scaling parameters. Sensitivity of the robust flutter boundary to individual uncertainty bounds can then be obtained by varying the bounds using the scaling parameters, one scaling parameter at a time. The range of variation for all the scaling parameters is kept the same, between 0.5 and 2. A step-by-step procedure for carrying out this analysis is given below.

1. Select a model parameter/subsystem for which uncertainty bounds are specified. Set sensitivity scaling parameter to 0.5.
2. Plot the $\bar{K}-V$ graph for the uncertain model, obtain the robust flutter boundary.
3. Repeat step 2 for all scaling parameter values between 0.5 and 2. Plot the corresponding $\bar{K}-V$ graphs and note the flutter boundary values.
4. Repeat steps 2 and 3 for all parameters/subsystems in the model.

We obtain an overall $\bar{K}-V$ graph for each parameter or subsystem which portrays the variation of its scaling parameter. As an example, the bending stiffness sensitivity scaling parameter k_{Esens} is scaled between 0.5 and 2 and the $\bar{K}-V$ graph is plotted for the uncertain model obtained for each scaled value as shown in Fig. 5.8.

Each line in Fig. 5.8 corresponds to the $\bar{K}-V$ plot for an uncertain model constructed using a different value of k_{Esens} ranging from 0.5 to 2. Consequently, the airspeed at which each line intersects the $\bar{K} = 1$ line represents the flutter boundary associated

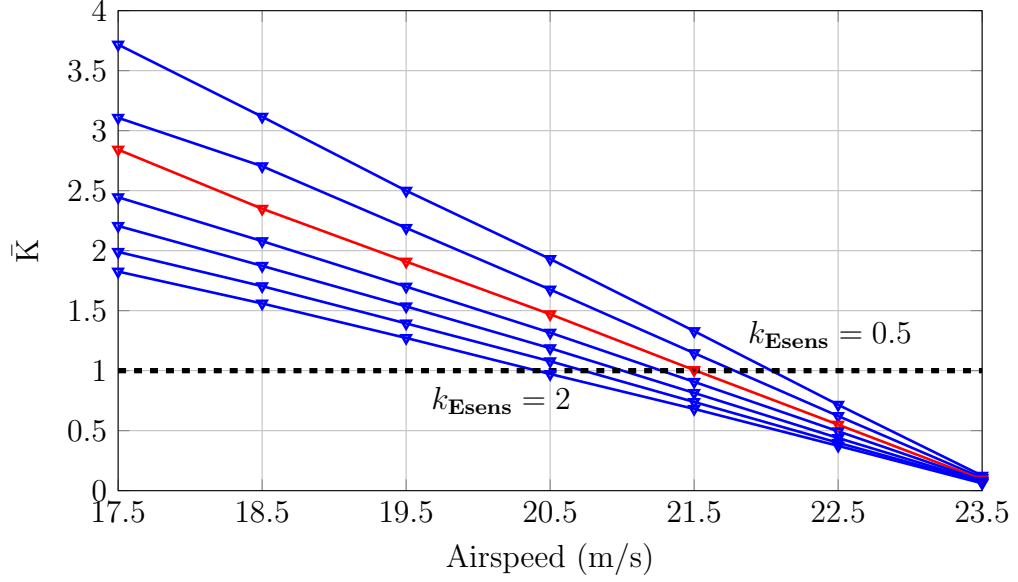


Figure 5.8: $\bar{K} - V$ graph variation in uncertainty for structural bending stiffness, baseline uncertainty given by (\blacktriangledown)

with the corresponding value of k_{Esens} . For example, the flutter boundary of an uncertain model in which $k_{\text{Esens}} = 2$ is approximately 18.5 m/s. On the other hand, the flutter boundary associated with $k_{\text{Esens}} = 1$, which represents the baseline uncertain model, is 20 m/s as obtained in the previous chapter as well.

It should be noted that \bar{K} refers to the scaling of the overall structured uncertainty Δ required for model instability, whereas k_{Esens} refers to the individual scaling of uncertainty Δ_E . We see in Fig. 5.8 that with increase in k_{Esens} , the robust flutter boundary V_{rfb} decreases. This is to be expected, since scaling up the bounds of one uncertainty makes the overall model more conservative. Graphs such as Fig. 5.8 can be plotted for each uncertainty specification. The next section describes the results for sensitivity analysis carried out for the BFF vehicle using $\bar{K} - V$ graphs similar to the one shown in Fig. 5.8.

5.4.2 Results & Discussion of Sensitivity Analysis

To compare sensitivity of the flutter boundary to different uncertainties, it is necessary to quantify the rate at which the flutter speed varies with respect to change in the uncertainty bounds. $\bar{K} - V$ graphs such as the one shown in Fig. 5.8 show this variation visually for an individual uncertainty. Sensitivity can be quantified via a sensitivity graph in which the flutter speed V_{rfb} corresponding to each line of the $\bar{K} - V$ graph is

plotted against the respective value of the sensitivity parameter. For example, based on Fig. 5.8, the sensitivity graph for bending stiffness uncertainty can be obtained as shown in Fig. 5.9.

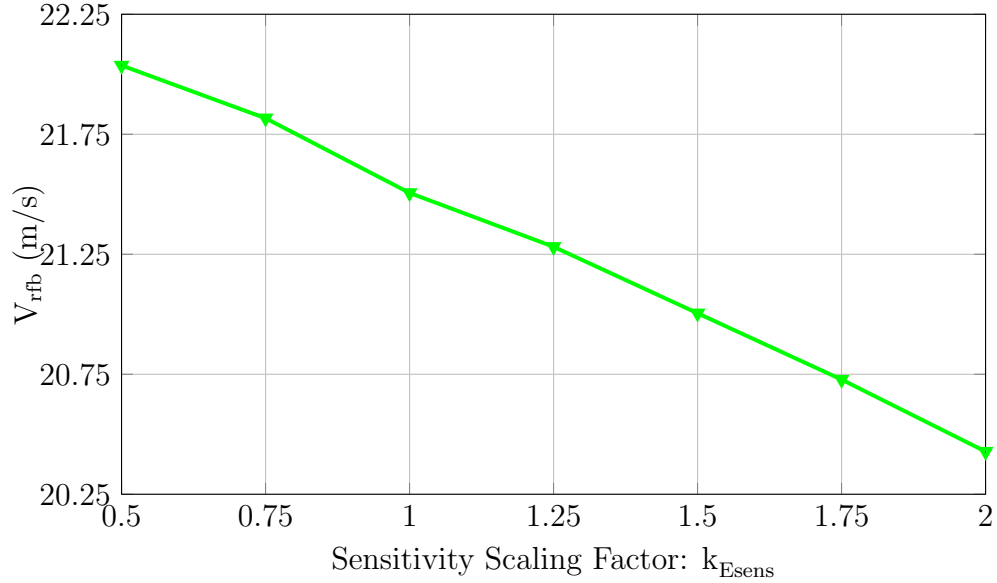


Figure 5.9: Sensitivity Plot showing variation of robust flutter boundary with change in bending stiffness uncertainty bound

The same process can be used for other uncertainties associated with pitch moment of inertia, location of C.G., steady and unsteady aerodynamics. From the $\bar{K} - V$ graphs associated with all uncertainties, we can pull out the variation of flutter speeds with their corresponding sensitivity scaling factors. A sensitivity graph can then be plotted which shows this variation for each uncertainty as shown in Fig. 5.10. Fig. 5.10 shows how the robust flutter boundary varies as each uncertainty is scaled individually. Since all the scalings are between 0.5 and 2, all the variations can be plotted and compared on a single graph. Fig. 5.10 provides insight into the relative sensitivities of different uncertainties. The plots all intersect at the baseline uncertainty where all sensitivity scalings are unity. This point represents the baseline robust flutter boundary $V_{r_{fb}} = 21.5 \text{ m/s}$. The results and conclusions obtained from the sensitivity graph shown in Fig. 5.10 is discussed in detail in the following section.

The sensitivity graph for the uncertain model representing the BFF vehicle is obtained as shown in Fig. 5.10. It shows the variation of robust flutter boundary as different uncertainty bounds are varied one at a time. From Fig. 5.10 we see that $V_{r_{fb}}$ is most sensitive to the bounds on structural bending stiffness. This is followed by

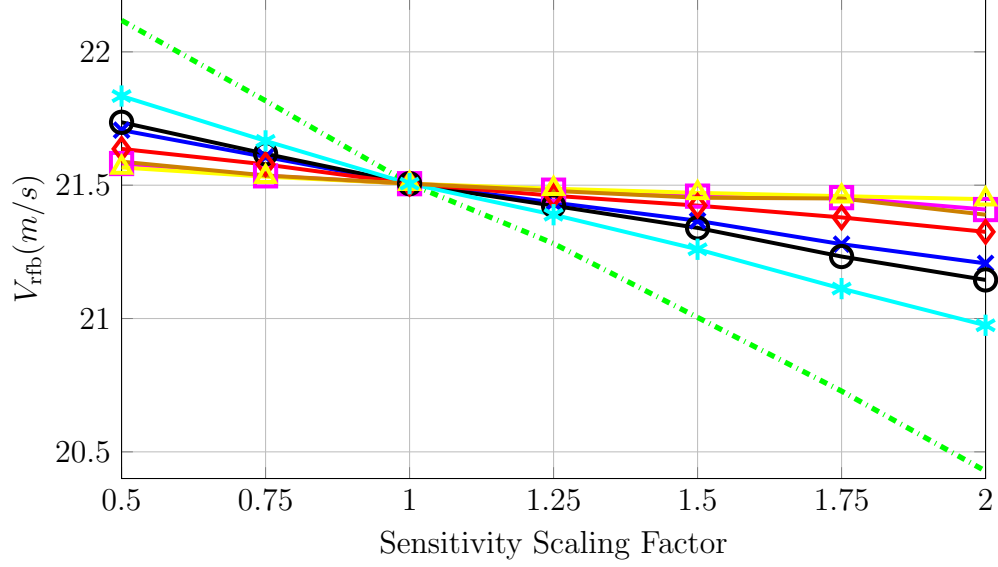


Figure 5.10: Sensitivity plot for BFF uncertain model. The lines represent steady lift coeff: (\blacklozenge), steady pitch coeff: (\blacktriangle), unsteady aerodynamics: (\blacksquare), Pitch moment of inertia: (\blacklozenge), Bending stiffness: ($\text{---}\text{---}$), Torsional Stiffness (\blacklozenge), C.G. location (\blacklozenge) and mass distribution (\blacklozenge)

the dynamic uncertainty due to C.G. variation and torsional stiffness. However, the flutter boundary seems to be highly unaffected by uncertainty bounds of either steady aerodynamics lift or pitch coefficient and only marginally affected by variation in the bounds of mass distribution. It should be remembered that the sensitivities referred to here are with respect to uncertainty bounds of various parameters and not the parameters themselves. The slope values are listed in Table 5.1.

Table 5.1: Slopes of the Sensitivity Plot for different Uncertainties

Uncertainty	Source	Slope
Δ_E	Bending Stiffness	-1.13
Δ_{cg}	C.G. Location	-0.57
Δ_{md}	Wing Mass Dist.	-0.39
Δ_G	Torsional Stiffness	-0.33
Δ_{C_L}	Steady Lift Coeff	-0.21
$\Delta_{I_{yy}}$	Pitching Mom. of Inertia	-0.13
Δ_{dyn}	Unsteady Aerodynamics	-0.12
Δ_{C_M}	Pitching Mom. Coeff	-0.079

From Table 5.1 we see that sensitivity to bending stiffness is more than 14 times the sensitivity to aerodynamic pitching moment coefficient uncertainty which is the

lowest. It should be noted that these results depend on the baseline bounds assumed for each uncertainty since the scaling is based on the size of the baseline bounds. For instance, the baseline bound for pitching moment coefficient C_M is assumed to be $\pm 5\%$, which is consequently scaled by a factor of 0.5 to 2. Therefore in absolute terms, the bound is varied from $\pm 3\%$ to $\pm 10\%$. However, if the baseline bound is assumed at, say, $\pm 50\%$, then the same scaling range results in the bound varying from $\pm 30\%$ to $\pm 100\%$ in the absolute sense. This leads to a greater drop in robust flutter boundary for the same scaling. Hence, for this sensitivity analysis to be relevant, baseline bounds have to be selected carefully.

The flutter boundary is most sensitive to variation in bending stiffness uncertainty. Considering the flutter mechanism which involves the first wing bending mode coupling with the short period mode, this result not unexpected. The baseline uncertainty in bending stiffness was determined on the basis of differences and deviations (with respect to theoretical estimate) in experimental data from ground tests. Therefore, if the bounds are tightened via better experimental measurements of the Young's modulus, we can achieve a robust flutter boundary closer to the nominal boundary more effectively compared to similar improvements in other uncertain parameters. Conversely, a poor experimental accuracy can cause V_{rfb} to drop rapidly since the baseline bound itself increases.

Variation of uncertainty in the location of center of gravity has a significant impact on V_{rfb} , which is second only to the bending stiffness. However, the experimental measurement for this parameter is very accurate [15]. Even the baseline uncertainty assumed has very large bounds, thus contributing to the high sensitivity. Therefore, this analysis may not be directly relevant to the BFF vehicle. However, in an aircraft with varying C.G. location (typically due to fuel burn), the model may not be able to predict the location as accurately as ground tests. The X-56A MUTT vehicle is a good example of this. In such a situation, it becomes very important to keep the modeling error low since the analysis reveals high sensitivity to C.G. location.

The third most important parameter in Table 5.1 is the mass distribution, which was included to account for variations in mode shapes obtained from GVT data. The mass distribution is essentially assumed constant along the wing, and the parameter affects the first wing bending dynamics. As mentioned earlier in Chapter 4, uncertainty in this parameter mainly arises from change in the composition of the wing due to

replacement of electronics, repairs to damages and general replacement of parts due to wear and tear. The sensitivity analysis reveals that unforeseen changes in mass distribution affect flutter boundary computation more than other aspects of the model such as aerodynamics (steady or unsteady) and pitching moment of inertia. Therefore it is important to take steps to minimize this uncertainty via careful logging of all changes to mass distribution in the vehicle.

An important insight gained from this analysis is the importance of the torsional stiffness parameter G which, unlike bending stiffness, mass distribution or C.G. placement, is assumed not to influence the BFF mode. Even though sensitivity of the flutter boundary to G is around a third of the value corresponding to bending stiffness parameter E , it is a relatively high compared to aerodynamics or the pitching moment of inertia. This is possibly because the BFF mode is not completely independent of the twist in the wings. The first wing bending motion dominates the BFF mode, but due to the sweep back design of the aircraft, the mode also shows significant amount of wing twist. Therefore, we see a considerable amount of influence of the wing torsional stiffness on the BFF mode and consequently, the flutter boundary.

Within the aerodynamics model, uncertainty in steady aerodynamics lift coefficient has the maximum effect on the computed flutter boundary. Since the lift coefficient is computed and compared using multiple methods including wind tunnel tests, the baseline uncertainty assumed for it is reasonable. On the other hand, although the flutter boundary is less sensitive to unsteady aerodynamics, it is the only part of the BFF vehicle model which is obtained purely from a *single* theoretical approach. Although the DLM itself has been validated against experimental data [55], there is no experimental data to either validate the unsteady aerodynamics model for this aircraft or to provide any meaningful bounds on it. As discussed in Chapter 4, the baseline error bounds are specified based on fitting errors only, although there could potentially be significant discrepancy at the baseline level itself. Thus, given the fact that the model is not verified or bounded via experimental data, it serves as one of the most important areas for further investigation.

The uncertainties associated with steady aerodynamics pitching moment as well as pitch moment of inertia seem to have little affect on flutter boundary prediction. Even reducing their uncertainty to half the specified value does not result in any improvement in the conservativeness of the predicted flutter boundary. Therefore the

current levels of accuracy in the experiments conducted or theory used for obtaining these parameters can be considered sufficient.

An important application of the results obtained from this analysis is in the area of model updating based on flight test data. It can be envisioned that in any future flight tests, if the experimental data (including the flutter boundary) do not fall within the scope of the corresponding uncertain model, the uncertainty bounds will have to be re-examined. These analyses will enable a least conservative updated uncertain model which effectively represent any variations of flight data, since it will be known a priori which sources of uncertainties are the most influential for stability and performance of the aeroelastic system.

5.5 Summary

In this chapter, we describe the process for constructing a state space model for the BFF vehicle at a given flight condition. The model is then used for nominal flutter analysis which provides the flutter boundary for the BFF vehicle. Classical flutter analysis techniques such as the p , k and $p - k$ method are reviewed and the method used for BFF vehicle is compared with them for a better perspective on the assumptions involved within the method as well as its limitations.

Uncertain models for the BFF vehicle are constructed for carrying out robust flutter analysis. Robust flutter boundary is computed via μ based mathematical tool called the $\bar{K} - V$ graph, which tracks the variation in robust flutter margin as a function of airspeed. The graphical approach helps avoid μ computations at a large number of airspeeds. Finally, sensitivity analysis for the robust flutter boundary is described. The analysis is based on the same graphical tools and is carried out to study the effect of the variation in bounds of each individual uncertainty specification. The sensitivity of the robust flutter boundary towards bounds of different uncertainty specifications can be studied using the sensitivity graph. The chapter provides a detailed interpretation of the results obtained from the analysis.

Chapter 6

Closed Loop Analysis

In the previous chapter, the variation of flutter boundary with respect to individual uncertainty bounds was examined. The objective of that analysis was to determine which uncertainties affected the estimated flutter boundary the most. In this chapter, we look at the effect of variation in individual uncertainty bounds on the flutter boundary for a system closed in loop with a baseline flutter suppression controller. The objective of this analysis is to identify the model uncertainties which are important from the control design point of view.

Flutter suppression is a common control design objective in the field of aeroservoelasticity. A flutter suppression controller is usually designed to provide increased damping and thereby stabilize a single mode of interest without affecting the open loop dynamics at other frequencies. This enables an aircraft such as the BFF vehicle to fly beyond its open loop flutter boundary while retaining its low frequency dynamics such as the rigid body modes, which may either be controlled by another controller in the loop or a human pilot. Thus, the flutter suppression controller helps extend the flight envelope of the aircraft. The aircraft model used for controller synthesis plays a vital role in determining the effectiveness of the controller in flight.

Typically, linear controllers are designed using aircraft models linearized at a given flight condition of interest. To keep the design procedures simple and final controller order low, nominal models are preferred for the synthesis. In such cases, it is important to analyze the degradation of closed loop performance in presence of model uncertainties. Also, it is fruitful to study how each individual uncertainty specifi-

cation affects the controller performance in terms of expanding the flight envelope. A flutter suppression controller in the loop significantly alters the dynamics of the closed loop system, since only certain modes are damped. Therefore, it is possible that in the closed loop system, parameters associated with undamped modes affect the flutter boundary more significantly. Hence, the analysis described in this chapter is critical for gaining useful insights into the affect of a controller in the loop on the sensitivity associated with different model parameters.

We can use the analysis tools developed in the previous chapter to study the sensitivity of closed loop performance of a given controller to individual uncertainty bounds. The aircraft model used for control law synthesis is based on the nominal aeroelastic state space model developed for the BFF vehicle in Chapter 5. We design a \mathcal{H}_∞ controller based on work previously done by Theis et al in [115]. The control design in [115], carried out at the University of Minnesota, focuses on active flutter suppression of the mini-MUTT aircraft which was built at the Unmanned Aerial Vehicles laboratory at the university [5,12]. The design of the mini-MUTT is based on the BFF vehicle, with the primary difference being that the mini-MUTT was designed to be much stiffer. As a result, as seen in [115], the flutter boundary of the mini-MUTT is at a much higher airspeed. To adapt to the BFF vehicle, the controller is re-tuned for control action in the desired frequency range.

The control synthesis model, which includes added dynamics due to actuators and sensors, is described in the following section 1. The baseline control design is briefly described next, along with nominal and robust closed loop flutter analysis in section 2. Finally, sensitivity analysis is carried out for each individual uncertainty specification in section 3.

6.1 Aircraft Model for Synthesis

The BFF state space model developed in the previous chapter is the basis for developing the synthesis model. The state space matrices are developed using Eqs. (5.4),

(5.11) and Eq. (5.12). The state space model is rewritten below for convenience.

$$\begin{bmatrix} \dot{\eta} \\ \ddot{\eta} \\ \dot{\eta}_{aero} \end{bmatrix} = A \begin{bmatrix} \eta \\ \dot{\eta} \\ \eta_{aero} \end{bmatrix} + Bu \quad (6.1a)$$

$$\begin{bmatrix} y_q^c \\ y_{accels} \end{bmatrix} = C \begin{bmatrix} \eta \\ \dot{\eta} \\ \eta_{aero} \end{bmatrix} + Du \quad (6.1b)$$

As noted in the previous chapter, in Eqs. (6.1) the states are $\eta = [\eta_r \ \eta_f]$ where η_r is the set of rigid body positions and η_f represent the modal deflections. Also, η_{aero} represent the aerodynamic lag states. It should be noted that the dependence of the state space matrices on airspeed V are not included in the notation in Eqs. (6.1) for brevity.

For control design, the state space model is modified to include the first wing bending modal velocity $\dot{\eta}_1$ as a performance output. A performance output, as opposed to a measurable output, is not a part of the feedback signals to the controller. The output is mainly used to enforce performance specifications, as we shall see later. The C and D matrices are modified to include this output as follows -

$$C_{\eta_1} = \begin{bmatrix} \underbrace{0 \ \dots \ 0}_{6+n_f+6} \ 1 \ \underbrace{0 \ \dots \ 0}_{n_f-1+n_{aero}} \end{bmatrix} \quad (6.2a)$$

$$C_{syn} = \begin{bmatrix} C_{\eta_1}^T & C^T \end{bmatrix}^T \quad (6.2b)$$

$$D_{syn} = \begin{bmatrix} 0 & D^T \end{bmatrix}^T \quad (6.2c)$$

where n_f and n_{aero} represent the number of modal states and aerodynamic lag states respectively. In order to keep the controller generated inputs decoupled from any external pilot inputs to the elevator and aileron, the controller is restricted to use only outboard flaps for flutter suppression. Therefore, the input vector u is modified to contain only outboard flap deflections and the corresponding columns in B and D_{syn} matrices are retained in the model. Furthermore, the controller is also restricted to generate purely symmetric deflections, thereby effectively generating a single control input signal which is fed to both the outboard flaps.

We also seek to reduce the number outputs required for feedback to keep the design

simple. Since the mode of interest is the BFF mode which involves rigid short period dynamics and first symmetric wing bending modes, the accelerometer outputs are *blended*. The four wing tip accelerometer outputs are averaged to obtain a single representative output for wing tip accelerations, while the two center body accelerometer outputs are averaged as well. This is done by pre-multiplying C and D matrices in Eq. (6.1) with a suitable matrix as follows -

$$C_{blend} = \begin{bmatrix} 1 & 0 & 0 & 0 & 0 & 0 & 0 \\ 0 & 0.5 & 0.5 & 0 & 0 & 0 & 0 \\ 0 & 0 & 0 & 0.25 & 0.25 & 0.25 & 0.25 \end{bmatrix} C_{syn} \quad (6.3a)$$

$$D_{blend} = \begin{bmatrix} 1 & 0 & 0 & 0 & 0 & 0 & 0 \\ 0 & 0.5 & 0.5 & 0 & 0 & 0 & 0 \\ 0 & 0 & 0 & 0.25 & 0.25 & 0.25 & 0.25 \end{bmatrix} D_{syn} \quad (6.3b)$$

C_{blend} and D_{blend} can now be used instead of C and D matrices in Eq. (6.1) to obtain the desired BFF model for synthesis.

The synthesis model needs to have a low number of states for a low order controller design. Due to aerodynamic lag states introduced by the DLM, number of states in the BFF model described above is of order 100 which is not acceptable for \mathcal{H}_∞ control design. Therefore, model order reduction needs to be carried out to proceed with control design. The next subsection provides details of the model reduction process used.

6.1.1 Model Order Reduction

The BFF model obtained in Eq. (6.1) after updating the output matrices consists of 12 rigid body states $(\eta_r, \dot{\eta}_r)$, 24 structural states $(\eta_f, \dot{\eta}_f)$ and 130 aerodynamic lag states (η_{aero}) . The first step for reducing the order is to truncate the lateral-directional rigid body states which do not play any role in the dynamics of body freedom flutter. Therefore bank angle ϕ , heading angle ψ , roll rate p , and yaw rate r are truncated. Surge position x and the corresponding velocity u are truncated as well.

Next, out of the 24 structural states that include 12 modal deflections and the corresponding velocities, the states associated with the first and second modes are retained and all others are residualized. Residualization, as opposed to truncation, ensures that the contribution of higher frequency states towards low frequency dy-

namics is retained. Further reduction is carried out after transforming the model into its balanced realization.

A balanced realization results in a model to have equal controllability and observability gramians that are diagonalized [18, 116]. The diagonal entries in the gramians are the Hankel singular values of the system. A balanced realization essentially transforms the model and arranges the transformed states in the order of their influence on input-output behavior of the model. The controllability and observability of each state is exactly the same, and its measure is given by the corresponding Hankel singular value. A Balanced truncation would then involve removing the states corresponding to Hankel values lesser than a fixed minimum value.

Normally, balanced realization can only be carried out for asymptotically stable systems. In this case however, since we need to reduce the order of a system that has a known instability (the BFF mode), an alternate approach is used to carry out the realization. The model is partitioned into stable and anti-stable parts, and the stable part is balanced in an isolated manner [116]. The unstable part of the model is then added back to the balanced stable part. For further details, the reader is referred to the standard publications by Glover [116] and Enns [117]. It should be noted that Matlab provides functionalities which carry out this procedure for balanced realization of unstable systems.

Using balanced realization of the BFF model, all the states beyond the first 30 states are truncated. Of the remaining 30, all the states beyond the first 12 are residualized. This leaves us with a state space model with 12 states which can be conveniently used for control design. The final reduced order state space matrices for the BFF vehicle are provided in Appendix A.3 for reference. In order to compare the dynamics of the reduced order model with the full order model, the frequency response from elevator to pitch rate for both the models is shown below.

Next, the model is supplemented with additional parasitic dynamics to account for actuator and sensor dynamics as well as internal hardware delays. The next subsection describes the parasitic dynamics added to obtain the final synthesis model.

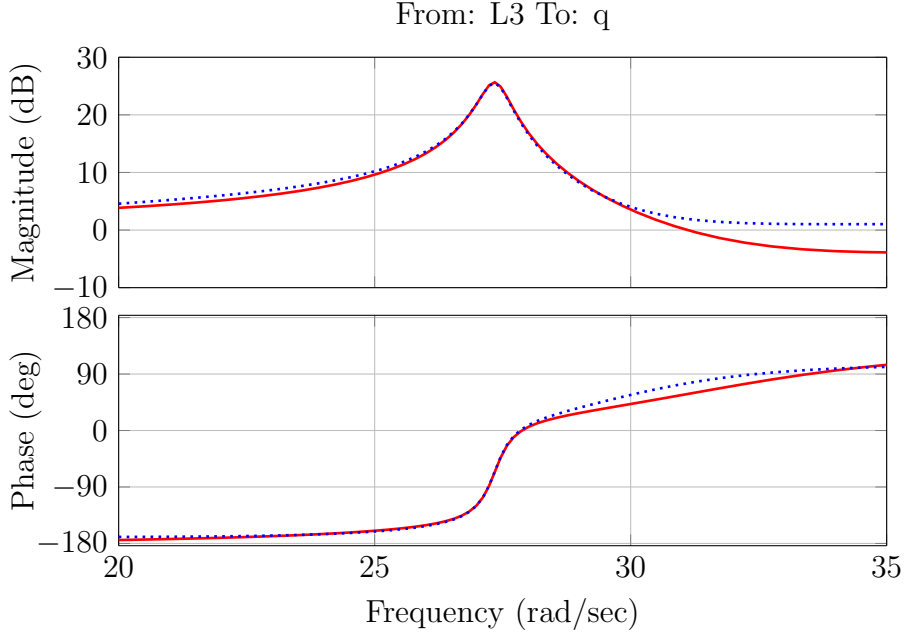


Figure 6.1: Reduced order model (— comparison with full order model (.....))

6.1.2 Parasitic Dynamics

The reduced order model obtained in the previous subsection is augmented with additional parasitic dynamics due to actuators and sensors to capture any phase loss due to them [115]. The actuator model is a second order linear system expressed in transfer function form as

$$G_{act}(s) = \frac{96710}{s^2 + 840s + 96710} \quad (6.4)$$

The sensor model, which is assumed common for the accelerometers as well as the IMU, is a first order linear model expressed as

$$G_{sens}(s) = \frac{70\pi}{s + 70\pi} \quad (6.5)$$

To account for internal delays of the digital flight computer, actuators and sensors, a total of 25ms delay is modeled as shown below.

$$G_{del}(s) = e^{-0.025s} \quad (6.6)$$

To simplify the overall synthesis model, the parasitic dynamics is combined together

and reduced to a second order model. Further, the delay is approximated using a fifth order Pade approximation. The combined dynamics are

$$G_{para}(s) = \frac{0.966s^2 - 86.33s + 5539}{s^2 + 117.6s + 5539} \quad (6.7)$$

The parasitic dynamics described in Eq. (6.7) are combined with the reduced order BFF model to obtain the final synthesis model. The next section describes the baseline controller design for flutter suppression.

6.2 Baseline Control Design

The objective of control design is suppression of the unstable BFF mode as seen in the nominal BFF vehicle model beyond the flutter boundary. The purpose of the flutter suppression controller is to enable the aircraft dynamics to remain stable beyond the computed open loop nominal flutter boundary. Therefore, a linear model of the BFF vehicle at an airspeed beyond the flutter boundary is selected for control design. The linear model is constructed as described in the previous section, at an airspeed of 24.5 m/s, which is marginally higher than the nominal flutter boundary, which was computed in the previous chapter to be 23.8 m/s. The closed loop flutter boundary is computed to show the effectiveness of the controller in pushing the flutter boundary significantly beyond the open loop value. Robust flutter analysis for the closed loop system is carried out as well, which incorporates the uncertainties described in Chapter 4.

Since flutter suppression requires targeted damping of a specific mode, the \mathcal{H}_∞ control design [17, 18] is highly suitable for the problem. Using \mathcal{H}_∞ loopshaping techniques, we can also specify the frequency range of the control action, thereby ensuring that the controller does not affect other modes at lower or higher frequencies. As mentioned earlier, the control design is based on the work by Theis et al [115]. It should be noted that other multivariable control design techniques such as linear quadratic Gaussian control (LQG) have also been used for flutter suppression (e.g. see [16]), but will not be reviewed here.

Theis et al use a mixed sensitivity formulation [18] to design an \mathcal{H}_∞ controller which provides the desired closed loop characteristics for a given aircraft model. The formulation involves constructing a *generalized plant* P which includes weights to all

input-output signals of the aircraft model. These weights, either static or dynamic, help enforce the controller performance requirements. The controller is designed to minimize the induced \mathcal{L}_2 norm, also called the \mathcal{H}_∞ norm, for the closed loop around the generalized plant. The \mathcal{H}_∞ norm is defined as the largest input-output gain of a given system over all frequencies and all combinations of inputs and outputs. For a system $G(s)$ which has inputs d and outputs e , the \mathcal{H}_∞ norm can be mathematically expressed as

$$\|G(s)\| = \sup_{d \in \mathcal{L}_2} \frac{\|e\|_2}{\|d\|_2} \quad (6.8)$$

Therefore, by constructing the generalized plant P appropriately and choosing the signal weights carefully, performance objectives for the controller may be enforced. We focus our discussion only towards these aspects of the overall control design. The theory associated with \mathcal{H}_∞ control synthesis itself may be found in standard robust control texts, for e.g. [17, 18]. Software for control synthesis is commercially available within the Robust Control Toolbox in MATLAB [80].

Also as mentioned in the previous section, the model is modified to include a performance output in addition to the measurable outputs. The performance output is chosen as the modal velocity associated with the first mode - $\dot{\eta}_1$. The controller itself uses all the measurable outputs discussed in the previous subsection - pitch rate output, average center body accelerometer signal, and the averaged wing tip accelerometer signal and generates input signals for the outboard flaps. The interconnection of the generalized plant is shown in Fig. 6.2

The generalized plant represented within the dashed block in Fig. 6.2 has three input signals d , n , and u which denote external input disturbances, output sensor noise and the input signals associated with symmetric outboard flap deflections respectively. The output signals are the weighted input signals (e_1), weighted measurable outputs (e_2), weighted performance output (e_3) and measurable outputs with noise (\bar{y}). The signal \bar{y} is fed back to the controller which generates the input signal u . The weights associated with the input signals are W_d , W_n and W_u , where the subscripts point to the corresponding inputs. Similarly, weights associated with the outputs are denoted by W_p for performance output and W_y for measurable outputs. The generalized model may be visualized as a single block shown in Fig. 6.3.

The \mathcal{H}_∞ controller is designed to close the lower loop of the generalized plant as shown in Fig. 6.3. The closed loop is essentially an LFT interconnection denoted in robust

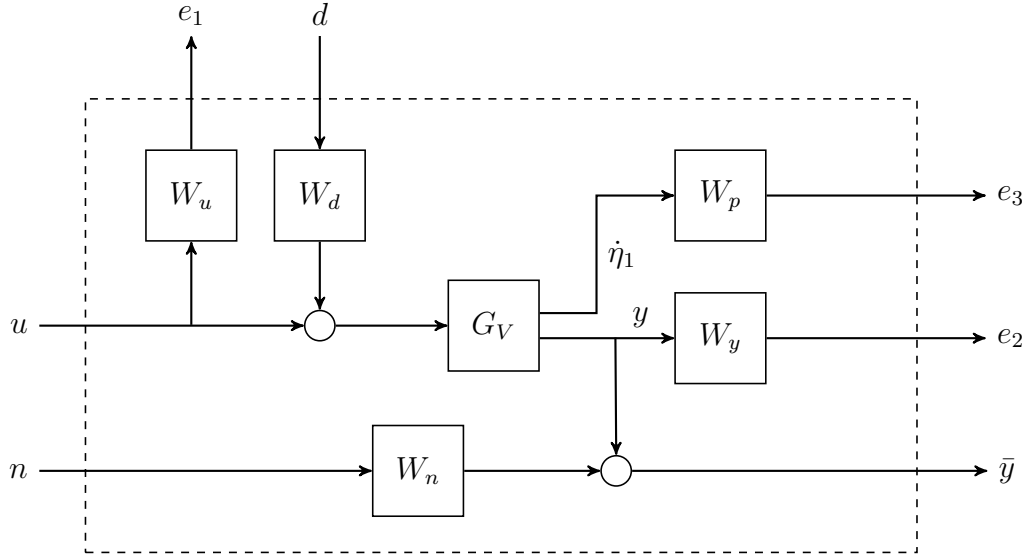
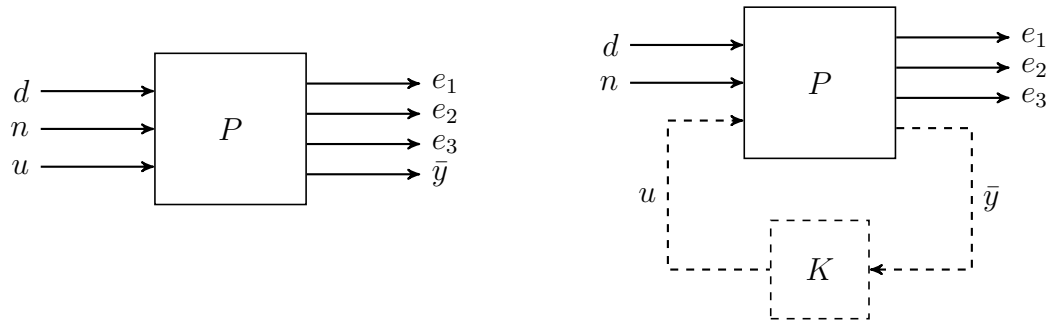


Figure 6.2: Generalized Plant interconnections



(a) Overall Generalized Plant Inputs and Outputs

(b) Controller closing lower LFT loop

Figure 6.3: H_∞ Control Design

control literature as $\mathcal{F}_L(P, K)$. As mentioned earlier, the controller K is designed to minimize the \mathcal{H}_∞ norm of the closed loop $\mathcal{F}_L(P, K)$ denoted by $\|\mathcal{F}_L(P, K)\|$. Therefore, the weights selected for each of the inputs and outputs influence the closed loop performance, as discussed next.

W_u is associated with the control input u which is generated by the controller in closed loop. Therefore, selecting a specific weighting for u limits the control action generated by the controller accordingly. For the BFF aircraft, W_u is chosen to be a frequency dependent weight. Specifically, it is chosen as a second order bandstop filter as shown in Fig. 6.4.

The weighted input signal e_1 is shaped by the weight W_u shown in Fig. 6.4, thereby

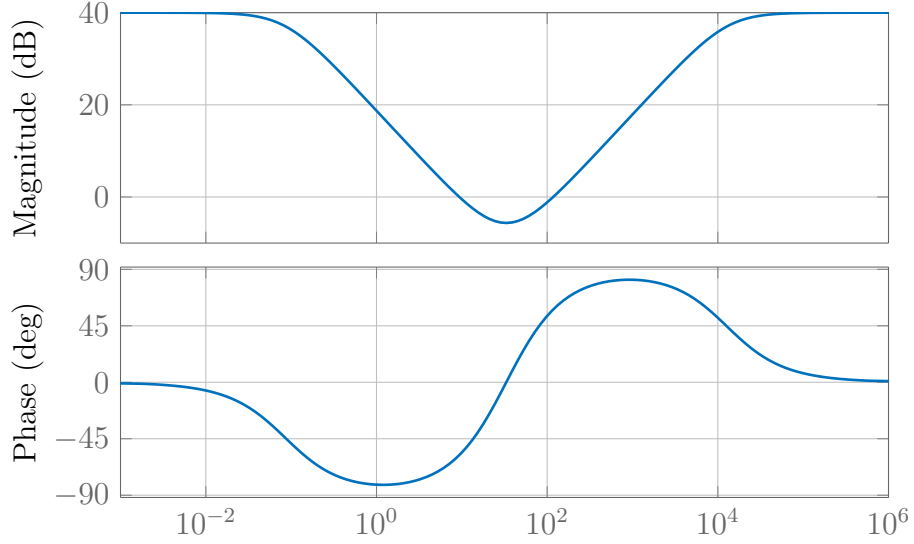


Figure 6.4: Control Input Weighting

penalizing any control action at lower or higher frequencies. In other words, selecting W_u as a bandstop filter shapes the controller like a bandpass filter. This ensures that the controller does not interfere with either low frequency rigid body dynamics or high frequency aeroelastic modes and other unmodeled dynamics. All the other weights are chosen to be static. W_p determines the amount of damping for the unstable BFF mode, thus influencing the closed loop flutter margin. W_d and W_n represent input and output disturbances. Their magnitude influences input and output robustness margins, thus determining controller performance in presence of any input or output multiplicative uncertainties. For further details on selection and tuning of the weights, see [115].

The generalized plant is constructed for the reduced order BFF model at 24.5 m/s and an \mathcal{H}_∞ controller is designed for it using the Robust Control Toolbox in Matlab, as described above. The controller frequency response is shown in Fig. 6.5.

From Fig. 6.5, we can clearly see that the controller is designed as a band-pass as desired. This is due to the influence of the input weight W_u described earlier. To confirm the selective action of the controller in damping the BFF mode exclusively, we look at the frequency response of both open and closed loop systems at 24.5 m/s for relevant input-output combinations. Fig. 6.6 shows the frequency response of the open and closed loop transfer functions from outboard flaps to the performance output $\dot{\eta}_1$.

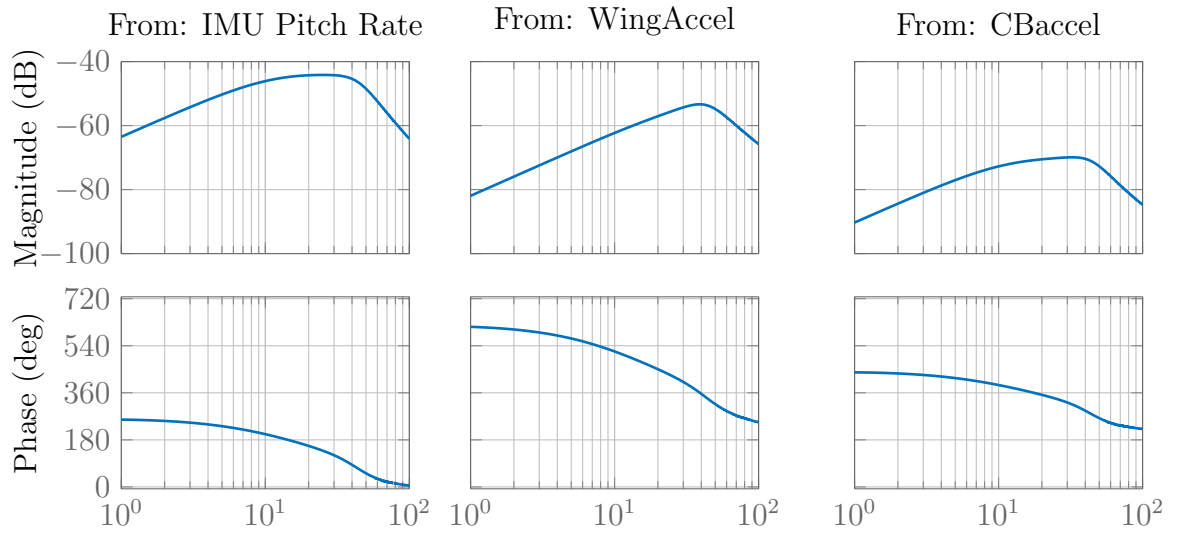


Figure 6.5: Controller Frequency Response

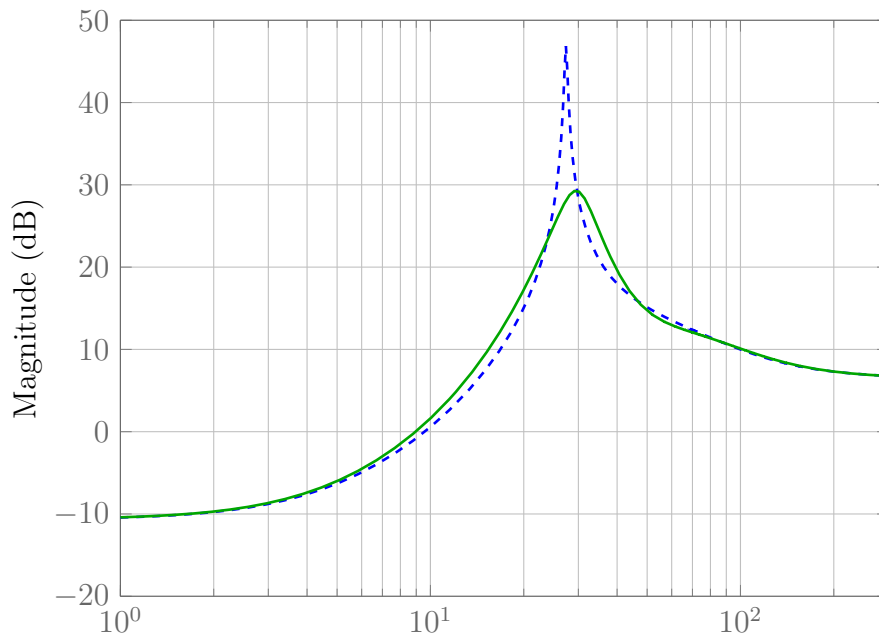


Figure 6.6: Open (---) and closed loop (—) frequency response of the performance output

Fig. 6.6 shows that the controller successfully damps the BFF mode at 24.5 rad/s in closed loop. We also look at the open and closed loop transfer function between outboard flaps to pitch rate in Fig. 6.7. The controller effectively damps the BFF mode without affecting either lower or higher frequency dynamics, as seen in Fig. 6.7. It is also important for check for the closed loop flutter boundary, which is expected

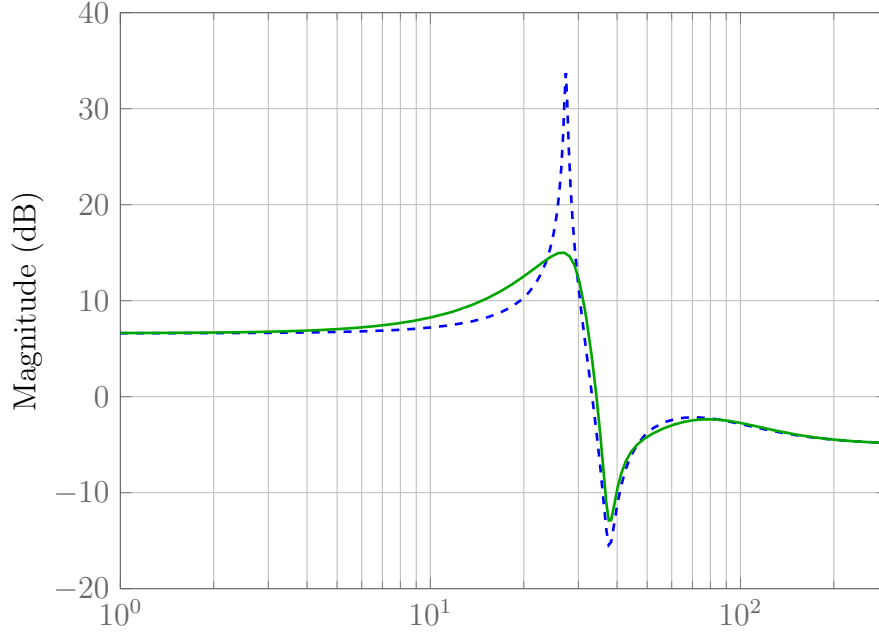


Figure 6.7: Open (---) and closed loop (—) frequency response for pitch rate output to be much higher than the open loop boundary which is 23.8 m/s. Nominal closed loop flutter boundary computation is discussed in the next subsection.

6.2.1 Nominal Closed Loop Flutter Boundary

The nominal flutter boundary for the BFF vehicle is 23.8 m/s as shown in Chapter 4. The \mathcal{H}_∞ controller is designed for a linear model derived at 24.5 m/s as described earlier. We use the same approach used earlier for nominal flutter analysis in Chapter 5 (see Fig. 5.3). The BFF mode is tracked for linear models across airspeeds varying from 6 m/s to 28 m/s. The controller designed at 24.5 m/s is used to close the loop around linear models across the range of airspeeds specified. The variation of the BFF mode is shown in Fig. 6.8.

From Fig. 6.8 we can see that the closed loop flutter boundary is at an airspeed of 26.3 m/s, which is about 10% higher than the open loop flutter speed of 23.8 m/s. The controller may be further tuned to achieve higher closed loop flutter boundaries if required. Furthermore, controllers designed at higher airspeeds may help in expanding the flight envelope further while simultaneously preserving stability at lower airspeeds. However for the purpose of the analysis in this chapter, the present controller is deemed adequate.

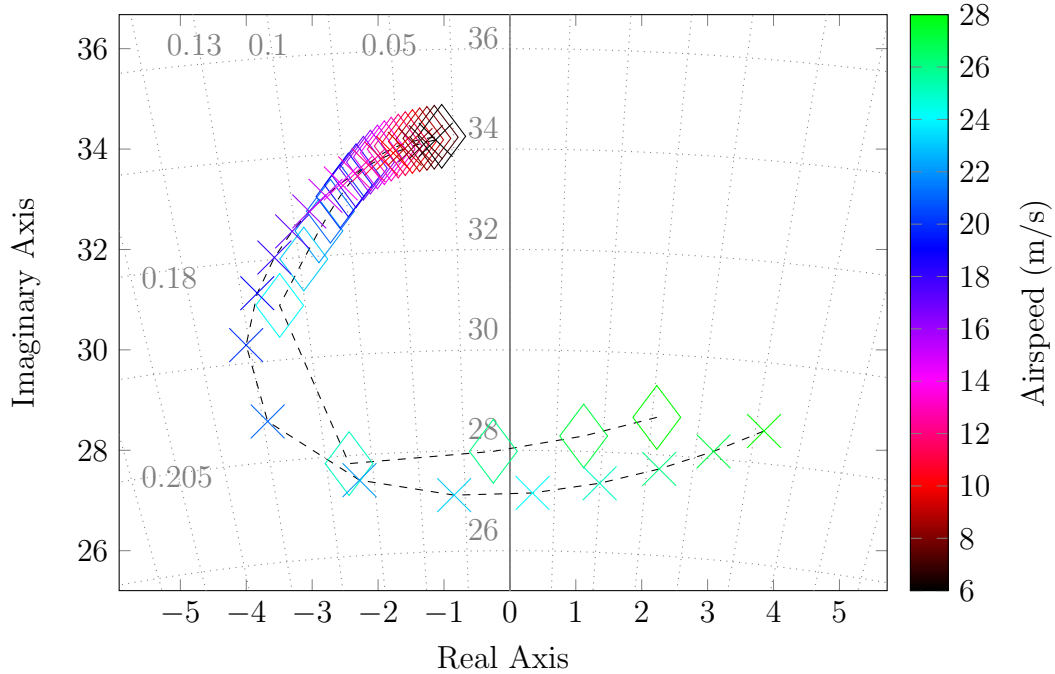


Figure 6.8: Pole map showing flutter boundary in the BFF model in closed loop. The next step in analyzing the closed loop BFF dynamics is to study the effect of model uncertainties. Like the open loop analysis process, a robust flutter boundary which takes into account model uncertainties specified in Chapter 4 is computed. That is followed by sensitivity analysis with respect to the uncertainty bounds. The next subsection discusses the robust flutter boundary computation and further ahead, the next section describes the sensitivity analysis.

6.2.2 Robust Closed Loop Flutter Boundary

The controller described in the previous section is designed using the nominal BFF vehicle model. Although input and output disturbances were incorporated in the mixed sensitivity approach, the impact of the controller is only analyzed for the nominal closed loop in Fig. 6.6, 6.7 and 6.8. We now look at closed loop performance with the baseline uncertain model in feedback with the controller designed at 24.5 m/s.

The primary metric of interest is the flutter boundary for the closed loop model with baseline uncertainties. In Chapter 5, robust flutter boundary for the baseline uncertain model is computed via μ analysis and is found to be 21.5 m/s. The same analysis tools, including the $\bar{K} - V$ graph, can be used to compute the closed loop robust flutter boundary as well. Fig. 6.9 shows the relevant $\bar{K} - V$ graph. Fig. 6.9

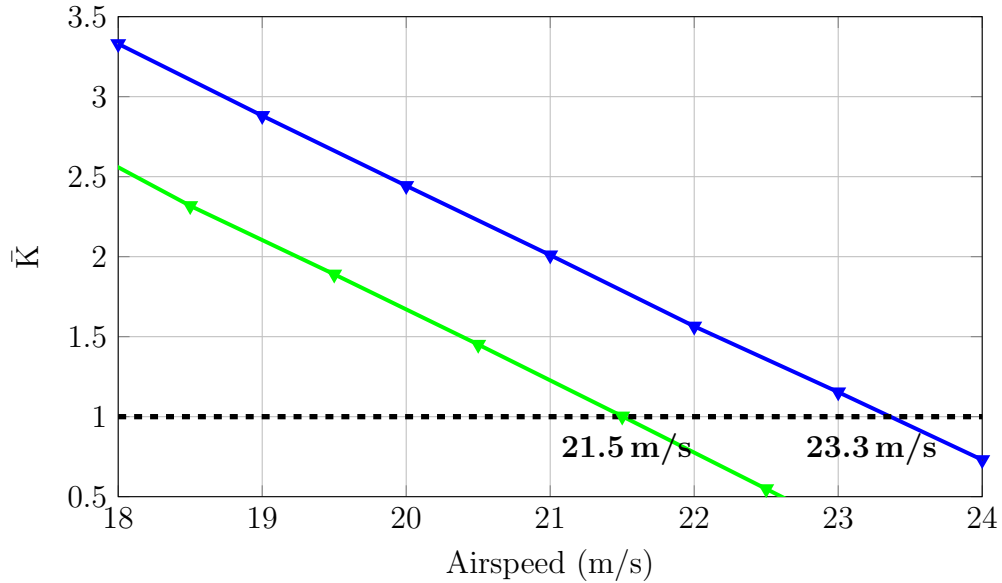


Figure 6.9: Closed (— \blacktriangledown) and open loop (— \blacktriangledown) $\bar{K} - V$ plot for Flutter Boundary shows that the robust flutter boundary for the closed loop system is at 23.3 m/s. The plot also shows the open loop robust flutter boundary (seen in Fig. 5.7 for comparison). The controller is able to increase the robust flutter boundary by approximately 9%, but unable to push it beyond the nominal flutter boundary which is 23.8 m/s. But more importantly, controller is unable to robustly stabilize the uncertain model at its design airspeed of 24.5 m/s.

It must be noted that control design techniques such as μ synthesis are available which directly take model uncertainties into account as a part of the synthesis process and synthesize controllers at the desired airspeed. Consequently, the resulting controllers push the robust flutter boundary to higher airspeeds [17, 18]. However, since the analysis in this chapter is not dependent on any particular performance objectives, the controller constructed here is considered suitable.

Finally, we carry out sensitivity analysis for the closed loop system to study the effect of variation in individual uncertainty specifications on the closed loop robust flutter boundary. The procedure is the same as that used for open loop analysis in the previous chapter. The analysis and the results are discussed in the next section.

6.3 Closed Loop Sensitivity Analysis

The objective for sensitivity analysis, as discussed in the previous chapter, is to determine the effect of individual parametric and non-parametric uncertainties on the overall model characteristics. Sensitivity analysis for the closed loop is important for taking into account the change in dynamics by introducing a controller in the loop. It is important to understand which uncertainty specifications are critical to a controller's ability to provide robust stability and performance. Also, since one of the reasons for doing a sensitivity analysis is to determine most likely sources of error in case of discrepancies in flight tests or experimental data, it is desirable to carry out both open and closed loop analyses for a complete understanding of the overall model.

As discussed in the previous section, the \mathcal{H}_∞ controller designed using a nominal model is unable to robustly stabilize the baseline uncertain model at the design airspeed of 24.5 m/s. The robust flutter boundary for the closed loop is computed to be 23.3 m/s, which is higher than the corresponding value to open loop. It is therefore interesting to investigate which uncertainties affect controller performance in terms of robust stability the most. We can then determine which parametric uncertainties need to be less conservative (i.e. which parameters are to be measured more accurately) for the given controller to robustly stabilize the model at its design point.

One way to analyze the effect of individual uncertainty bounds on controller's ability to robustly stabilize the system is to use the sensitivity analysis approach taken for open loop analysis in the previous chapter. The sensitivity scaling parameters described in Chapter 5 can be used to scale individual uncertainty bounds and the consequent variation in the robust flutter boundary in the closed loop can be studied. From the baseline robust boundary computation we know that the controller can robustly stabilize the BFF model up to an airspeed of 23.3 m/s. By observing the change in this boundary due to change in individual uncertainty bounds, we can deduce the effect of those uncertainties on controller performance.

We scale the sensitivity parameters between 0.5 and 2 and obtain a $\bar{K} - V$ graph for each of the individual uncertainty bounds which is analogous to Fig. 5.8. The $\bar{K} - V$ graph for scaling of $k_{E_{\text{sens}}}$ corresponding to bending stiffness is shown in Fig. 6.10.

After obtaining plots similar to Fig. 6.10 for all the uncertainties defined in the model,

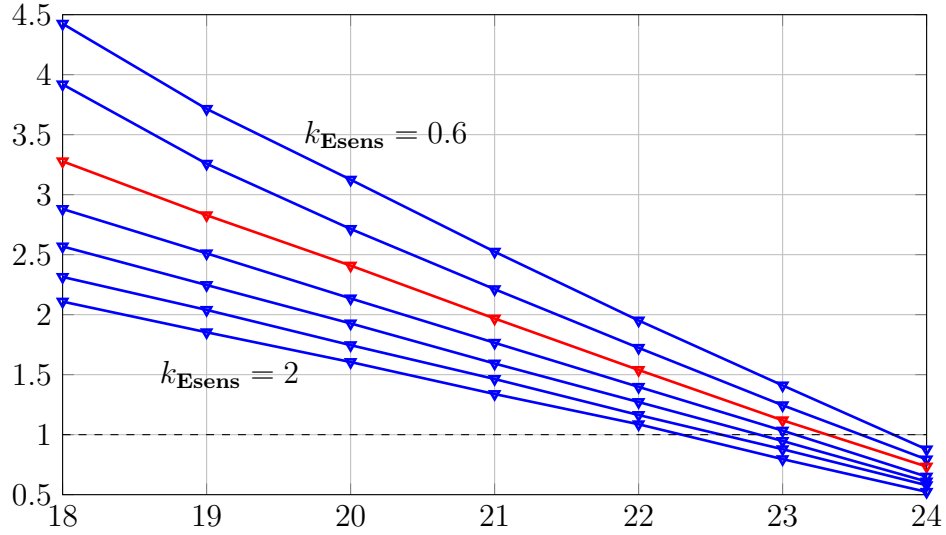


Figure 6.10: $\bar{K} - V$ graph variation for scaling in structural bending stiffness, closed loop

the overall sensitivity plot for the closed loop system may be obtained. The sensitivity plot for the open loop model is discussed in the preceding sections and shown in Fig. 5.10. The corresponding plot for the closed loop system is shown in Fig. 6.11.

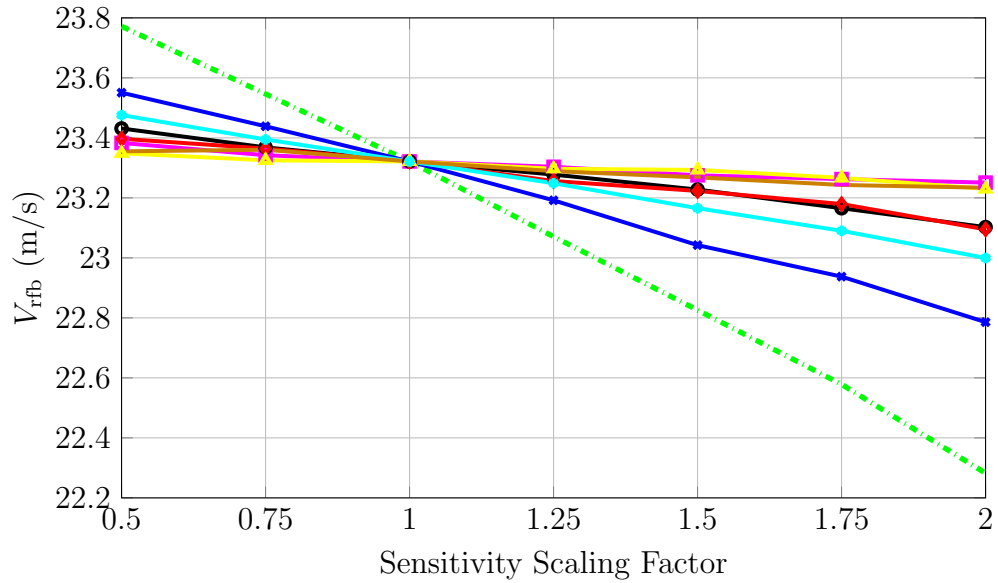


Figure 6.11: Closed loop sensitivity plot. The lines represent steady lift coeff: (—◆—), steady pitch coeff: (—▲—), unsteady aerodynamics: (—■—), Pitch moment of inertia: (—●—), Bending stiffness: (—■—), Torsional Stiffness (—▲—), C.G. location (—●—) and mass distribution (—●—)

Table 6.1 lists the slopes and relative slopes of the closed loop system in the descending order. The corresponding values obtained for open loop analysis are also included for comparison.

Table 6.1: Slopes of the Sensitivity Plot for different Uncertainties in closed loop

Uncertainty	Source	Closed Loop	Open loop
δ_E	Bending Stiffness	-0.99	-1.13
δ_G	Torsional Stiffness	-0.51	-0.33
δ_{cg}	C.G. Location	-0.32	-0.57
δ_{md}	Mass Dist.	-0.22	-0.39
δ_{C_L}	Steady Lift Coeff	-0.21	-0.21
Δ_{dyn}	Unsteady Aerodynamics	-0.088	-0.12
$\delta_{I_{yy}}$	Pitching mom. of Inertia	-0.081	-0.133
δ_{C_M}	Pitching Mom. Coeff	-0.079	-0.079

A quick reading of Table 6.1 shows that although the slopes for closed loop system generally follow a similar order of descendance as that corresponding to the open loop model, there is one significant change in the order, which is related to torsional stiffness. Also, there are significant changes in the magnitudes of slopes of most of the parameters. These changes are not necessarily proportional to the sensitivity values. Whereas sensitivity of the closed loop flutter boundary with respect to most parametric uncertainties decreases, sensitivity with respect to torsional stiffness uncertainty bound increases significantly compared to the open loop value. These observations are discussed in detail ahead.

The bending stiffness has maximum effect on the flutter boundary in closed loop. The controller effectiveness in terms of robustly stabilizing the system is twice as sensitive to the uncertainty in bending stiffness compared to the second uncertainty in the order. Therefore, just as the case with open loop flutter boundary, the closed loop flutter boundary can be pushed higher most effectively by tightening the bounds for bending stiffness uncertainty via better accuracy in experimental data.

The second most important parametric uncertainty is that of torsional stiffness, which has a rather high impact on closed loop flutter boundary. This is an interesting result since this uncertainty is not as important for the open loop flutter boundary computation when compared to other parameters such as C.G. location or mass distribution. In fact, it is the only parameter with respect to which the closed loop

flutter boundary sensitivity is higher than the open loop value, as seen in Table 6.1. In Chapter 5, the contribution of wing twist to the BFF mode due to the swept wing design was discussed in order to address the sensitivity of open loop flutter boundary with respect to torsional stiffness. The open loop sensitivity, although not particularly high as noted above, is nevertheless significant. In the closed loop, this aspect of the BFF mode appears to be more pronounced, thus leading to increased sensitivity. Specifically, the stabilization action of the controller via outboard flaps appears to be highly sensitive to wing twist, probably because outboard flaps tend to generate a wing twist in addition to the expected wing bending. The reason for this is also the swept back wing design. Therefore, a change in uncertainty pertaining to torsional stiffness parameter affects the closed loop flutter boundary even more than it does for the open loop case.

The order for remaining uncertainties in closed loop is similar to that of open loop. The C.G. location and mass distribution follow in the same order, although the sensitivity of the closed loop boundary is lower than that of open loop. Therefore, it is much harder to push the flutter boundary up in closed loop (i.e. improved robust stability by the controller) compared to the open loop case. The same is true for steady and unsteady aerodynamics uncertainties as well as the pitching moment of inertia. Although the dynamic uncertainty related to unsteady aerodynamics and parametric uncertainty for the pitching moment of inertia trade places in terms of the order of descendence, the sensitivity slope values for both cases are very close to one another. And finally, the invariance of both uncertainties associated with steady aerodynamics i.e. steady lift coefficient and steady pitching moment coefficient indicates their little influence on the flutter boundary in open or closed loop. Their conservativeness neither affects the computation for a robust flutter boundary in the open loop, nor the robust stability provided by the controller in closed loop.

As observed earlier, with the exception of the parametric uncertainty for torsional stiffness, sensitivity of the closed loop flutter boundary with respect to all other uncertainties decreases in magnitude compared to the open loop values. A reason for this could be that the controller is designed to selectively and robustly damp the BFF mode and leave all other modes unaffected. Therefore, the closed loop system becomes more robust to changes in parameters as well as parametric uncertainties dominantly associated with the BFF mode. Of course, Table 6.1 shows that the effect of the controller on sensitivity towards a given parameter in closed loop is not

directly related to the corresponding value in open loop. Therefore a parameter which has significant influence on the flutter boundary in open loop may continue to do so in closed loop, as is the case with bending stiffness, that sees a drop of only 12%. On the other hand, the controller may cause additional reduction in sensitivity with respect to a parameter which does not have a significant influence on the open loop flutter boundary in the first place. For example, we can see from Table 6.1 that the sensitivity towards unsteady aerodynamics is further decreased by more than 23%. Finally, a differently tuned or designed controller may provide different results with respect to the same uncertainties. Therefore, these differences essentially justify the need to repeat this analysis for the closed loop system.

Further investigation into these results can lead to significant insights on how the controller and associated control design procedures are effected by these uncertainty specifications. These results may not be generalizable to all controllers, but they underline the importance of carrying out such analyses for closed loop systems in any aeroservoelastic model. Since a controller in the loop alters the sensitivity of the closed loop flutter boundary with respect to different parameters, sensitivity analysis for closed loop systems cannot be overlooked even if an open loop analysis has been done.

6.4 Summary

In this chapter, a closed loop robustness analysis is carried out for the BFF vehicle with model uncertainties. An \mathcal{H}_∞ controller is designed for flutter suppression using the nominal model at a design point of 24.5 m/s. The nominal flutter boundary with controller in the loop is computed to be 26.3 m/s, thus expanding the envelope beyond the nominal open loop flutter boundary of 23.8 m/s. However, the controller is unable to robustly stabilize the baseline uncertain model developed in Chapter 5 at the design airspeed. The closed loop robust flutter boundary is at 23.3 m/s, which although higher than the robust open loop boundary, is marginally lower than the nominal open value state above.

A sensitivity analysis similar to that in Chapter 5 is carried out for the closed loop system. The objective is to determine the individual uncertainty specifications which affect the ability of the controller to robustly stabilize the uncertain model. By studying the sensitivity graph, uncertainties which affect the closed loop flutter boundary

the most, and therefore affect the stability provided by the controller can be determined. The results and their interpretations are discussed in detail, with a particular focus on uncertainty associated with torsional stiffness which is the only one with respect to which sensitivity of the robust flutter boundary in closed loop is higher than in the open loop.

Chapter 7

Conclusion

In the concluding chapter for this thesis, closing remarks the overall research and the associated results are provided. Several new avenues for research can be explored on the basis of this work. Some of the important future directions are discussed as well.

7.1 Conclusions

The work described in this thesis provides a framework for constructing and analyzing aeroservoelastic systems with model uncertainties for robust stability and performance. The body freedom flutter vehicle, constructed by Lockheed Martin and the Air Force Research Laboratory, is used as an application for this research work. The construction of a nonlinear aeroelastic model for a flexible fixed wing air vehicle is described using the concept of mean axes, which combines nonlinear rigid body dynamics with a linear structural model in a minimally coupled manner. Unsteady aerodynamics, which is also a part of the modeling process, is modeled using the doublet lattice method (DLM). The coordinate transformation required to project the results obtained from the DLM into the structural modal space is also described. The unsteady nature of aerodynamics results in a lag in the aerodynamic forcing function, which is instrumental in causing instabilities. Also, the aerodynamic model is a function of airspeed and the vibrational frequencies of the lifting surface, which lends a linear parameter varying nature to the aeroelastic model. Finally, linear aeroelastic models are obtained across a range of fixed airspeeds for straight and level flight via linearization of the nonlinear model at the corresponding trim conditions.

Based on the nominal model, model uncertainties are specified to account for errors in experimental data as well as modeling procedures. The research work focuses on a consistent and holistic definition of model uncertainties in order to obtain an uncertain model within the robust control theory framework which is not too conservative. Eigenvector derivative based parametric uncertainty definitions are used for the construction of uncertain models in structural modal coordinates. Errors in modeling procedures for the aerodynamic model are accounted for via frequency dependent dynamic uncertainties. Stability analysis using μ as a measure of robustness is described for computing the robust flutter boundary for a given uncertain aeroelastic model. A sensitivity analysis method is also developed to study the effects of individual uncertainties and their magnitudes on the predicted robust flutter boundary. The entire process of constructing uncertain models and carrying out robust flutter analysis as well as sensitivity analysis is demonstrated for the BFF vehicle. Finally, an \mathcal{H}_∞ flutter suppression control law is synthesized for the BFF vehicle to extend the flight envelope beyond the nominal flutter boundary. The robust flutter analysis and sensitivity analysis are repeated for an uncertain model of the BFF vehicle in closed loop with the flutter suppression controller to study the effects of altered closed loop dynamics on the results.

Each one of the topics explored in this research work, be it flexible airframe dynamics, unsteady aerodynamics modeling, uncertainty descriptions or robust flutter analysis, has provided significant insights into the challenges commonly faced in the overall field of aeroservoelasticity. For instance, the mean axes approach to modeling flexible airframe dynamics attempts to address the model complexity due to highly coupled dynamics of rigid and structural modes, and in the process, provides an opportunity to study the nature of the underlying coupling terms. Similarly, defining structural parametric uncertainties based on mode shape uncertainties leads to the use of eigenvector derivatives in determining which parametric uncertainties affect mode shapes of a finite element model the most. These results and insights lead to several future directions that the research community can follow to understand and address the theoretical as well as application problems in the field. Some of the potential future directions are discussed ahead.

7.2 Future Directions

This work opens up new avenues for research in theory as well as experiments related to aeroservoelasticity. Some important directions for future research based on this thesis are discussed ahead.

In Chapter 4, several uncertainty descriptions are explored and incorporated into the final uncertain model. The parameters considered uncertain include bending and torsional stiffness, mass distribution, pitching moment of inertia, C.G. location, steady aerodynamics coefficients and dynamic uncertainty for unsteady aerodynamics. There is scope for further research into how these uncertainties are defined and additional parameters that could be included in this list.

The unsteady aerodynamics uncertainty remains the only one which is based on errors in methodology (fitting errors). It does not incorporate any experimental data, since experimental data for unsteady loads for the BFF vehicle is not available. There are two potential ways that can be developed to model this uncertainty in a more comprehensive manner. The first way is to study the differences between the data obtained from a simple oscillating wing experiment (e.g. Benchmark Active Controls Technology (BACT) wind tunnel set up [97]) and its theoretical model obtained from the DLM. Although it is not a direct estimate of uncertainty within the BFF model, it helps understand the drawbacks of the DLM approach and help improve the uncertainty specification. Secondly, research effort can be undertaken to compare the DLM results for the BFF vehicle with unsteady aerodynamics models built using high fidelity CFD methods [118] and estimate the error bounds which account for any possible differences. A better baseline uncertainty model for unsteady aerodynamics can help in providing a more credible estimate of sensitivity of the flutter boundary with respect to it.

Recent developments in the PAAW project have opened up the possibility of an additional model uncertainty in the structural dynamics subsystem - asymmetric stiffness. It is possible that in the absence of industry-level precision manufacturing capabilities, a small difference of bending and/or torsional stiffness may be present between the two wings. Since each wing is manufactured individually, it is certainly not possible to build them identically. Typically, very small differences in stiffness could be ignored, while small differences in mass can be corrected. However, if the asymmetry in stiffness is significant enough, there could be unwanted coupling between symmetric and

asymmetric structural modes. Therefore, it is important to quantify and account for such asymmetry via a small uncertainty in stiffness modeled separately for each wing. The control design process for such a model will need to be altered as well, since the control authority in lateral-directional axes would be required. Effort should also be made to include flight test data into the uncertainty specification process to obtain an uncertain model which is validated via multiple ground tests as well as flight tests.

Finally, Chapter 6 provides interesting results for sensitivity analysis in closed loop. Specifically, the role played by a controller in altering the sensitivity of the flutter boundary with respect to different uncertainties needs to be analyzed thoroughly. Sensitivity analysis for different controllers can be compared to gain more insights into how each uncertainty affects the closed loop flutter boundary and conversely, how a given controller affects the influence of different uncertainties on the flutter boundary.

Bibliography

- [1] Scanlan, R. H. and Rosenbaum, R., *Introduction to the study of aircraft vibration and flutter*, Dover Publications, 1951.
- [2] Cox, D., Curtiss Jr, H., Edwards, J., Hall, K., Peters, D. A., Scanlan, R., Simiu, E., and Sisto, F., *A modern course in aeroelasticity*, Vol. 116, Springer, 2006.
- [3] Fung, Y. C., *An introduction to the theory of aeroelasticity*, Courier Dover Publications, 2002.
- [4] Kotikalpudi, A., Pfifer, H., and Balas, G. J., “Unsteady Aerodynamics Modeling for a Flexible Unmanned Air Vehicle,” *AIAA Atmospheric Flight Mechanics Conference*, 2015, p. 2854.
- [5] Kotikalpudi, A., Moreno, C., Taylor, B., Pfifer, H., and Balas, G. J., “Low cost development of a nonlinear simulation for a flexible uninhabited air vehicle,” *American Control Conference*, 2014, pp. 2029–2034.
- [6] Moreno, C., Seiler, P., and Balas, G., “Linear parameter varying model reduction for aeroservoelastic systems,” *AIAA Atmospheric Flight Mechanics Conference*, 2012, p. 4859.
- [7] Theis, J., Takarics, B., Pfifer, H., Balas, G., and Werner, H., “Modal Matching for LPV Model Reduction of Aeroservoelastic Vehicles,” *AIAA Science and Technology Forum*, 2015.
- [8] Wang, S., Pfifer, H., and Seiler, P., “Robust synthesis for linear parameter varying systems using integral quadratic constraints,” *Conference on Decision and Control*, IEEE, 2014, pp. 4789–4794.

- [9] Theis, J., Pfifer, H., and Seiler, P., “Robust Control Design for Active Flutter Suppression,” *AIAA Atmospheric Flight Mechanics Conference*, 2016.
- [10] Moreno, C. P., Gupta, A., Pfifer, H., Taylor, B., and Balas, G. J., “Structural model identification of a small flexible aircraft,” *American Control Conference*, 2014, pp. 4379–4384.
- [11] Gupta, A., Moreno, C., Pfifer, H., Taylor, B., and Balas, G., “Updating a finite element based structural model of a small flexible aircraft,” *AIAA Scitech Conference*, 2015.
- [12] Dorobantu, A., Johnson, W., Lie, F. A., Taylor, B., Murch, A., Paw, Y. C., Gebre-Egziabher, D., and Balas, G., “An airborne experimental test platform: From theory to flight,” *American Control Conference 2013*, 2013, pp. 659–673.
- [13] Dorobantu, A., Murch, A., Mettler, B., and Balas, G., “System identification for small, low-cost, fixed-wing unmanned aircraft,” *Journal of Aircraft*, Vol. 50, No. 4, 2013, pp. 1117–1130.
- [14] Pfifer, H. and Danowsky, B., “System Identification of a Small Flexible Aircraft,” *AIAA Atmospheric Flight Mechanics Conference*, 2016.
- [15] Regan, C. and Taylor, B., “mAEWing1: Design, Build test,” *AIAA Atmospheric Flight Mechanics Conference*, 2016.
- [16] Burnett, E., Atkinson, C., Beranek, J., Sibbitt, B., Holm-Hansen, B., and Nicolai, L., “NDoF Simulation model for flight control development with flight test correlation,” *AIAA Modeling and Simulation Technologies Conference*, Vol. 3, 2010, pp. 7780–7794.
- [17] Zhou, K., Doyle, J. C., and Glover, K., *Robust and optimal control*, Vol. 40, Prentice hall New Jersey, 1996.
- [18] Skogestad, S. and Postlethwaite, I., *Multivariable feedback control: analysis and design*, Vol. 2, Wiley New York, 2007.
- [19] Borglund, D., “The mu-k method for robust flutter solutions,” *Journal of Aircraft*, Vol. 41, No. 5, 2004, pp. 1209–1216.
- [20] Lind, R. and Brenner, M., *Robust aeroservoelastic stability analysis: Flight test applications*, Springer Science & Business Media, 2012.

- [21] Lind, R. and Brenner, M., “Flutterometer: an on-line tool to predict robust flutter margins,” *Journal of Aircraft*, Vol. 37, No. 6, 2000, pp. 1105–1112.
- [22] Megretski, A. and Rantzer, A., “System analysis via integral quadratic constraints,” *IEEE Transactions on Automatic Control*, Vol. 42, No. 6, 1997, pp. 819–830.
- [23] Vuillemin, P., Demourant, F., Biannic, J.-M., and Poussot-Vassal, C., “Global stability validation of an uncertain large-scale aircraft model,” *Conference on Control Applications (CCA)*, IEEE, 2014, pp. 152–157.
- [24] Demourant, F., “New algorithmic approach based on integral quadratic constraints for stability analysis of high order models,” *European Control Conference (ECC)*, IEEE, 2013, pp. 359–364.
- [25] Cook, M. V., *Flight dynamics principles: a linear systems approach to aircraft stability and control*, Butterworth-Heinemann, 2012.
- [26] Nelson, R. C., *Flight stability and automatic control*, Vol. 2, WCB/McGraw Hill, 1998.
- [27] McRuer, D. T., Graham, D., and Ashkenas, I., *Aircraft dynamics and automatic control*, Princeton University Press, 2014.
- [28] Milne, R. D., *Dynamics of the deformable aeroplane*, HM Stationery Office, 1964.
- [29] Waszak, M. R. and Schmidt, D. K., “Flight dynamics of aeroelastic vehicles,” *Journal of Aircraft*, Vol. 25, No. 6, 1988, pp. 563–571.
- [30] Guimarães Neto, A. B., Silva, R. G., Paglione, P., and Silvestre, F. J., “Formulation of the Flight Dynamics of Flexible Aircraft Using General Body Axes,” *AIAA Journal*, 2016, pp. 3516–3534.
- [31] Canavin, J. and Likins, P., “Floating reference frames for flexible spacecraft,” *Journal of Spacecraft and Rockets*, Vol. 14, No. 12, 1977, pp. 724–732.
- [32] Meirovitch, L. and Tuzcu, I., “The lure of the mean axes,” *Journal of Applied Mechanics*, Vol. 74, No. 3, 2007, pp. 497–504.

- [33] Schmidt, D. K., “Discussion:The Lure of the Mean Axes(Meirovitch, L., and Tuzcu, I., ASME J. Appl. Mech., 74 (3), pp. 497–504),” *Journal of Applied Mechanics*, Vol. 82, No. 12, 2015, pp. 125501.
- [34] Fowles, G. R. and Cassiday, G. L., *Analytical mechanics*, Saunders college, 1999.
- [35] Lurie, A. I., *Analytical mechanics*, Springer Science & Business Media, 2013.
- [36] Sokolnikoff, I. S., Specht, R. D., et al., *Mathematical theory of elasticity*, Vol. 83, McGraw-Hill New York, 1956.
- [37] Nikraves, P. E., “Understanding mean-axis conditions as floating reference frames,” *Advances in Computational Multibody Systems*, Springer, 2005, pp. 185–203.
- [38] Keyes, S. A., Seiler, P. J., and Schmidt, D. K., “A Newtonian Development of the Mean-Axis Equations of Motion for Flexible Aircraft,” *AIAA Atmospheric Flight Mechanics Conference*, 2017, p. 1395.
- [39] Clough, R. W. and Tocher, J. L., “Finite element stiffness matrices for analysis of plates in bending,” *Proceedings of conference on matrix methods in structural analysis*, Vol. 1, 1965.
- [40] Ngo, D. and Scordelis, A., “Finite element analysis of reinforced concrete beams,” *American Concrete Institute Journal Proceedings*, Vol. 64, 1967.
- [41] Chandrupatla, T. R., Belegundu, A. D., Ramesh, T., and Ray, C., *Introduction to finite elements in engineering*, Vol. 2, Prentice Hall Upper Saddle River, NJ, 2002.
- [42] Shames, I. H., *Mechanics of fluids*, McGraw-Hill New York, 1982.
- [43] Anderson Jr John, D., *Fundamentals of aerodynamics*, McGraw-Hill, 1984.
- [44] Katz, J. and Plotkin, A., *Low speed aerodynamics: From wing theory to panel methods*, New York: Mc–Graw-H ill Book Co, 1991.
- [45] Fung, Y. C., *An introduction to the theory of aeroelasticity*, Courier Corporation, 2002.

- [46] Bisplinghoff, R. L. and Ashley, H., *Principles of aeroelasticity*, Courier Corporation, 2013.
- [47] Anderson, J. D. and Wendt, J., *Computational fluid dynamics*, Vol. 206, Springer, 1995.
- [48] Hirsch, C., *Numerical computation of internal and external flows: The fundamentals of computational fluid dynamics*, Butterworth-Heinemann, 2007.
- [49] Farhat, C., Lesoinne, M., and Le Tallec, P., “Load and motion transfer algorithms for fluid/structure interaction problems with non-matching discrete interfaces: Momentum and energy conservation, optimal discretization and application to aeroelasticity,” *Computer methods in applied mechanics and engineering*, Vol. 157, No. 1, 1998, pp. 95–114.
- [50] Farhat, C., Geuzaine, P., and Brown, G., “Application of a three-field nonlinear fluid-structure formulation to the prediction of the aeroelastic parameters of an F-16 fighter,” *Computers & Fluids*, Vol. 32, No. 1, 2003, pp. 3–29.
- [51] Rodden, W. P. and Stahl, B., “A strip method for prediction of damping in subsonic wind tunnel and flight flutter tests.” *Journal of Aircraft*, Vol. 6, No. 1, 1969, pp. 9–17.
- [52] Belotserkovskii, S. M., “Study of the unsteady aerodynamics of lifting surfaces using the computer,” *Annual Review of Fluid Mechanics*, Vol. 9, No. 1, 1977, pp. 469–494.
- [53] Hough, G. R., “Remarks on vortex lattice methods.” *Journal of Aircraft*, Vol. 10, No. 5, 1973, pp. 314–317.
- [54] Lan, C. E., “A quasi-vortex lattice method in thin wing theory,” *Journal of Aircraft*, Vol. 11, No. 9, 1974, pp. 518–527.
- [55] Albano, E. and Rodden, W. P., “A doublet-lattice method for calculating lift distributions on oscillating surfaces in subsonic flows.” *AIAA Journal of Aircraft*, Vol. 7, No. 2, 1969, pp. 279–285.
- [56] Rodden, W. P., Taylor, P. F., and McIntosh, S. C., “Further refinement of the subsonic doublet-lattice method,” *Journal of Aircraft*, Vol. 35, No. 5, 1998, pp. 720–727.

- [57] Houghton, E. L. and Carpenter, P. W., *Aerodynamics for engineering students*, Butterworth-Heinemann, 2003.
- [58] Blair, M., “A compilation of the mathematics leading to the doublet lattice method,” Tech. rep., DTIC Document, 1992.
- [59] Kotikalpudi, A., Pfifer, H., and Balas, G. J., “Unsteady Aerodynamics Modeling for a Flexible Unmanned Air Vehicle,” *AIAA Atmospheric Flight Mechanics Conference*, 2015, p. 2854.
- [60] Rodden, W. P. and Johnson, E. H., *MSC/NASTRAN Aeroelastic Analysis: User’s Guide, Version 68*, MacNeal-Schwendler Corporation, 1994.
- [61] Rodden, W. P., “Further remarks on matrix interpolation of flexibility influence coefficients,” *Journal of the Aerospace Sciences*, 2012.
- [62] Harder, R. L. and Desmarais, R. N., “Interpolation using surface splines.” *Journal of aircraft*, Vol. 9, No. 2, 1972, pp. 189–191.
- [63] Kier, T. and Looye, G., “Unifying manoeuvre and gust loads analysis models,” *International Forum on Aeroelasticity & Structural Dynamics*, 2009.
- [64] Roger, K. L., “Airplane math modeling methods for active control design,” *Advisory Group for Aerospace Research and Development CP-228*, 1977, pp. 4–1.
- [65] Vepa, R., “Finite state modeling of aeroelastic systems,” 1977.
- [66] Karpel, M., *Design for active and passive flutter suppression and gust alleviation*, Vol. 3482, National Aeronautics and Space Administration, Scientific and Technical Information Branch, 1981.
- [67] Rodden, W., Taylor, P., and McIntosh, S., “Improvements to the Doublet-Lattice Method in MCS/NASTRAN,” *MacNeal-Schwendler Corp., Technical Rept., Los Angeles, Sept*, 1999.
- [68] Drela, M., “XFLR-5, open source VLM software,” <http://www.xflr5.com>.
- [69] Pettit, C. L., “Uncertainty quantification in aeroelasticity: recent results and research challenges,” *Journal of Aircraft*, Vol. 41, No. 5, 2004, pp. 1217–1229.

- [70] Melchers, R. E., *Structural reliability analysis and prediction*, John Wiley & Son Ltd, 1999.
- [71] Kleiber, M. and Hien, T. D., *The stochastic finite element method: for use on IBM PC/XT*, Wiley, 1992.
- [72] Roger, G. G. and Spanos, P. D., *Stochastic finite elements: A spectral approach*, Springer-Verlag New York, Inc., New York, NY, USA, 1991.
- [73] Beran, P. S., Pettit, C. L., and Millman, D. R., “Uncertainty quantification of limit-cycle oscillations,” *Journal of Computational Physics*, Vol. 217, No. 1, 2006, pp. 217–247.
- [74] Manan, A. and Cooper, J., “Design of composite wings including uncertainties: a probabilistic approach,” *Journal of Aircraft*, Vol. 46, No. 2, 2009, pp. 601–607.
- [75] Hosder, S., Walters, R. W., and Balch, M., “Efficient uncertainty quantification applied to the aeroelastic analysis of a transonic wing,” *46th AIAA Aerospace Sciences Meeting and Exhibit, Reno, NV, January*, 2008, pp. 7–10.
- [76] Ben-Haim, Y. and Elishakoff, I., *Convex models of uncertainty in applied mechanics*, Vol. 25, Elsevier, 2013.
- [77] Rao, S. S. and Berke, L., “Analysis of uncertain structural systems using interval analysis,” *AIAA journal*, Vol. 35, No. 4, 1997, pp. 727–735.
- [78] Muhanna, R. L. and Mullen, R. L., “Uncertainty in mechanics problems—interval-based approach,” *Journal of Engineering Mechanics*, Vol. 127, No. 6, 2001, pp. 557–566.
- [79] Elishakoff, I., “Essay on uncertainties in elastic and viscoelastic structures: from AM Freudenthal’s criticisms to modern convex modeling,” *Computers & Structures*, Vol. 56, No. 6, 1995, pp. 871–895.
- [80] Balas, G., Chiang, R., Packard, A., and Safonov, M., “Robust control toolbox,” *For Use with Matlab. Users Guide, Version*, Vol. 3, 2005.
- [81] Borglund, D., “Upper Bound Flutter Speed Estimation Using the mu-k Method,” *Journal of Aircraft*, Vol. 42, No. 2, 2005, pp. 555–557.

- [82] Borglund, D. and Ringertz, U., “Efficient computation of robust flutter boundaries using the mu-k method,” *Journal of Aircraft*, Vol. 43, No. 6, 2006, pp. 1763–1769.
- [83] Karpel, M., Moulin, B., and Idan, M., “Aeroservoelastic design process using structural optimization and robust control methods,” *8th Symposium on Multidisciplinary Analysis and Optimization*, 2000, p. 4722.
- [84] Chavez, F. R. and Schimdt, D., “Systems approach to characterizing aircraft aeroelastic model variation for robust control applications,” *AIAA Paper*, Vol. 4020, No. 6, 2001, pp. 9.
- [85] Kehoe, M. W., “Aircraft ground vibration testing at NASA Ames-Dryden flight research facility,” 1987.
- [86] Mottershead, J. and Friswell, M., “Model updating in structural dynamics: a survey,” *Journal of sound and vibration*, Vol. 167, No. 2, 1993, pp. 347–375.
- [87] Caesar, B. and Peter, J., “Direct update of dynamic mathematical models from modal test data,” *AIAA journal*, Vol. 25, No. 11, 1987, pp. 1494–1499.
- [88] Nelson, R. B., “Simplified calculation of eigenvector derivatives,” *AIAA journal*, Vol. 14, No. 9, 1976, pp. 1201–1205.
- [89] Lin, R., Wang, Z., and Lim, M., “A practical algorithm for the efficient computation of eigenvector sensitivities,” *Computer methods in applied mechanics and engineering*, Vol. 130, No. 3, 1996, pp. 355–367.
- [90] Friswell, M. I., “Calculation of second and higher order eigenvector derivatives,” *Journal of Guidance, Control, and Dynamics*, Vol. 18, No. 4, 1995, pp. 919–921.
- [91] Weisstein, E. W., “Least squares fitting,” 2002.
- [92] Van den Berg, E. and Friedlander, M. P., “Sparse optimization with least-squares constraints,” *SIAM Journal on Optimization*, Vol. 21, No. 4, 2011, pp. 1201–1229.
- [93] Cotter, S. F., Rao, B. D., Egan, K., and Kreutz-Delgado, K., “Sparse solutions to linear inverse problems with multiple measurement vectors,” *IEEE Transactions on Signal Processing*, Vol. 53, No. 7, 2005, pp. 2477–2488.

- [94] Tibshirani, R., “Regression shrinkage and selection via the lasso,” *Journal of the Royal Statistical Society. Series B (Methodological)*, 1996, pp. 267–288.
- [95] Rae, W. H. and Pope, A., *Low-speed wind tunnel testing*, John Wiley, 1984.
- [96] Fingersh, L. J., Simms, D., Hand, M., Jager, D., Cotrell, J., Robinson, M., Schreck, S., and Larwood, S., “Wind tunnel testing of NRELS unsteady aerodynamics experiment,” *AIAA paper*, Vol. 35, 2001, pp. 2001.
- [97] Waszak, M. R., “Modeling the benchmark active control technology wind-tunnel model for application to flutter suppression,” *AIAA Atmospheric Flight Mechanics Conference, San Diego, California*, Vol. 96, 1996.
- [98] Melin, T., “Tornado,” *KTH, Stockholm, Sweden, Masters Thesis and continued development*. <http://www.flyg.kth.se/divisions/aero/software/tornado>, 2013.
- [99] Woolston, D. S., “An Investigation of Effects of Certain Types of Structural Nonlinearities on Wing and Control Surface Flutter,” *Journal of the Aeronautical Sciences*, 2012.
- [100] Conner, M., Tang, D., Dowell, E., and Virgin, L., “Nonlinear behavior of a typical airfoil section with control surface freeplay: a numerical and experimental study,” *Journal of Fluids and structures*, Vol. 11, No. 1, 1997, pp. 89–109.
- [101] Kehoe, M. W., “A historical overview of flight flutter testing,” 1995.
- [102] Denegri, C. M., “Limit cycle oscillation flight test results of a fighter with external stores,” *Journal of Aircraft*, Vol. 37, No. 5, 2000, pp. 761–769.
- [103] Bennett, R. M. and Edwards, J. W., “An overview of recent developments in computational aeroelasticity,” *AIAA paper*, Vol. 2421, 1998.
- [104] Hassig, H. J., “An approximate true damping solution of the flutter equation by determinant iteration.” *Journal of Aircraft*, Vol. 8, No. 11, 1971, pp. 885–889.
- [105] Chen, P., “Damping perturbation method for flutter solution: the g-method,” *AIAA journal*, Vol. 38, No. 9, 2000, pp. 1519–1524.
- [106] Guertin, M., *The Application of Finite Element Methods to Aeroelastic Lifting Surface Flutter*, Ph.D. thesis, Rice University, 2012.

- [107] Platzer, M. F., Jones, K. D., Young, J., and S. Lai, J., “Flapping wing aerodynamics: progress and challenges,” *AIAA journal*, Vol. 46, No. 9, 2008, pp. 2136–2149.
- [108] Young, J. and S. Lai, J. C., “Oscillation frequency and amplitude effects on the wake of a plunging airfoil,” *AIAA journal*, Vol. 42, No. 10, 2004, pp. 2042–2052.
- [109] Wright, J. R. and Cooper, J. E., *Introduction to aircraft aeroelasticity and loads*, Vol. 20, John Wiley & Sons, 2008.
- [110] Oakley, J. E. and O’Hagan, A., “Probabilistic sensitivity analysis of complex models: a Bayesian approach,” *Journal of the Royal Statistical Society: Series B (Statistical Methodology)*, Vol. 66, No. 3, 2004, pp. 751–769.
- [111] Saltelli, A., Chan, K., Scott, E. M., et al., *Sensitivity analysis*, Vol. 1, Wiley New York, 2000.
- [112] Hamby, D., “A review of techniques for parameter sensitivity analysis of environmental models,” *Environmental monitoring and assessment*, Vol. 32, No. 2, 1994, pp. 135–154.
- [113] Homma, T. and Saltelli, A., “Importance measures in global sensitivity analysis of nonlinear models,” *Reliability Engineering & System Safety*, Vol. 52, No. 1, 1996, pp. 1–17.
- [114] Iman, R. L., Helton, J. C., Campbell, J. E., et al., “An approach to sensitivity analysis of computer models, Part 1. Introduction, input variable selection and preliminary variable assessment,” *Journal of quality technology*, Vol. 13, No. 3, 1981, pp. 174–183.
- [115] Theis, J., Pfifer, H., and Seiler, P., “Robust Control Design for Active Flutter Suppression,” .
- [116] Glover, K., “All optimal Hankel-norm approximations of linear multivariable systems and their L₂-error bounds,” *International journal of control*, Vol. 39, No. 6, 1984, pp. 1115–1193.
- [117] Enns, D. F., “Model reduction with balanced realizations: An error bound and a frequency weighted generalization,” *Decision and Control, 1984. The 23rd IEEE Conference on*, Vol. 23, IEEE, 1984, pp. 127–132.

- [118] Petterson, K., “CFD analysis of the low-speed aerodynamic characteristics of a UCAV,” *AIAA Paper*, Vol. 1259, 2006, pp. 2006.
- [119] Watkins, C. E., Woolston, D. S., and Cunningham, H. J., “A systematic kernel function procedure for determining aerodynamic forces on oscillating or steady finite wings at subsonic speeds,” 1959.

Appendix A

Appendices

A.1 Equations for Doublet Lattice Method

This appendix section provides the equations associated with Doublet Lattice Method (DLM) which has been discussed in detail in Chapter 3. The DLM is the method used for modeling the unsteady aerodynamic forces on the BFF vehicle. the DLM has been implemented in Matlab to solve for any general lifting surface. Equations and methods used to compute integrals which are critical to this implementation are provided below.

This section provides the equations used to compute the kernel function K described in Eq. (3.3) between two points on a given lifting surface. The method and approximations used in integration of the kernel function to compute the entries of downwash matrix (see Eqs. (3.4)) are also provided here. These equations are from the Ref. [55].

The kernel function between points $p_1 := (x_1, y_1, z_1)$ and $p_2 := (x_2, y_2, z_2)$ for a given

Mach number M , reference chord \bar{c} and reduced frequency k is given as

$$x_0 = x_2 - x_1 \quad (\text{A.1a})$$

$$r_0 = \sqrt{(y_2 - y_1)^2 + (z_2 - z_1)^2} \quad (\text{A.1b})$$

$$\beta^2 = 1 - M^2 \quad (\text{A.1c})$$

$$R = \sqrt{x_0^2 + \beta^2 r_0^2} \quad (\text{A.1d})$$

$$k_0 = \frac{2kr_0}{\bar{c}} \quad (\text{A.1e})$$

$$u_0 = \frac{MR - x_0}{\beta^2 r_0^2} \quad (\text{A.1f})$$

$$I = \int_{u_0}^{\infty} \frac{e^{-jk_0 u}}{(1 + u^2)^{3/2}} du \quad (\text{A.1g})$$

$$K = \left(I + \frac{Mr_0 e^{-jk_0 u_0}}{R(1 + u_0^2)^{1/2}} \right) e^{-2jkx_0/\bar{c}} \quad (\text{A.1h})$$

The integral shown in Eq. (A.1 g) can be evaluated in two steps - integration by parts, followed by a polynomial approximation [55]. Integrating Eq. (A.4 g) by parts gives

$$I = \left[1 - \frac{u_0}{(1 + u_0^2)^{1/2}} \right] e^{-jk_0 u_0} - jk_0 \int_{u_0}^{\infty} \left[1 - \frac{u}{(1 + u^2)^{1/2}} \right] e^{-jk_0 u} du \quad (\text{A.2})$$

We can now use the approximation provided by Watkins et al [119] -

$$\frac{u}{(1 + u^2)^{1/2}} = 1 - 0.101e^{-0.329u} - 0.899e^{-1.4067u} - 0.09480933e^{-2.90u} \sin(\pi u) \quad (\text{A.3})$$

The polynomial approximation shown in Eq. (A.3) can be used to simplify and compute the integral in Eq. (A.2) analytically.

Eqs. (3.4) require the kernel function to be integrated across each doublet line on the grid. To simplify the integral, an equivalent rational function is constructed. The kernel function between the collocation point r and starting point (s_1), mid-point (s_2) and end point (s_3) of each doublet line is computed, and denoted as K_1 , K_2 and K_3 respectively. The variation of the kernel function across the doublet line is then modeled as a quadratic function of distance from the mid-point of the line. The

coefficients of the quadratic function, denoted A , B and C may be computed as

$$r_i = \sqrt{(y_r - y_{s_i})^2 + (z_r - z_{s_i})^2} \quad (i = 1, 2, 3) \quad (\text{A.4a})$$

$$\kappa_i = K_i r_i^2 \quad (\text{A.4b})$$

$$A = \frac{2(\kappa_1 - 2\kappa_2 + \kappa_3)}{L^2} \quad (\text{A.4c})$$

$$B = \frac{\kappa_3 - \kappa_1}{L} \quad (\text{A.4d})$$

$$C = \kappa_2 \quad (\text{A.4e})$$

The kernel function can now be written as a rational function as

$$K(\eta) = \frac{A\eta^2 + B\eta + C}{(\eta_0 - \eta)^2 + \zeta_0^2} \quad (\text{A.5a})$$

$$\eta_0 = (y_r - y_{s_2}) \cos \gamma + (z_r - z_{s_2}) \sin \gamma \quad (\text{A.5b})$$

where η is the local coordinate along the length of a given doublet line, originated at its mid-point and γ is the dihedral angle of the panel. In terms of the rational function described above, the downwash matrix entry shown in Eq. (3.3) may be written as

$$D_{ij} = \frac{1}{8} \pi c_j \int_{-\frac{L}{2}}^{\frac{L}{2}} \frac{A\eta^2 + B\eta + C}{(\eta_0 - \eta)^2 + \zeta_0^2} d\eta \quad (\text{A.6})$$

Analytical solution for the integral in Eq. (A.6) is available and is provided here -

$$I_{ij} = (\eta_0^2 A + \eta_0 B + C) \left(\frac{1}{\eta_0 - \frac{L}{2}} - \frac{1}{\eta_0 + \frac{L}{2}} \right) + \left(B + 2\eta_0 A \right) \log \left(\frac{\eta_0 - \frac{L}{2}}{\eta_0 + \frac{L}{2}} \right) + LA \quad (\text{A.7})$$

Therefore, using Eqs. (A.1), (A.4), (A.5) and (A.7), the integral in Eq. (3.3) can be computed in order to construct the required downwash matrix.

A.2 Derivation for Nelson's Method

This section provides the derivation for Nelson's method, which is used to compute derivatives of eigenvectors or mode shapes of a structural model with respect to a given set of system parameters. The main result of the derivation is a linear equation for computing the required eigenvector derivative.

Let a linear structural model be defined via a finite element model with matrices M and K denoting the mass and stiffness matrix. Eigenvectors are computed by solving the eigenvalue problem -

$$[K - \lambda_i M] \phi_i = 0 \quad (\text{A.8})$$

where λ_i and ϕ_i are the i^{th} eigenvalue and eigenvector respectively. Let $\theta := \{\theta_1, \theta_2 \dots \theta_n\}$ be a set of model parameters with respect to which eigenvector derivatives are required. To compute the derivative $\frac{\partial \phi_i}{\partial \theta_k}$, Eq. (A.8) is differentiated with respect to θ_k to obtain

$$[K - \lambda_i M] \frac{\partial \phi_i}{\partial \theta_k} + \left[\frac{\partial K}{\partial \theta_k} - \lambda_i \frac{\partial M}{\partial \theta_k} \right] \phi_i - \frac{\partial \lambda_i}{\partial \theta_k} M \phi_i = 0 \quad (\text{A.9})$$

For the purposes of this derivation, the finite element matrices are assumed to be scaled so that $\phi^T M \phi = I$ where I is identity matrix of the appropriate size. Also, it is assumed that the derivatives of mass and stiffness matrices with respect to the parameters are available. Pre-multiplying Eq. (A.9) by ϕ_i^T , and applying the fact that $\phi_i^T M \phi_i = 1$, we have

$$\frac{\partial \lambda_i}{\partial \theta_k} = \phi_i^T [K - \lambda_i M] \frac{\partial \phi_i}{\partial \theta_k} + \phi_i^T \left[\frac{\partial K}{\partial \theta_k} - \lambda_i \frac{\partial M}{\partial \theta_k} \right] \phi_i \quad (\text{A.10})$$

Thus, Eq. (A.10) represents the eigenvalue derivative for the i^{th} eigenvalue with respect to θ_k . We can simplify Eq. (A.10) by using Eq. (A.8) to show that the first term on the right hand side is zero -

$$\phi_i^T [K - \lambda_i M] = \left[[K - \lambda_i M] \phi_i \right]^T = 0 \quad (\text{A.11})$$

Therefore, the eigenvalue derivative can be written as

$$\frac{\partial \lambda_i}{\partial \theta_k} = \phi_i^T \left[\frac{\partial K}{\partial \theta_k} - \lambda_i \frac{\partial M}{\partial \theta_k} \right] \phi_i \quad (\text{A.12})$$

It should be kept in mind that the eigenvalue derivative computed in Eq. (A.12) is a scalar quantity. Now, every term in Eq. (A.9) can be computed since the eigenvalue derivative $\frac{\partial \lambda_i}{\partial \theta_k}$ is available from Eq. (A.12), the mass and stiffness matrices and their derivatives are analytically obtainable and the eigenvector ϕ_i is available as well. However, the equation cannot be solved for the eigenvector derivative $\frac{\partial \phi_i}{\partial \theta_k}$ appearing in it. This is because the coefficient of the eigenvector derivative $[[K - \lambda_i M]]$ is zero

as seen in Eq. (A.8).

To resolve this problem, the eigenvector derivative is expressed as a linear combination of all the mode shapes of the model. This is a valid assumption, since the complete set of eigenvectors ϕ are a valid, linearly independent basis. Therefore, for mode shape derivative $\frac{\partial \phi_i}{\partial \theta_k}$ we have

$$\frac{\partial \phi_i}{\partial \theta_k} = \sum_{s=1}^{s=n} \beta_{is} \phi_s \quad (\text{A.13})$$

Substituting Eq. (A.13) into Eq. (A.9) we get

$$[K - \lambda_i M] \sum_{s=1}^{s=n} \beta_{is} \phi_s + \left[\frac{\partial K}{\partial \theta_k} - \lambda_i \frac{\partial M}{\partial \theta_k} \right] \phi_i - \frac{\partial \lambda_i}{\partial \theta_k} M \phi_i = 0 \quad (\text{A.14})$$

We can obtain the required eigenvector derivative by computing the values of β shown in Eq. (A.13). To compute β_{ir} where $r \neq i$, we pre-multiply Eq. (A.13) by r^{th} mode shape ϕ_r^T to obtain

$$\phi_r^T [K - \lambda_i M] \sum_{s=1}^{s=n} \beta_{is} \phi_s + \phi_r^T \left[\frac{\partial K}{\partial \theta_k} - \lambda_i \frac{\partial M}{\partial \theta_k} \right] \phi_i - \frac{\partial \lambda_i}{\partial \theta_k} \phi_r^T M \phi_i = 0 \quad (\text{A.15})$$

In Eq. (A.15), the last term on the right hand side can be seen to be zero due to orthogonality property of the mode shapes. Using the same property, the first term on the right hand side may be simplified as follows -

$$\begin{aligned} \phi_r^T [K - \lambda_i M] \sum_{s=1}^{s=n} \beta_{is} \phi_s &= \beta_{ir} \phi_r^T [K - \lambda_i M] \phi_r \\ &= \beta_{ir} \left(\underbrace{\phi_r^T [K - \lambda_r M] \phi_r}_{=0} + [\lambda_r - \lambda_i] \underbrace{\phi_r^T M \phi_r}_{=1} \right) \\ &= \beta_{ir} [\lambda_r - \lambda_i] \end{aligned} \quad (\text{A.16})$$

Therefore, for all $r \neq i$, β_{ir} may be computed as

$$\beta_{ir} = \frac{1}{\lambda_i - \lambda_r} \phi_r^T \left[\frac{\partial K}{\partial \theta_k} - \lambda_i \frac{\partial M}{\partial \theta_k} \right] \phi_i \quad (\text{A.17})$$

For the case where $r = i$, β_{rr} can be computed from the property $\phi_r^T M \phi_r = 1$, by

differentiating both sides with respect to θ_k to obtain

$$\phi_r^T \frac{\partial M}{\partial \theta_k} \phi_r + 2\phi_r^T M \frac{\partial \phi_i}{\partial \theta_k} = 0 \quad (\text{A.18a})$$

$$2\phi_r^T M \sum_{s=1}^{s=n} \beta_{is} \phi_s = -\phi_r^T \frac{\partial M}{\partial \theta_k} \phi_r \quad (\text{A.18b})$$

$$\beta_{rr} = -\frac{1}{2} \phi_r^T \frac{\partial M}{\partial \theta_k} \phi_r \quad (\text{A.18c})$$

Using Eqs. (A.17) and (A.18), the required eigenvector derivative can be computed via Eq. (A.13).

A.3 BFF Vehicle State Space Matrices

This section provides the state space matrices for the reduced order BFF model used for control synthesis. The following points should be noted -

1. The parasitic dynamics associated with sensors and actuators has not been included i.e. this is a bare airframe model.
2. The final model is in modal canonical form, in which the A matrix is a block diagonal matrix comprising of modal damping and frequencies.
3. The B and D matrices provide columns corresponding to the left mid-board flap (elevator) and left outboard flap. The outboard flaps are used for control inputs.
4. Although the outputs are blended in the control design, the C matrix here provides outputs to all 6 accelerometers, IMU pitch rate and the performance output $\dot{\eta}_1$.
5. Inputs: $\{L_3, L_4\}$, Outputs: $\{\dot{\eta}_1, q, \text{Left wing tip fwd accel, Left wing tip aft accel, Right wing tip fwd accel, Right wing tip aft accel, Center Body fwd accel, Center body aft accel}\}$

A Matrix:

$$\begin{bmatrix} 0.28 & 27.35 & 0 & 0 & 0 & 0 & 0 & 0 & 0 & 0 & 0 & 0 \\ -27.35 & 0.28 & 0 & 0 & 0 & 0 & 0 & 0 & 0 & 0 & 0 & 0 \\ 0 & 0 & -69.27 & 2772.63 & 0 & 0 & 0 & 0 & 0 & 0 & 0 & 0 \\ 0 & 0 & -2772.66 & -69.27 & 0 & 0 & 0 & 0 & 0 & 0 & 0 & 0 \\ 0 & 0 & 0 & 0 & -68.84 & 2781.27 & 0 & 0 & 0 & 0 & 0 & 0 \\ 0 & 0 & 0 & 0 & -2781.27 & -68.84 & 0 & 0 & 0 & 0 & 0 & 0 \\ 0 & 0 & 0 & 0 & 0 & 0 & -249.65 & 1794.03 & 0 & 0 & 0 & 0 \\ 0 & 0 & 0 & 0 & 0 & 0 & -1794.03 & -249.65 & 0 & 0 & 0 & 0 \\ 0 & 0 & 0 & 0 & 0 & 0 & 0 & 0 & -222.08 & 1730.96 & 0 & 0 \\ 0 & 0 & 0 & 0 & 0 & 0 & 0 & 0 & -1730.96 & -222.08 & 0 & 0 \\ 0 & 0 & 0 & 0 & 0 & 0 & 0 & 0 & 0 & 0 & -8.10 & 85.68 \\ 0 & 0 & 0 & 0 & 0 & 0 & 0 & 0 & 0 & 0 & -85.68 & -8.10 \end{bmatrix}$$

B Matrix:

$$\begin{bmatrix} 47.14 & 40.54 \\ 36.89 & 63.54 \\ -659.77 & -57.12 \\ 77.34 & -87.28 \\ 328.16 & 21.32 \\ 243.42 & -11.64 \\ 204.37 & -577.67 \\ 83.34 & -446.17 \\ 228.53 & -577.75 \\ 128.81 & -401.22 \\ -22.98 & 18.65 \\ 41.98 & -65.54 \end{bmatrix}$$

C Matrix:

$$\begin{bmatrix} -0.58 & 0.611 & 0.62 & 0.32 & -0.24 & 0.45 & 0.88 & 0.89 & -0.0052 & -0.0080 & 0.0005 & -0.0045 \\ -0.17 & 0.08 & -0.303 & -0.11 & 0.095 & -0.2171 & -0.3715 & -0.37 & 0.0033 & 0.0027 & -0.0012 & 0.0032 \\ -10.89 & -15.83 & 55.53 & 122.34 & -33.43 & 69.52 & 135.03 & 142.89 & 123.03 & 150.98 & 22.73 & -8.17 \\ -10.89 & -15.83 & 55.53 & 122.34 & -33.43 & 69.52 & 135.03 & 142.89 & 123.03 & 150.98 & 22.73 & -8.17 \\ -10.79 & -15.77 & 53.57 & 65.13 & -115.12 & -2.046 & 125.84 & 147.50 & -123.45 & -154.13 & -22.33 & 8.04 \\ -10.79 & -15.77 & 53.57 & 65.134 & -115.12 & -2.04 & 125.84 & 147.50 & -123.45 & -154.13 & -22.33 & 8.04 \\ -3.69 & -9.12 & 31.12 & 33.48 & -25.98 & 22.33 & 51.13 & 65.34 & -0.2167 & 0.19 & 0.0481 & -0.0224 \\ 2.39 & -3.41 & 11.15 & -17.92 & 15.20 & 12.60 & -16.52 & -2.78 & -0.22 & 1.71 & -0.082 & 0.0145 \end{bmatrix}$$

D Matrix

$$\begin{bmatrix} 2.06 & 1.84 \\ -0.54 & -0.57 \\ 88.30 & 115.43 \\ 88.30 & 115.43 \\ 155.66 & -111.04 \\ 155.66 & -111.04 \\ 116.41 & 125.68 \\ 111.65 & 231.03 \end{bmatrix}$$